

ornl

**ORNL/TM-8203
ENDF-333**

**OAK
RIDGE
NATIONAL
LABORATORY**



**Application of New Techniques
to ORELA Neutron Transmission
Measurements and Their Uncertainty
Analysis: The Case of Natural Nickel
from 2 keV to 20 MeV**

D. C. Larson
N. M. Larson
J. A. Harvey
N. W. Hill
C. H. Johnson

**OPERATED BY
UNION CARBIDE CORPORATION
FOR THE UNITED STATES
DEPARTMENT OF ENERGY**

Printed in the United States of America. Available from
National Technical Information Service
U.S. Department of Commerce
5285 Port Royal Road, Springfield, Virginia 22161
NTIS price codes—Printed Copy: A07 Microfiche A01

This report was prepared as an account of work sponsored by an agency of the United States Government. Neither the United States Government nor any agency thereof, nor any of their employees, makes any warranty, express or implied, or assumes any legal liability or responsibility for the accuracy, completeness, or usefulness of any information, apparatus, product, or process disclosed, or represents that its use would not infringe privately owned rights. Reference herein to any specific commercial product, process, or service by trade name, trademark, manufacturer, or otherwise, does not necessarily constitute or imply its endorsement, recommendation, or favoring by the United States Government or any agency thereof. The views and opinions of authors expressed herein do not necessarily state or reflect those of the United States Government or any agency thereof.

ORNL/TM-8203
ENDF-333
Dist. Category UC-79d

Engineering Physics Division

**APPLICATION OF NEW TECHNIQUES TO ORELA NEUTRON TRANSMISSION
MEASUREMENTS AND THEIR UNCERTAINTY ANALYSIS: THE CASE OF
NATURAL NICKEL FROM 2 keV TO 20 MeV**

D. C. Larson, N. M. Larson,* J. A. Harvey, N. W. Hill,** and C. H. Johnson***

*Computer Sciences Division
**Instrumentation and Controls Division
***Physics Division

Manuscript completed: September 1983
Date Published: October 1983

NOTICE This document contains information of a preliminary nature.
It is subject to revision or correction and therefore does not represent a
final report.

Prepared by
OAK RIDGE NATIONAL LABORATORY
Oak Ridge, Tennessee 37830
operated by
UNION CARBIDE CORPORATION
Under Contract No. W-7405-eng-26
for the
Division of Basic Energy Sciences
and the
Division of Reactor Research and Technology
U.S. DEPARTMENT OF ENERGY

CONTENTS

ABSTRACT	1
1. INTRODUCTION	1
2. EXPERIMENTAL PROCEDURE	2
3. BACKGROUND DETERMINATION	6
3.1 Use of Discriminators to Isolate Backgrounds	6
3.2 Detector Afterpulsing Studies	9
3.3 Hydrogen Total Cross-Section Tests	12
4. DATA REDUCTION	13
4.1 Deadtime Corrections	13
4.2 Background Removal	18
4.2.1 Time-Independent Background	20
4.2.2 Background Due to 2.2-MeV Gamma Rays	20
4.2.3 Background Due to the $^{10}\text{B}(n,\alpha\gamma)$ Reaction	21
4.2.4 Other Possible Sources of Backgrounds	24
4.3 Conversion of Corrected Data to Cross Sections and Energies	25
5. UNCERTAINTY ANALYSIS	26
5.1 Channel-Independent Uncertainties	27
5.1.1 Sample Thickness Uncertainties	27
5.1.2 Uncertainty Due to Monitor Counter	29
5.2 Channel-Dependent Uncertainties	32
5.2.1 Energy-Scale Uncertainties	32
5.2.2 Deadtime Uncertainties	35
5.2.3 Background Uncertainties	36
5.3 Cross-Section Uncertainties and Correlations	37
5.4 The Uncertainty Propagation Code ALEX	64
6. DISCUSSION OF RESULTS	65
6.1 Nickel Cross-Section Results	65
6.2 Covariance Analysis Results	80
6.2.1 Uncertainty Analysis Results Where Cross Sections Have Been Averaged Into a 15-Group Set and All Correlations in Input Parameters Are Included	80
6.2.2 Same Example as in Sect. 6.2.1, but With Diagonal Covariance Matrix for the Input Diameters	87
6.2.3 Example of Small Energy Intervals and Full Covariance Matrix for Input Parameters	87
6.2.4 Example of 15-Group Cross Sections with Full Parameter Matrix for Input Parameters, but Uncertainties on n , m , M , and σ^2 Decreased by 100	87
6.2.5 Same Example as Previous Case, Except a Diagonal Covariance Matrix Was Used for the Input Parameters	93
6.2.6 Uncertainty Analysis for the Averaged Data	93
6.2.7 Conclusions from Uncertainty Analysis Results	93

7. SUMMARY AND CONCLUSIONS	96
ACKNOWLEDGEMENTS	97
REFERENCES	97
APPENDIX A. EFFECTS OF NEUTRON INTENSITY VARIATION ON THE DEADTIME CORRECTION	100
APPENDIX B. METHOD OF ESTIMATING $(1 + \sigma^2)$	110
APPENDIX C. MONITOR UNCERTAINTIES DUE TO DEADTIME CORRECTIONS ...	114
APPENDIX D. AVERAGED CROSS SECTION RESULTS	117

APPLICATION OF NEW TECHNIQUES TO ORELA NEUTRON TRANSMISSION
MEASUREMENTS AND THEIR UNCERTAINTY ANALYSIS: THE CASE OF
NATURAL NICKEL FROM 2 keV TO 20 MeV

D. C. Larson, N. M. Larson, J. A. Harvey, N. W. Hill, and C. H. Johnson

ABSTRACT

The neutron transmission through a 2.54-cm sample of natural nickel has been measured for neutron energies between 2 keV and 20 MeV. The Oak Ridge Electron Linear Accelerator (ORELA) was used to provide the neutrons which were detected at the 200-m flight path by a NE110 proton recoil detector. A selective gating system was utilized to minimize background effects due to large light-level events which produce phototube afterpulsing and long decay-constant light emission in the detector. A detailed discussion of the development of this system is given.

Known background sources are described, and the methods used to correct for these backgrounds are presented. An in-depth uncertainty analysis is given for this measurement, with explicit formulas derived for each effect contributing to the cross-section uncertainty. Parameter uncertainties and correlations among the parameters describing the backgrounds, deadtime, and other sources of uncertainty are given. To obtain a covariance matrix for this measurement, the final cross-section results are binned into 15 energy groups, and a covariance matrix is provided for this 15-group set. We find that the largest contributions to the cross-section uncertainty are due to sample properties, beam monitors (used to normalize sample-in and sample-out counts), and ORELA power variations during the run which affect the deadtime correction. Overall uncertainties in the cross section for this measurement are on the order of 2%. The resulting cross sections are compared with the ENDF/B-V file for nickel; many resonances not presently in the file are observed, and energy-scale differences are noted.

1. INTRODUCTION

It has been realized for some time that the evaluated neutron total cross section for nickel is in disagreement with thick sample shielding benchmark measurements (WE82). Comparisons of calculated results (using ENDF/B-V) with the measured transmission through 15.2 cm and 30.5 cm of nickel imply that the evaluated cross section is as much as 20% too large in the energy region from 1.0 to 1.4 MeV and 10% too large up to 3 MeV. The "broomstick" series of shielding benchmarks (MA76) are particularly sensitive to cross-section minima since thick samples are used. These discrepancies are assumed to result mainly from a lack of high-resolution data needed to better define the cross-section minima associated with s-wave resonances.

In addition to this benchmark discrepancy, the data from which the resolved resonance parameters, Γ_n , were obtained have relatively poor energy resolution by today's standards. A new high-resolution measurement should provide a better set of resonance parameters and allow the resolved resonance region to be extended in energy from its present upper limit of 650 keV. The present high-resolution measurement of the neutron transmission through a sample of natural nickel is an attempt to resolve the benchmark discrepancy, as well as provide a uniform set of data from ~ 2 keV to 20 MeV for use in the next ENDF/B update.

The purpose of this report is (a) to document in detail the newly developed experimental procedure and data reduction techniques, (b) to provide for the first time a detailed variance-covariance analysis of our transmission measurements, and (c) to provide a graphical comparison with the present ENDF/B-V evaluation.

In Section 2 we describe the experimental procedure used for this measurement. Section 3 presents a discussion of the backgrounds present in this work, and our techniques for evaluating them. We also describe a source of background to which we have not been sensitive in the past — phototube afterpulsing phenomena. Finally, we describe the hydrogen total cross-section measurements which were done to check our data-acquisition scheme. In Section 4 we describe our data-reduction techniques, including deadtime corrections, background removal, and conversion to cross sections. Section 5 is a detailed description of the uncertainty analysis for this measurement, including derivation of equations for all known non-zero entries in the covariance matrix for this measurement. In Section 6 we present our nickel total cross-section results compared with the ENDF/B-V evaluation, as well as results of the variance-covariance uncertainty analysis. Finally, in Section 7 a summary of the work is presented, and conclusions are drawn.

Appendices A and B contain derivations of the deadtime and neutron intensity variation corrections used in this work, Appendix C describes deadtime corrections required in determining the uncertainty associated with the neutron monitor which is used to normalize the sample-in and sample-out spectra, and Appendix D is a microfiche listing of our averaged cross-section data and associated uncertainties.

2. EXPERIMENTAL PROCEDURE

The 200-m flight path of the Oak Ridge Electron Linear Accelerator (ORELA) was used for the measurement. The accelerator was run using a repetition rate of 780 Hz at an electron burst width of 7.5 ± 0.5 ns with 8 kW of power on the target. The beryllium-clad, water-cooled tantalum target was used for the neutron production. A 7.9-cm-thick rectangular (5.4 by 4.8 cm) shadow bar, consisting of 2.9 cm uranium, 2.5 cm thorium, and 2.5 cm tantalum, was located in the beam at 4 m. A 7.6-cm-diam brass collimator was used at 9 m so the detector was illuminated by neutrons both from the tantalum and from the surrounding cooling-water moderator. The 1820-g natural-nickel sample was cylindrical in shape with a diameter of 10.2 cm and a length of 2.54 cm, giving a sample thickness of 0.2304 atoms/b. It was cut from 10.2-cm-diam round hot forged bar stock, ASTM Grade 160 (A grade). The specifications for this grade of nickel are a minimum nickel content of 99.97% (by weight), a cobalt content of less than 0.001%, and less than 0.02% C, 0.005% Fe, and less than 0.001% total additional impurities. A chemical analysis for impurities was done as a check and the results, while less sensitive than the impurity specifications, showed that any impurities present were less than 0.1% by weight. Filters used in the beam included 3.8 cm of uranium to diminish the effect in the detector of the gamma flash produced when the electron beam strikes the target and a 300-mg/cm² ¹⁰B filter to eliminate overlap of low-energy neutrons from preceding bursts. Data acquisition was under computer control with the sample being alternated in and out of the beam by the computer approximately every 10 minutes for a total of 106 hours of beam time. Averaged over the measurement, about 1.4 counts/burst were accepted for the sample-in cycle and 1.9 counts/burst for the sample-out cycle. A neutron monitor, located in the concrete wall surrounding the target, was used to normalize the sample-in and sample-out data to the same neutron source intensity.

Neutron energies are determined by the time-of-flight technique. The start signal for the time-digitizer system is taken from a bare phototube placed in the linac target vault to view the gamma flash

resulting from the electron burst. Stop pulses for the digitizer are neutron events in the remote detector. The gamma flash is also observed at the remote detector and provides a fiducial time for determining neutron energies.

The width of the time-of-flight channels is adjusted with the data-acquisition program so there are at least three channels per resolution width over the neutron energy range of interest in the experiment. This scheme minimizes the number of channels used for an experiment by crunching neutron energy regions, where the cross section is approximately energy independent, into a few wide channels. The measurements reported in this paper were performed using 60,000 channels varying in width from 1 ns to 1 μ sec, the wider bins being used at long flight times to determine the time-independent background. Table 1 presents the time-of-flight channel structure used for the nickel measurements.

Table 1. Time-of-flight channel structure

Number of Channels	Channel width (nsec)	Time-of-flight range (μ sec)	Energy Range (keV)
34,836	1	0 - 34	3×10^5 - 183
7,000	2	34 - 48	183 - 92
8,000	4	48 - 80	92 - 33
5,000	16	80 - 160	33 - 8.3
2,000	200	160 - 560	8.3 - 0.68
3,164 (574) ^a	1000	560 - 3724 (1134)	0.68 - 0.16

^aThe numbers in parentheses correspond to the number of channels and time actually utilized before the system was disabled to wait for the next burst.

A block diagram of the important electronic components is shown in Fig. 1. We will only sketch its operation here. The reasons for this electronics arrangement will be presented in Sect. 3 where background determinations are discussed. The fast signal from the Zener base of the RCA-8854 phototube is fed into an active amplifier fanout and then into four constant-fraction discriminators. Each discriminator has a different lower bias level, with bias 1 having the lowest level and bias 4 the highest. Figure 2 is a diagram of the bias-level concept used in our measurements. These output signals are fed into an OR circuit, and the delayed output is used as the stop for the clock. Cable lengths are carefully chosen between the fanout and the OR gate so timing signals from each discriminator are consistent. If the pulse height is such that it is between bias levels 1 and 2, the signal is shaped, passes through one section of a strobe coincidence, sets tag 4 in the clock, and is stored in the "bias 1" spectrum in the data-acquisition computer. If the pulse height from the detected event falls between bias levels 2 and 3, tag 3 is set in the clock and the count is stored in the bias-2 spectrum. However, if this pulse height is identified in time as being an event from the gamma flash, the electronics on the right-hand side of the clock prevents any further counts from that burst to be stored. If the count is later than the gamma flash, further counts from that burst can be registered. If the pulse height falls between bias levels 3 and 4, the operation is the same as for the bias-2 spectrum case, except the count is stored in the bias-3 spectrum. If the pulse height is greater than the bias-4 level, the count is stored in the bias-4 spectrum, and the remainder of the electronics to the right of the clock prevents further counts being accepted from that burst regardless of when the primary bias-4 spectrum pulse occurs. The reason for the special treatment of gamma-flash events in biases 2 and 3 and all events in bias 4 is related to backgrounds caused by afterpulsing in the detector system initiated by large light-level events. This will be discussed in detail in Sect. 3.2.

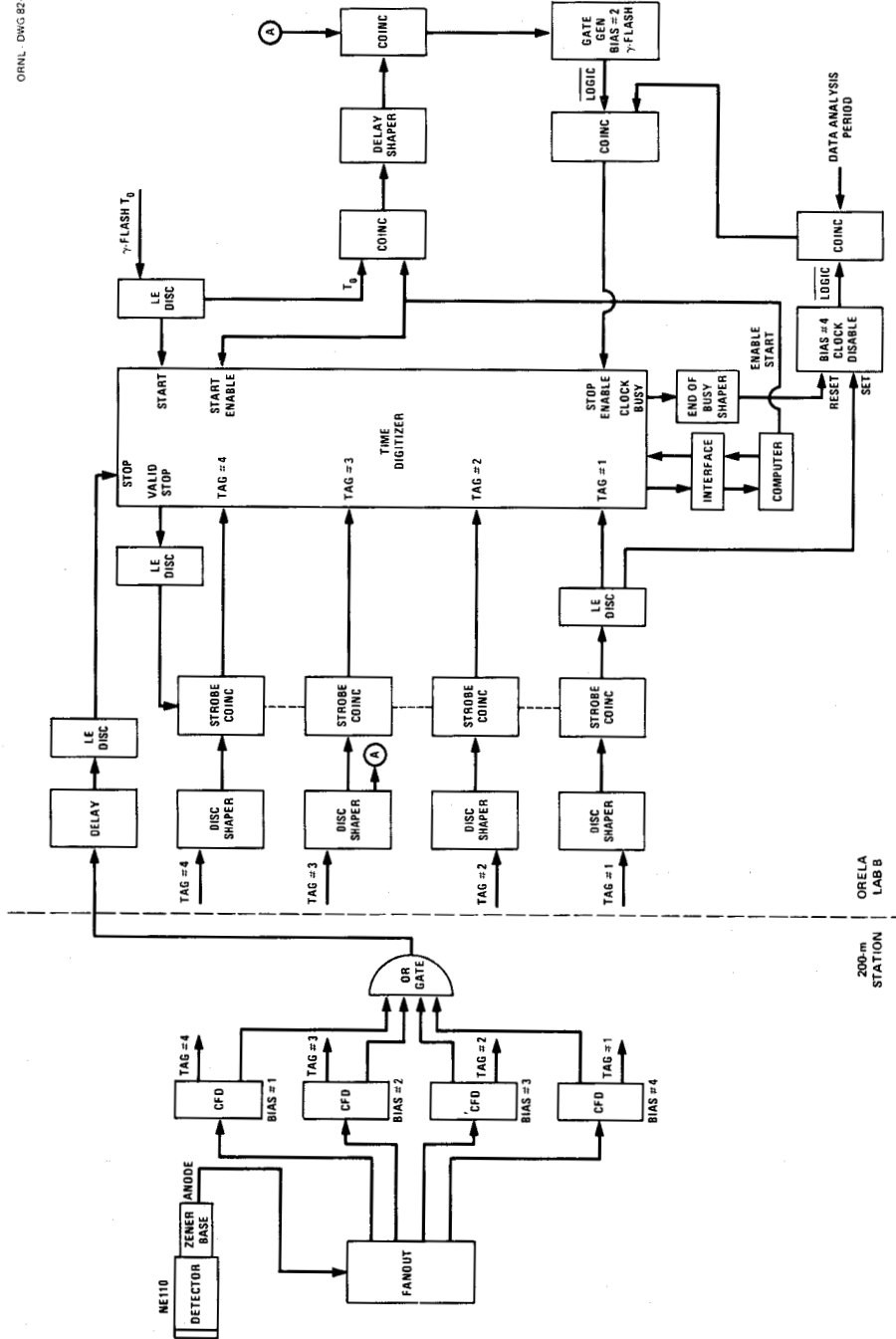


Fig. 1. Schematic outline of the electronics used in the present measurement. Components to the left of the dashed line are located at the 200-m station, and the resulting logic signals are transmitted for further analysis in the components to the right of the dashed line, located in Lab B at ORELA.

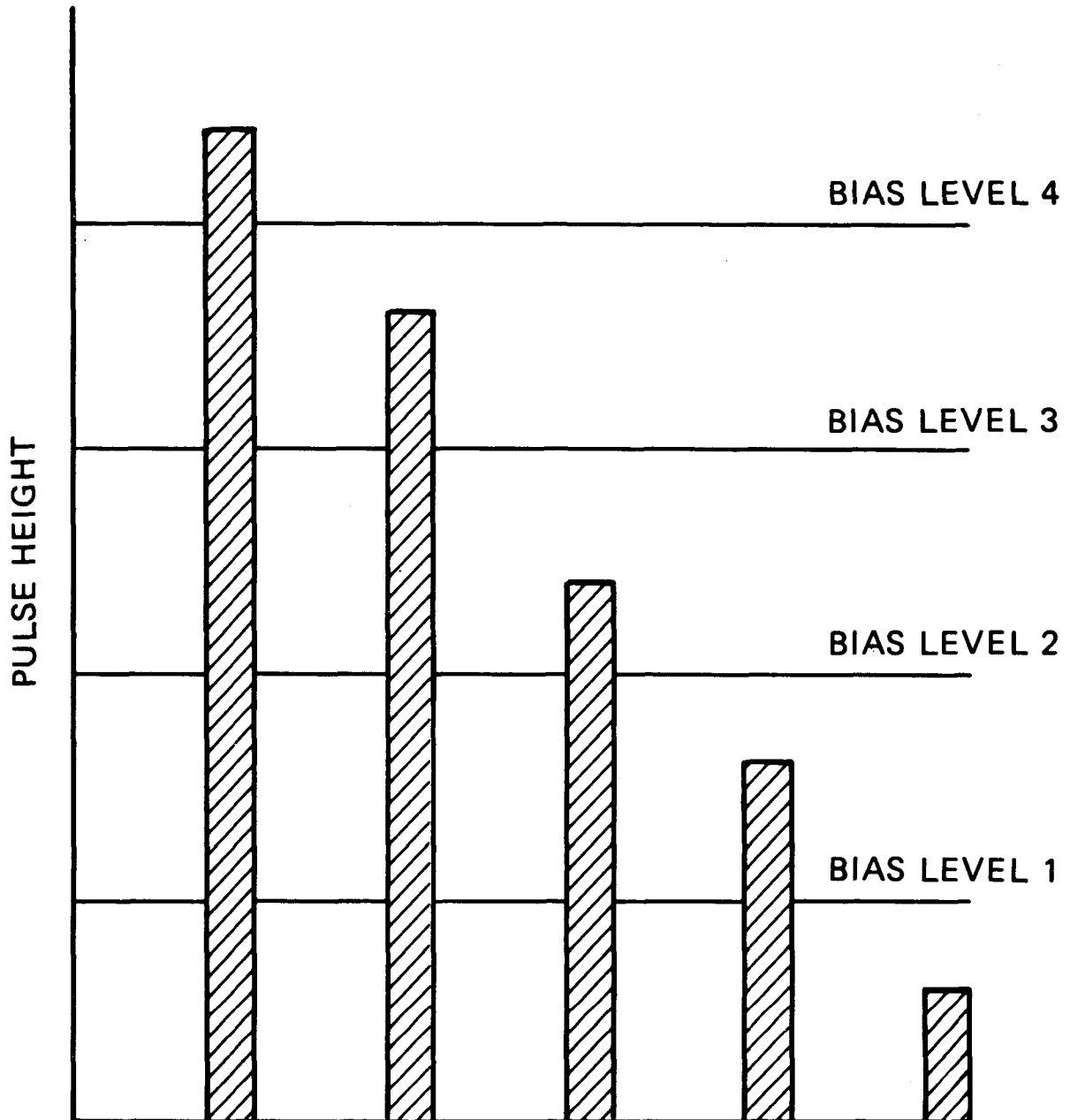


Fig. 2. Schematic diagram of the "bias level" concept used for crude pulse height analysis. If a signal is below the discriminator setting on the CFD for bias 1, it is rejected. This bias is adjusted to respond to light levels corresponding to 1 to 2 photoelectrons. If the signal is larger than the bias-1 discriminator, but below the bias-2 discriminator, it is registered as a count in the appropriate time-of-flight channel of the "bias-1" spectrum. Similarly, if the signal is larger than the bias-1 and bias-2 discriminator settings, but below the bias-3 level, the count is stored in the "bias-2" spectrum. A pulse height larger than bias levels 1, 2, and 3, but smaller than 4, is registered as a count in the "bias-3" spectrum. Finally, a pulse height larger than all four discriminator settings is registered in the "bias-4" spectrum. Thus high-energy neutrons (as evidenced by their t-o-f) can be stored in any of the bias spectra, but low energy neutrons can only be stored in the low bias spectra. If a pulse height is registered in bias i , but not the lower biases, it is tagged as a false event and stored elsewhere.

3. BACKGROUND DETERMINATION

Since the neutron flux from ORELA is a maximum in the region from a few keV to a few MeV, measurements frequently concentrate on this energy range. However, detectors to cover this energy range need to be improved. Lithium glass detectors rapidly lose efficiency above a few keV, and organic scintillators have been used mostly above 100 keV. Past measurements at ORELA have utilized both detector types. A number of improvements in extending the useful energy range of organic scintillators to lower neutron energies have been made in the last few years. Some of these results for NE110 scintillators will now be discussed.

Before approximately 1978, our measurements (LA76) generally used a discriminator to reject events which produced less than three or four photoelectrons per neutron event, corresponding to a few tens of keV neutron energy. However, since these detection processes are statistical, lower energy neutrons would occasionally produce enough photoelectrons to register an event. Therefore, we were able to measure cross sections for neutron energies down to 10-20 keV, although with poor statistics. Improved low-noise photomultiplier tubes and electronics have encouraged the effort to lower the discriminator bias to the lowest possible limit (between 1 and 2 photoelectrons per event), making it possible to detect recoiling protons from neutrons of only a few keV in energy. However, when this was tried, new sources of background appeared which were not observed in the older measurements. Much work has been done to isolate the sources of these backgrounds, remove them where possible, and develop a data-acquisition scheme which minimizes the residual backgrounds while, at the same time, preserving a reasonable counting rate. Prior to this nickel measurement (and succeeding measurements for molybdenum and titanium), a number of studies were made to determine the lower neutron-energy limit for which useful data could be reliably measured. These efforts will be documented in this report for completeness, although the development work is continuing.

3.1 USE OF DISCRIMINATORS TO ISOLATE BACKGROUNDS

For work described in this report, the detector consisted of a 1.9-cm-thick by 10.2-cm-diam piece of NE110 plastic scintillator, coupled to a RCA-8854 phototube. This phototube was selected for photocathode uniformity, quantum efficiency, and low afterpulsing. As in previous measurements (LA76), four separate contiguous t-o-f spectra are simultaneously measured for both sample-in and sample-out to help isolate background sources. Each spectrum is characterized by a different lower cutoff on the pulse height from the scintillator. These are referred to as "bias levels" in this work. Figure 3a illustrates spectra for each of the four bias levels as a function of channel number, and Fig. 3b relates the channel number to neutron energy and time-of-flight. In terms of proton recoil energy, bias 1 covers the energy range from just above the noise background to about 150 keV; bias 2 covers from 150 to 600 keV; bias 3 covers from 600 keV to 2 MeV; and bias 4 covers from 2 MeV up to ~ 30 MeV. The corresponding neutron energy regions are not well defined since the recoiling protons have a broad energy distribution and the pulse-height resolution of the NE110 plastic is rather poor. Absolute values for thresholds of the four bias levels could be related to energies of known gamma-ray sources, but we have found it easier operationally simply to describe the biases by the neutron energies at which the spectra cross over with equal intensity. For the present measurement, the cross-over for biases 1 and 2 occurs at 170 keV, for biases 2 and 3 at 560 keV, and for biases 3 and 4 at 1870 keV. Each bias group is further described by giving the minimum neutron energy which can produce a pulse from a proton recoil and thereby be registered in that bias. For bias 1, the neutron energy cutoff is ~ 0.8 keV; bias 2 has no counts for neutron energies less than 45 keV; the bias 3 cutoff is 300 keV; and the bias 4 cutoff is 1.2 MeV. Since a recoil proton energy distribution is approximately uniform up to an energy equal to the incident neutron energy, a high-energy neutron can be registered in any of the four biases, but a low-energy neutron can be registered only in biases corresponding to cutoffs noted above. To extend the

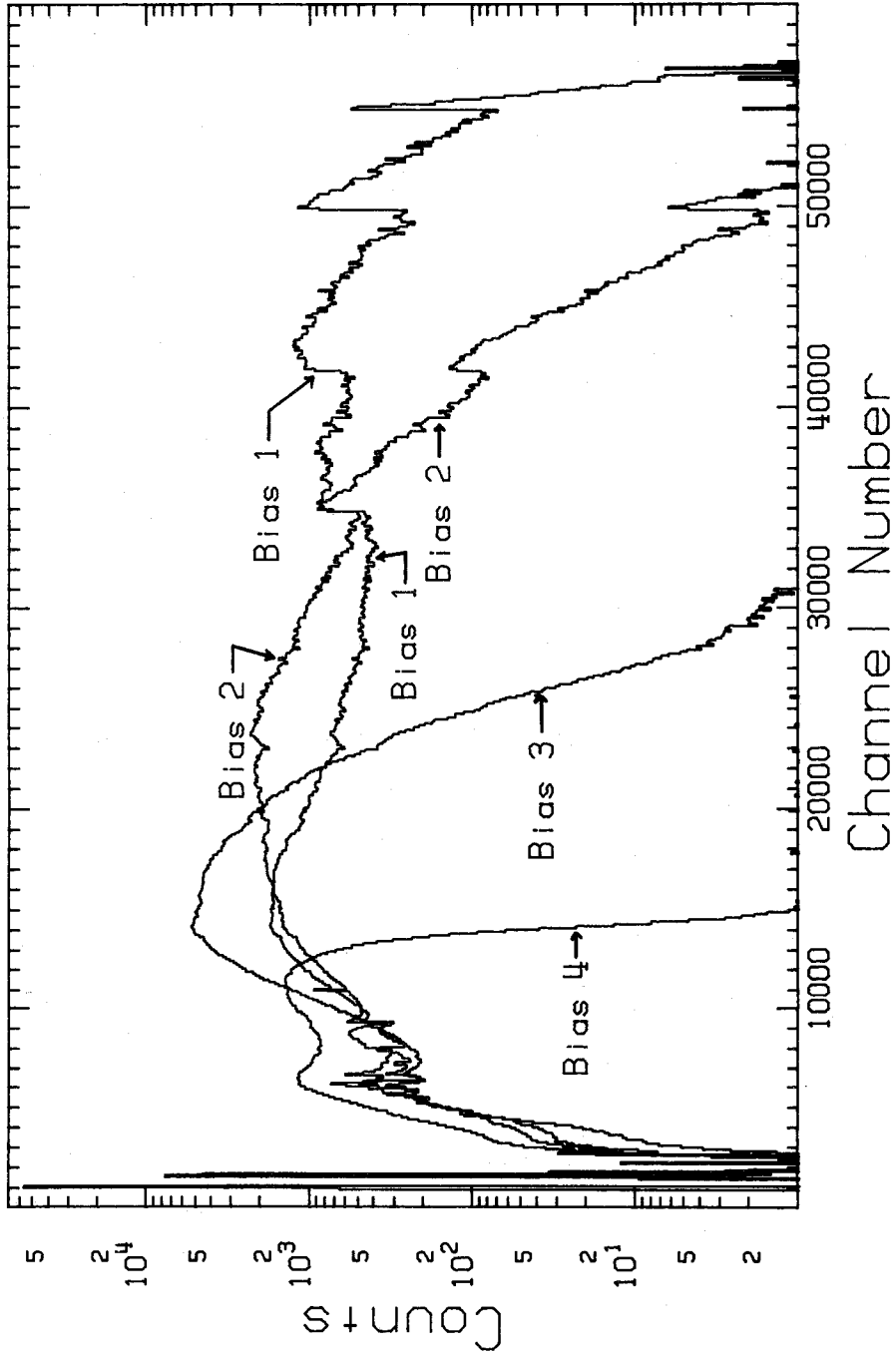


Fig. 3a. Illustration of the neutron spectra obtained in each of the four bias levels for the sample-out measurement on nickel as a function of the time-of-flight channel number. For clarity, the backgrounds have been removed, and the data have been averaged over 50 channels.

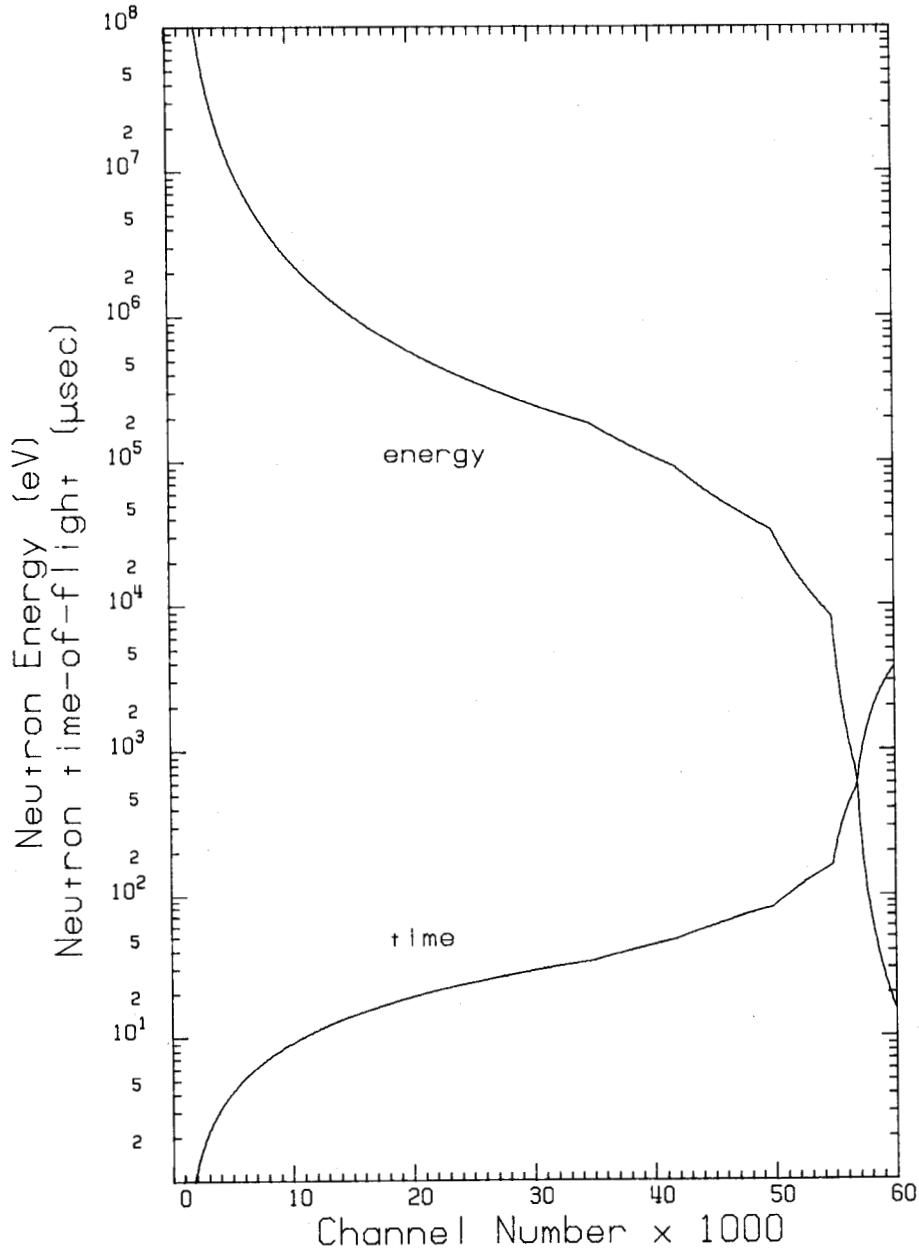


Fig. 3b. Plot of neutron energy and time-of-flight as a function of channel number.

energy range of the detected neutrons as low as possible, the bias-1 discriminator must be set in the vicinity of one photoelectron. Difficulties with extending organic scintillators to low energies are discussed in refs. HA79 and RE78. In studying this extension to low-neutron energies, it became apparent that there was some source of small pulses which caused data in the lowest two bias levels to be wrong. Investigation of this phenomenon demonstrated that it was due to afterpulsing in the detector system. A number of studies were made to understand this phenomenon and, for completeness, will be described here in some detail.

3.2 DETECTOR ATERPULSING STUDIES

To understand the time distribution of the afterpulses, a ^{60}Co source (1.17-MeV and 1.33-MeV gamma rays) was placed near the detector. One TDC-100 time digitizer (clock) was started by a pulse generator to simulate the linac pulse and was stopped by the output of a discriminator set to trigger only for the top 10% of the ^{60}Co pulse-height distribution. For this clock, the deadtime was set at 32 μsec under the assumption that afterpulsing effects had disappeared by 32 μsec following detection of the large light-level event. A valid stop from this first clock was used to start a second TDC-100 clock. This same valid stop, in conjunction with a variable delay and width, was also used to enable the analysis period for the second clock. The second clock used additional discriminators set at the typical levels of bias 1 and bias 2 as stops. The afterpulses per legitimate primary pulse were counted in this variable width time window which was opened only if there was a large light-level primary pulse. Data were taken step-by-step as the time window was moved from nearly zero to 100- μsec delay. The background of true coincident initial pulses was subtracted. The results of this measurement are shown in Fig. 4 where the afterpulses per initial pulse per μsec time window are plotted as a function of time after initial pulse. Results are shown for biases 1 and 2 since the measurement showed negligible effects in biases 3 and 4. The sharp peak at 1.1 μsec is generated by backstreaming ions which originate at or near dynode 1 and produce electrons upon impact with the photocathode. The peaks at 3.6 and 8 μsec are thought to be the same mass ion coming from further down the dynode structure, or heavier ions again originating at dynode 1. The time-dependent continuum probably results from asynchronous ion feedback and/or the typical long decay time constant of the scintillator.

This experiment clearly demonstrates that, for this scintillator and phototube, small pulses can be expected following a detected event which produces a large light level and these small pulses can give rise to a time-dependent background which is difficult to remove. For example, as will be shown later, simply gating the phototube will not eliminate the effects produced by data events from large light-level pulses.

To understand the effects in a total cross-section measurement, a series of experiments were done to measure the transmission of a filtered beam. Filters in the beam included 2.54 cm of uranium and 10.2 cm of polyethylene. The beam which passed through the filters included some of the gamma burst, neutrons above ~ 400 keV in energy, and the 2.2-MeV gamma rays which result from neutron capture in the water moderator surrounding the target (and decay with ~ 17.6 μsec half-life). Hydrogen was chosen for the transmission sample because the neutron and gamma-ray cross sections are grossly different. The sample was actually 7.6 cm of polyethylene with a carbon compensator and had a (hydrogen) thickness of $n = 0.61$ atoms/barn (see Eq. 5.1 for definition of n).

The first experiment was run in the "usual" mode used for previous transmission measurements at ORELA except the new (lower) bias settings were used. Multiple stops per start were allowed with the clock being dead for 1104 ns following an event to allow processing of that event. The gamma flash was gated off both at the phototube base and via a time delay. Data were obtained in each of the four bias levels, corrected for deadtime and time-independent backgrounds, converted to cross sections, and

ORNL-DWG 82-11247

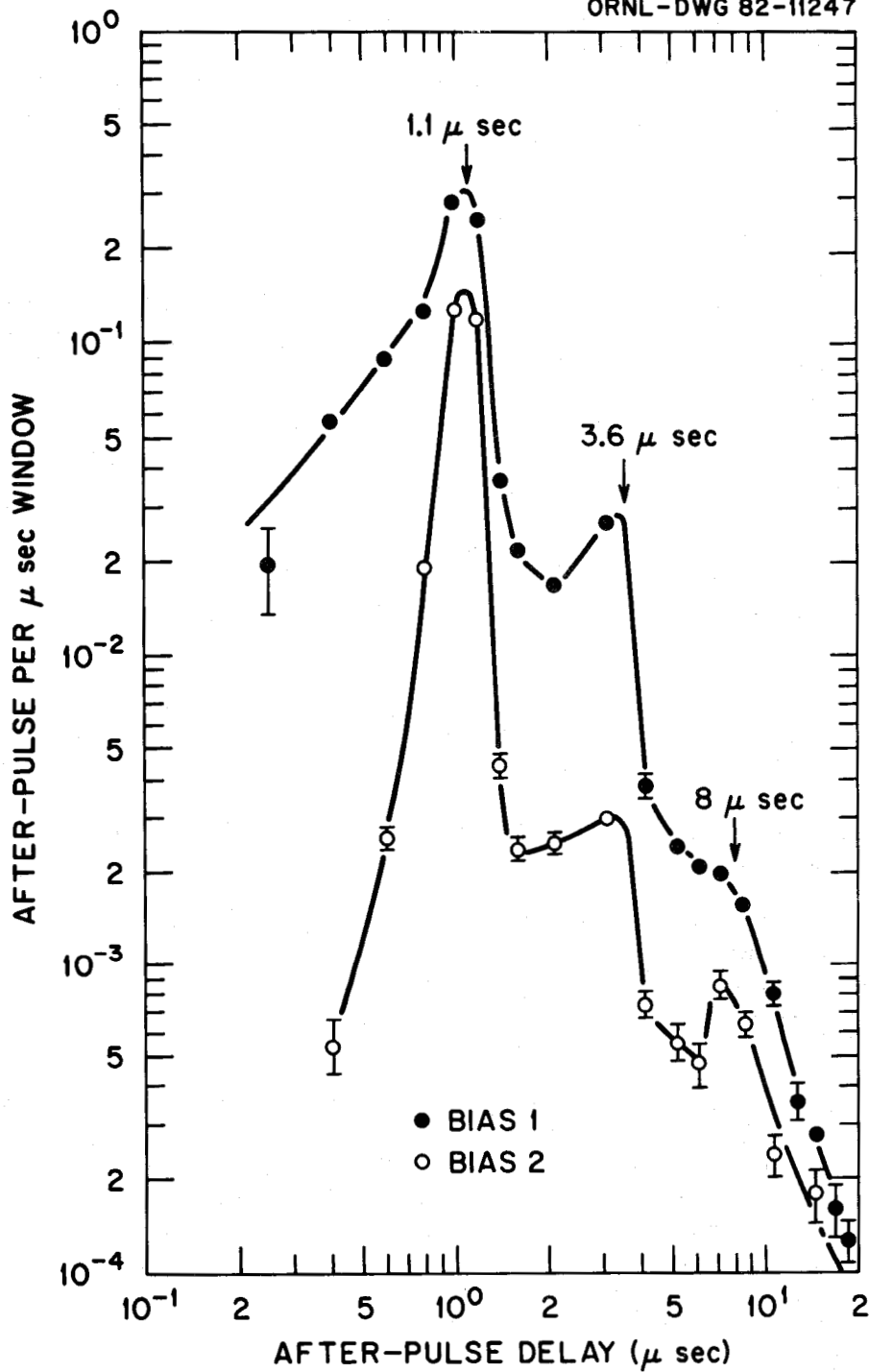


Fig. 4. Plot of the afterpulses per initial stop per μsec window as a function of the time following the initial stop. Corresponding data for bias 3 and bias 4 are very small and off the bottom of the scale. Results for biases 1 and 2 are also very small and off-scale for delay times $>20 \mu\text{sec}$.

compared with the hydrogen total cross section from ENDF/B-V (ST79). For biases 3 and 4 the data were in agreement with the evaluation (1 to 2%), but in biases 1 and 2 the resulting cross-section data were a factor of two low, indicating (as expected) that afterpulsing was causing a large background. These afterpulses were small enough to be below the discriminator levels for biases 3 and 4. Since the cross sections for biases 1 and 2 were low, we deduce the background due to afterpulsing must be proportionately more important for sample-in (CH_2) than sample-out (C). Also, this background must be due mainly to gamma rays, since the neutrons are more highly attenuated by the CH_2 than the C, but the gamma-ray transmission is about the same through both the C and CH_2 , due to the small gamma-ray cross section of hydrogen. To identify the magnitude of the afterpulsing background resulting from the 2.2-MeV gamma rays (often used in the past as a diagnostic tool), the data for each bias were crunched into 2- μsec bins and plotted. The characteristic 17.6- μsec slope was observed in each bias. In the past, with different detector systems and bias-level discriminator settings, the ratios of the background in the biases 1 through 4, relative to 4, were $\approx 0.2:0.2:0.2:1.0$. However, in this measurement, ratios of 0.7:0.4:0.2:1.0 were obtained, indicating that the afterpulsing in biases 1 and 2 was caused by the 2.2-MeV gamma rays as well as by the gamma burst since a larger-than-expected background which decays with a 17.6- μsec half-life is present in biases 1 and 2.

The second experiment was at the other extreme from multiple stops for each start; namely, single stop per start. In this case, only one stop was allowed per burst and the gamma flash was accepted in the spectrum. The stop was provided by the primary pulse, either from the gamma flash, 2.2-MeV gamma rays or neutrons, but not by an associated afterpulse (i.e., if the gamma flash was large enough to cause afterpulsing, the gamma flash itself would cause the stop). With this setup, the counting rate was much slower, but afterpulses were never counted. The resulting cross sections for all four biases were in 1 to 2% agreement with the evaluated cross section for hydrogen. The data were again binned in 2- μsec bins and the resulting ratios of 0.15:0.16:0.18:1.0 were obtained. This significant drop in the ratios for biases 1 and 2 from 0.70 to 0.15 and 0.40 to 0.16 again demonstrated that some of the counts in biases 1 and 2 for the previous multistop case were created by afterpulses which decay with the same 17.6- μsec half-life of the parent gamma ray.

Further runs were made with conditions intermediate between one stop per start which gave excellent results but considerably slowed the data acquisition rate and multistop per start which provided an adequate data rate but gave poor cross-section results. We will now describe some of these runs.

The next measurement was run in the single stop-per-start mode, except that the gamma flash was gated off logically; i.e., the detector system (scintillator + phototube) responded to the gamma flash, but no stops were accepted (by logic) until the gamma flash had passed. Thus, the earliest event in time which could produce a stop was an afterpulse from the gamma flash, and this would cause the system to remain dead until after the next gamma flash. Since about one burst in three resulted in a gamma flash large enough to detect and produce significant afterpulsing, the system would also be stopped by a valid neutron or a 2.2-MeV gamma ray but not by an afterpulse from one of these events. Thus, for this test we are sensitive to afterpulsing resulting only from the gamma flash. Data resulting from this measurement were converted to cross sections, and the results looked much like the cross sections for the multistop-per-start mode. In particular, cross sections extracted from biases 1 and 2 were very low, while the biases 3 and 4 cross-section results agreed with the hydrogen evaluation. These results imply that the afterpulses causing the problems are mainly due to the gamma flash.

The following measurement was also in the single stop-per-start mode, but rather than being gated off logically the phototube was gated at the base by defocusing the voltage for the second and fourth dynodes. Thus, the gamma flash produced light in the scintillator, but the phototube was much less efficient at amplifying it. The dynodes were brought back to normal potentials after the gamma flash passed, and the phototube was thus susceptible to some afterpulsing due to ion movement in the tube, as well as to the usual "late light" from the scintillator. Again, a neutron or a 2.2-MeV gamma ray could

provide a valid stop, but an afterpulse from one of these events would not produce a stop. These results for biases 1 and 2, when converted to cross sections, were better than results obtained when the logical gating was used but were still 30 to 40% low in biases 1 and 2. This measurement demonstrated that reducing the effect of the gamma flash reduced the magnitude of the afterpulsing problem.

The next measurement was done using the normal multistop-per-start mode, except if a gamma flash occurred in biases 2, 3, or 4 the burst was discarded. It was anticipated that a gamma flash occurring only in bias 1 would be too small to produce afterpulsing. This was checked and found to be correct. The resulting cross sections for biases 1 and 2 were a marked improvement over the normal multistop mode but still not as good as the benchmark single stop-per-start operation. Thus, it is clear that much (if not most) of the afterpulsing is due to response of the scintillator and phototube to the gamma flash. However, eliminating afterpulsing due to the gamma flash does not completely eliminate the problem.

Since the afterpulsing is due to large pulses, the next experiment was similar to the previous one except that, in addition to a gamma burst in biases 2, 3, or 4, a pulse (neutron or gamma) occurring in bias 4 at *any* time would also cause other stops from that burst to be discarded. Thus pulses resulting from the gamma flash, and large pulses from high-energy neutrons or 2.2-MeV gamma rays could cause a single stop-per-start mode of operation for that burst. Cross-section results extracted from these data were in 1 to 2% agreement with the evaluated hydrogen cross sections for all biases.

This series of tests have demonstrated that afterpulsing resulting from both the scintillator and the phototube gives rise to false events in biases 1 and 2 in addition to the true events. Thus, erroneous cross sections may be extracted from data in these bias levels. Data from biases 3 and 4 are unaffected by these afterpulses because of the higher discriminator settings. The afterpulses appear to come mostly from the gamma flash, and some from high-energy neutrons and the 2.2-MeV gamma rays emitted due to hydrogen capture in the water moderator surrounding the neutron target. Binning the cross sections for each bias level into wide (2- μ sec) bins facilitates the extraction of the background due to the 17.6- μ sec tail. The ratios of this background relative to bias 4 provide a quantitative estimate of the amount of afterpulsing due to this background. Gating on the gamma burst in biases 2 and 3, in addition to any event in bias 4, gives ratios basically in agreement with the one stop-per-start mode in which all effects of afterpulsing have been removed. By looking at the ratios determined with the present detector system, we find that this system is more sensitive to afterpulsing than some previous ones.

Based on results of these tests, we decided to take the nickel data in the multistop gated mode; in particular if a gamma flash occurred in biases 2, 3, or 4, or an event occurred in bias 4 at any time, the remaining burst was gated off. This seemed the best compromise between single stop-per-start and the desire to accumulate sufficient counting statistics in a reasonable length of time. Running in the gated multistop mode required a new deadtime correction program (CR81) which was thoroughly tested. In the process of testing this program, we also verified the deadtime of the data acquisition system as being 1104 ns following acceptance of a valid count. This is in agreement with the value used for a number of years. As a check, a 5.08-cm polyethylene sample with a 2.35-cm carbon compensator (set 1) was run and the hydrogen cross section extracted. These results will be discussed in the next section.

3.3 HYDROGEN TOTAL CROSS-SECTION TESTS

As noted above, a check was made on our new data acquisition method of selected gating by measuring the transmission through a 5.08-cm polyethylene sample with a matched 2.35-cm carbon compensator. The data were corrected for deadtime and background effects, in a manner similar to the nickel data which will be described in the following section. The hydrogen total cross section was extracted from these data from approximately 50 keV to 80 MeV, and the results were compared to 20

MeV with the ENDF/B-V evaluation (ST79) for hydrogen and results of Arndt (AR79) from 20 to 80 MeV. The results are shown in Figs. 5-7. In Figs. 5 and 6, we show a comparison for data extracted from each bias with the evaluation, and in Fig. 7 we show the percent difference to 20 MeV between the summed data for all four biases and the evaluation. From this latter figure, we see a systematic difference from 50 keV to 1 MeV, while above 1 MeV the experimental results are about 1.5% larger than the evaluated result.

A number of checks were performed to try to understand the source of these differences. The calculated number of carbon atoms in the polyethylene and carbon compensator agree to 0.14%. Another compensated set (set 2) was also measured with results very similar to those shown in Fig. 7. Similar tests with hydrogen were performed for a set of measurements (LA80), which covered the energy range from 2 to 80 MeV, in which the beryllium-block neutron source was used rather than the tantalum target used for the measurements in this report. The high-energy measurements were done in the multistop mode with no selective gating and used much higher discriminator cutoffs; bias 1 detected no neutrons below ~ 1 MeV. When those data were reduced and compared with the hydrogen evaluation to 20 MeV and results of Arndt (AR79) from 20 to 80 MeV, the data were found to agree within $\sim 0.5\%$. Thus, the samples do not appear to be the source of the problem.

Since the high-energy data were taken with the beryllium-block target, the present hydrogen measurements described above were also run with the beryllium block, with essentially no improvement over Fig. 7. A number of other checks, including changes in electronics, trying the single stop-per-start mode, small changes in discriminator bias levels, and different phototubes, were tried with essentially no improvements in the results. There are still some open questions regarding uniformity and purity of the polyethylene sample, for example, and this discrepancy is still under investigation.

4. DATA REDUCTION

Under the gated multistop mode of operation, the gamma flash is accepted in the spectrum. For the nickel sample-in, one gamma burst was observed for each 18 bursts produced; for the nickel sample-out, the ratio was one in seven. The distribution of the gamma burst among the bias levels for both sample-in and sample-out was as follows: 5% in bias 1, 10% in bias 2, 11% in bias 3, and 74% in bias 4. During the course of a run, channels containing the gamma flash would overflow, particularly in bias 4. These were corrected at the end of the run. Accepting the gamma flash as part of the spectrum also had the advantage of allowing continual monitoring of the centroid of the gamma flash which defines the energy scale. During the nickel runs no drifting was observed, and the centroids in the four bias levels were equal to within a 1-ns channel.

4.1 DEADTIME CORRECTIONS

Following corrections for channel overflows, the data were corrected for deadtime effects. As noted in the previous section, the data acquisition system operated in a single stop-per-start mode if (a) the event was identified in time as a gamma flash and occurred in biases 2, 3, or 4, or (b) an event occurred in bias 4 at any time. If the event occurred anywhere else (i.e., any event in bias 1, or an event in biases 2 or 3 occurring after the gamma flash), the system operated in a multistop-per-start mode. Thus, when an event met these requirements, the system was disabled for $\Delta t = 1104$ ns to process the count and then was enabled to wait for another count from that burst. Thus, under certain conditions which are associated with minimal phototube afterpulsing, more than one event could be detected from a burst, hence increasing the data acquisition rate. The multiplicative deadtime correction for channel j can be expressed as

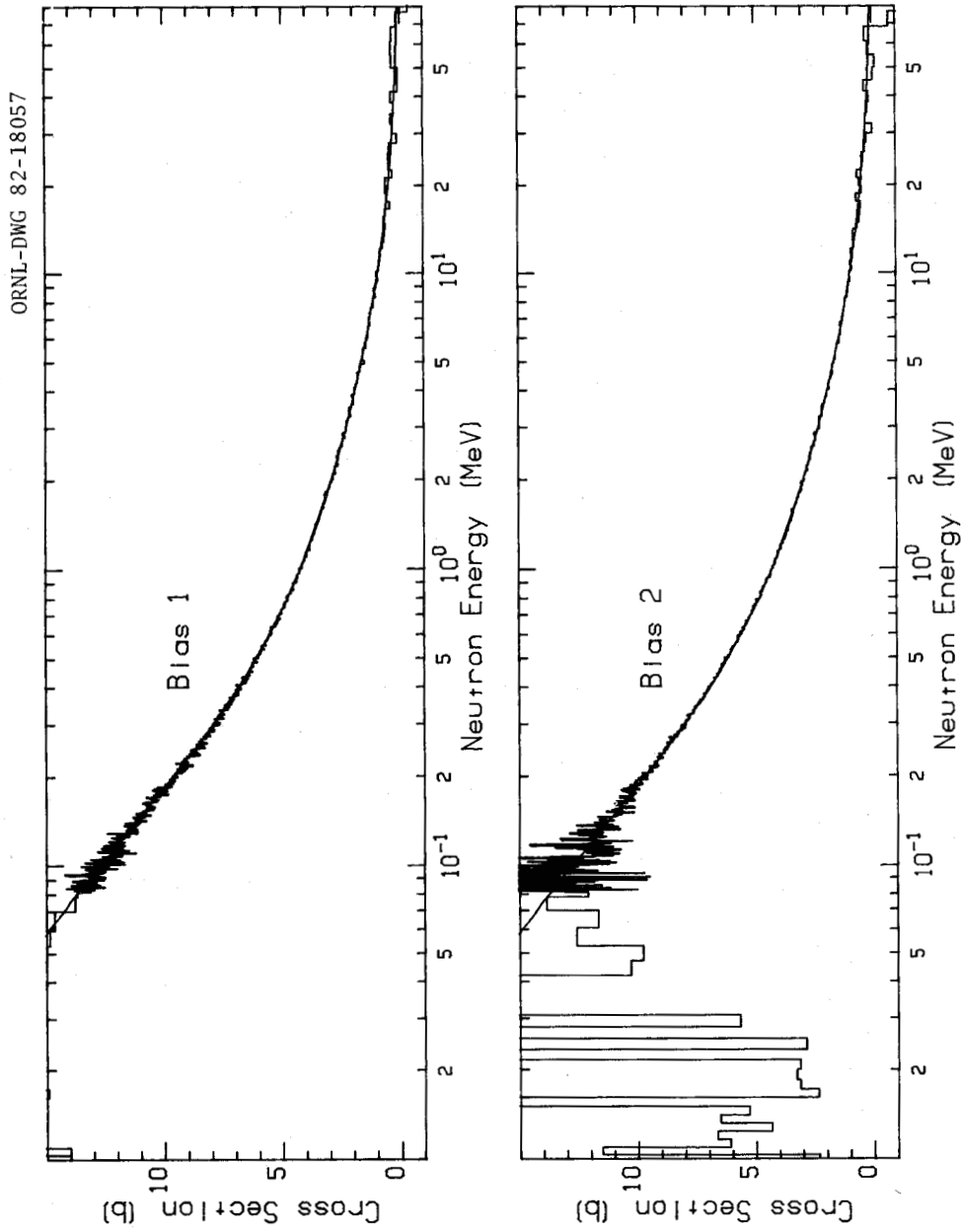


Fig. 5. Comparison of the hydrogen total cross section extracted from bias 1 and bias 2 data with the hydrogen ENDF/B-V evaluation. The data were taken in the gated multistop mode used for the nickel measurement.

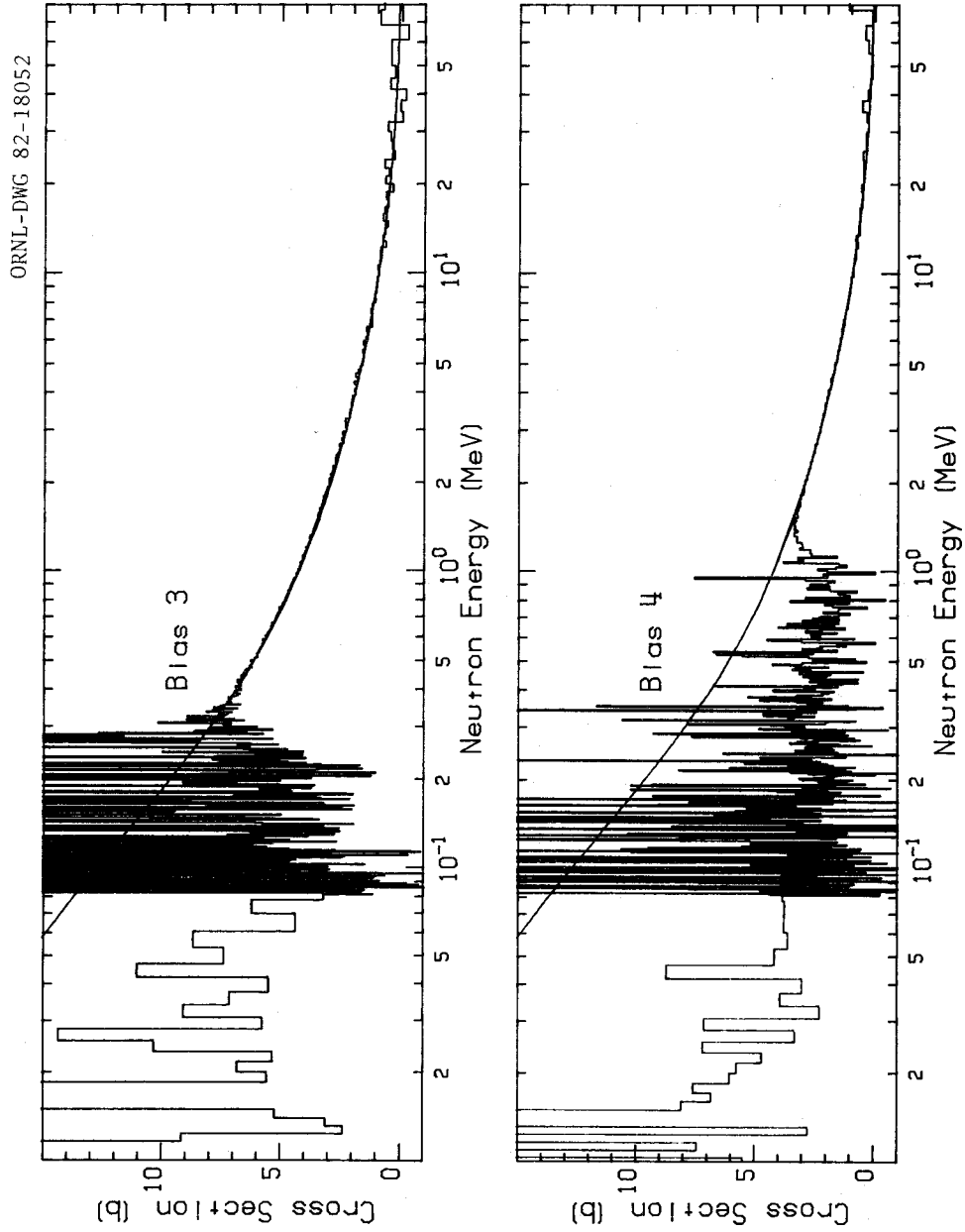


Fig. 6. Comparison of the hydrogen total cross section extracted from bias 3 and bias 4 data with the hydrogen ENDF/B-V evaluation. The data were taken in the gated multistop mode used for the nickel measurement.

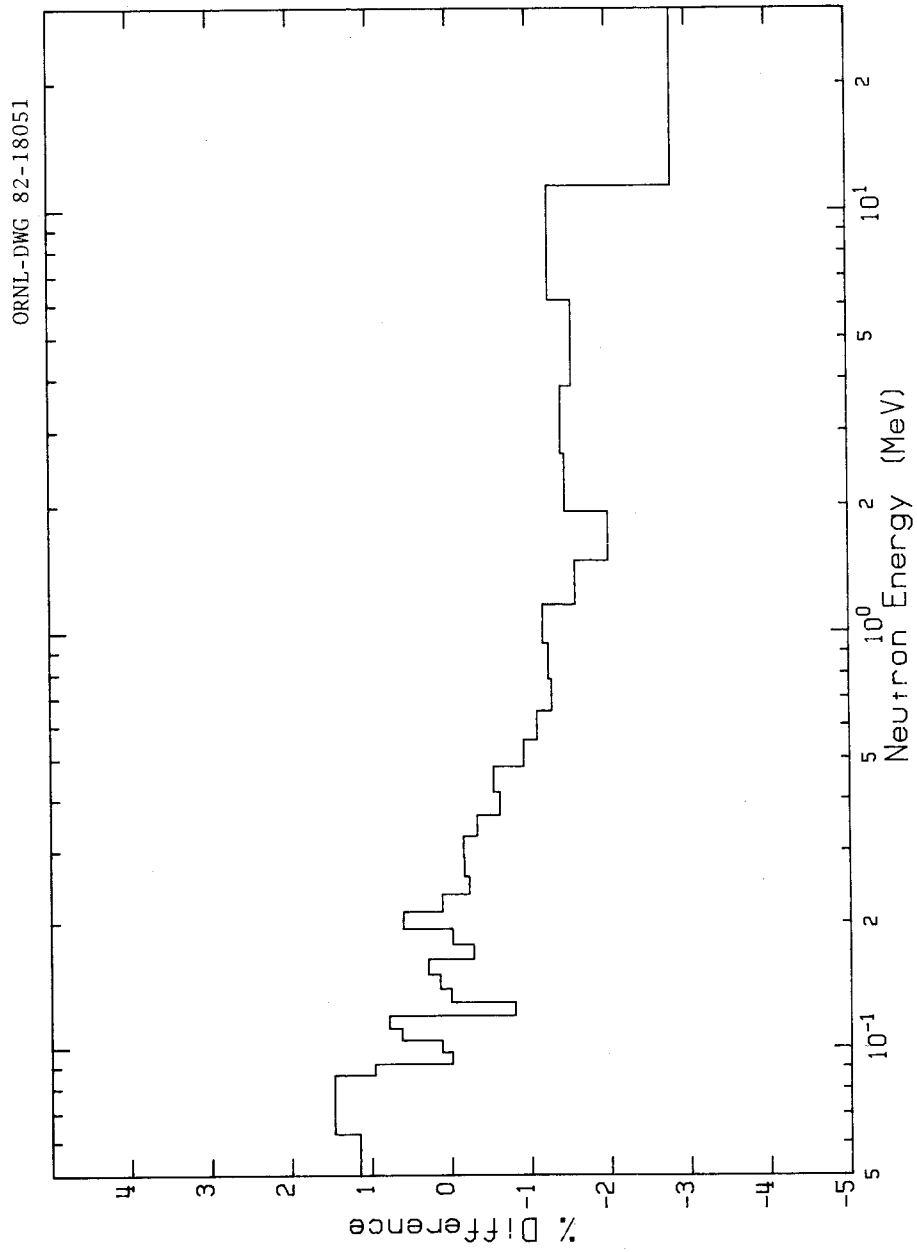


Fig. 7. Percent difference (EVAL-EXPT)/EVAL between our hydrogen total cross section and the ENDF/B-V evaluation. The low bin above 10 MeV comes mainly from averaging two statistically high cross-section bins in bias 3 of our measurement. The percent difference has been averaged by 15 for this plot.

$$D_j = \frac{1}{1 - \frac{A \left[\sum_{k=1}^4 \left(\sum_i C_i + C_j/2 \right)_k \right]}{T}} \quad (4.1)$$

where the normalization constant $A = 1 + \sigma^2$ (in anticipation of results on the following page), and T represents the number of bursts for the run. The sum over i represents a sum over selected channels in the k^{th} bias level spectrum; the range of the sum over i depends on the bias level k . For bias 1, counts are summed for channels corresponding to 1104 ns prior to channel j ; for the bias 2 and 3 spectra, counts are summed for channels containing the gamma flash, in addition to channels corresponding to 1104 ns prior to channel j , and for the bias-4 spectrum counts are summed for *all* channels prior to channel j .

However, this expression for the deadtime correction contains an inherent assumption that both intensity and shape of the incident neutron distribution do not vary with time. This assumption is not valid, since there are both pulse-to-pulse variations in the neutron intensity as well as long-term drifts in the ORELA power. To estimate the intensity variations over short periods of time (a few seconds), we integrate the current output of a bare photomultiplier tube which directly views the target. We are thus measuring the burst-to-burst intensity variation of the gamma flash, and we assume a proportionate variation in the number of neutrons from burst to burst. We find that this short-term distribution of intensities can be well approximated by a Gaussian shape. This component of the intensity variation is described in terms of the standard deviation σ_0 of a normal distribution whose mean is 1.0. Measurements of this short-term intensity variation show a dependence of the effect on the operating parameters of the accelerator, and electron gun condition, and appear to be largest for narrow pulse conditions, with $\sigma_0 = 0.14 \pm 0.04$ for conditions similar to those for measurements described in this report. Since realization of the possible importance of this correction was a result of the uncertainty analysis of this measurement, measurements of σ_0 for the short-term intensity variations were not made during the nickel run. This rather crude way of estimating the short-term neutron intensity variation is essentially an integral result and provides no information on the possible burst-to-burst variation in the neutron spectral shape.

The second component of the intensity variation is associated with the long-term (>15 minutes) drifts in ORELA power. Power is monitored on a chart recorder as part of the regular operating procedure. Due to the long-time constant of the chart recorder, no indication of pulse-to-pulse variation is observed. Long-term drifts can be caused by many things, including the electron gun, modulator power, and other factors beyond control of the experimenters. These long-term drifts can have an effect both on the sample-in to sample-out normalization as well as on the deadtime correction. The normalization problem is discussed in detail in Sect. 5.1.2, and here we deal only with the intensity variation problem as it relates to the deadtime correction. As part of our experimental procedure, we cycle the sample-in and -out of the beam about every 10 minutes, the exact time depending on detection of a preset number of valid events (Sect. 5.1.2). For each cycle we store, among other parameters, the number of bursts and number of events detected in the neutron monitor detector ("house monitor"), which monitors the neutron production from the ORELA target. The distribution of the ratios of house monitors to bursts (m_k/T_k) gives an estimate of the long-term intensity variation. For the 67-cycle (~26-hour) run described in Sect. 5.1.2, we have calculated the standard deviation associated with the dispersion of these ratios about the mean values and found a standard deviation of 3.1% for sample-in and 3.3% for sample-out. Thus, for the present measurement with narrow pulse width (~7 ns), the short-term intensity variations (~14%) are much greater than the long-term variations (~3%). This is not a general result, of course, and depends on machine conditions during the particular measurement.

We now need to relate this information on the magnitude of the intensity variation to the deadtime correction. In Appendix A, we derive an expression for the deadtime correction which properly includes the effect of variations in neutron intensity. This result, derived in a rigorous fashion, is essentially the same as that obtained in ref. MO80. The result is to replace the term A in Eq. (4.1) by $A = 1 + \sigma^2$, where σ^2 is the variance of the distribution describing the combined intensity variations due both to pulse-to-pulse variations and long-term drifts. In Appendix B, we derive a relation for the quantity $(1 + \sigma^2)$ in terms of the measured standard deviation for the short-term pulse-to-pulse variation, and the individual ratios of m_k/T_k for the k^{th} 10-minute cycle. This result is

$$1 + \sigma^2 = (1 + \sigma_0^2) \left[\frac{T}{m^2} \sum_{k=1}^K \frac{m_k^2}{T_k} \right]$$

where σ_0^2 is the observed variance of the pulse-to-pulse variation, T is the sum of the bursts for the run, K is the number of cycles for the run, and m is the sum of the monitor counts for the run. Note that if there is no long-term variation in neutron intensity, the term in brackets is identically equal to unity, and the total correction is given by the pulse-to-pulse result. Also, if σ_0^2 is very small, the total intensity variation correction is dominated by the long-term drifts.

These results are useful for studying possible effects on existing data where the deadtime corrections may have been large enough to warrant such re-analysis. The long-term drift information (i.e., m_k and T_k) is stored for each run, but one has to make an assumption regarding the magnitude of σ_0^2 . For future runs, the total σ^2 can be measured simply by monitoring the intensity variation for the full duration of a run, utilizing the pulse-to-pulse measuring equipment.

Finally, the deadtime corrections applied to the data in this report were consistent with Eq. (4.1), with $A = (1 + \sigma^2)$. The largest corrections were around 1 MeV and were a factor of 1.23 for the sample-in spectrum and 1.56 for the sample-out spectrum. The deadtime corrections are shown in Fig. 8. Uncertainties associated with these corrections will be presented in Sect. 5.2.2 of this report.

4.2 BACKGROUND REMOVAL

The deadtime corrected data were then corrected for backgrounds. A general expression for our background is

$$B = \alpha + \beta e^{-t/\tau} + [(at + f) + e + g/t^k] \text{ cts/ns} \quad (4.2)$$

where t is the time-of-flight, α represents the time independent background, and $\beta e^{-t/\tau}$ represents a background due to the $H(n,\gamma)$ reaction in the water moderator surrounding the neutron producing target (the value of τ is normally taken as 25.4 μsec). The term enclosed in square brackets represents the background in three different time regions due to the $^{10}\text{B}(n,\alpha\gamma)$ reaction which occurs in the boron component of the Pyrex face of the phototube. This background is taken as zero for $t < 3 \mu\text{sec}$, linear ($at + f$) for $3 < t < 17 \mu\text{sec}$, constant (e) for $17 < t < 26$, and g/t^k for $t > 26 \mu\text{sec}$, with $k = 1$ for sample-out and $k = 2$ for sample-in. Each component of these backgrounds will now be described in detail.

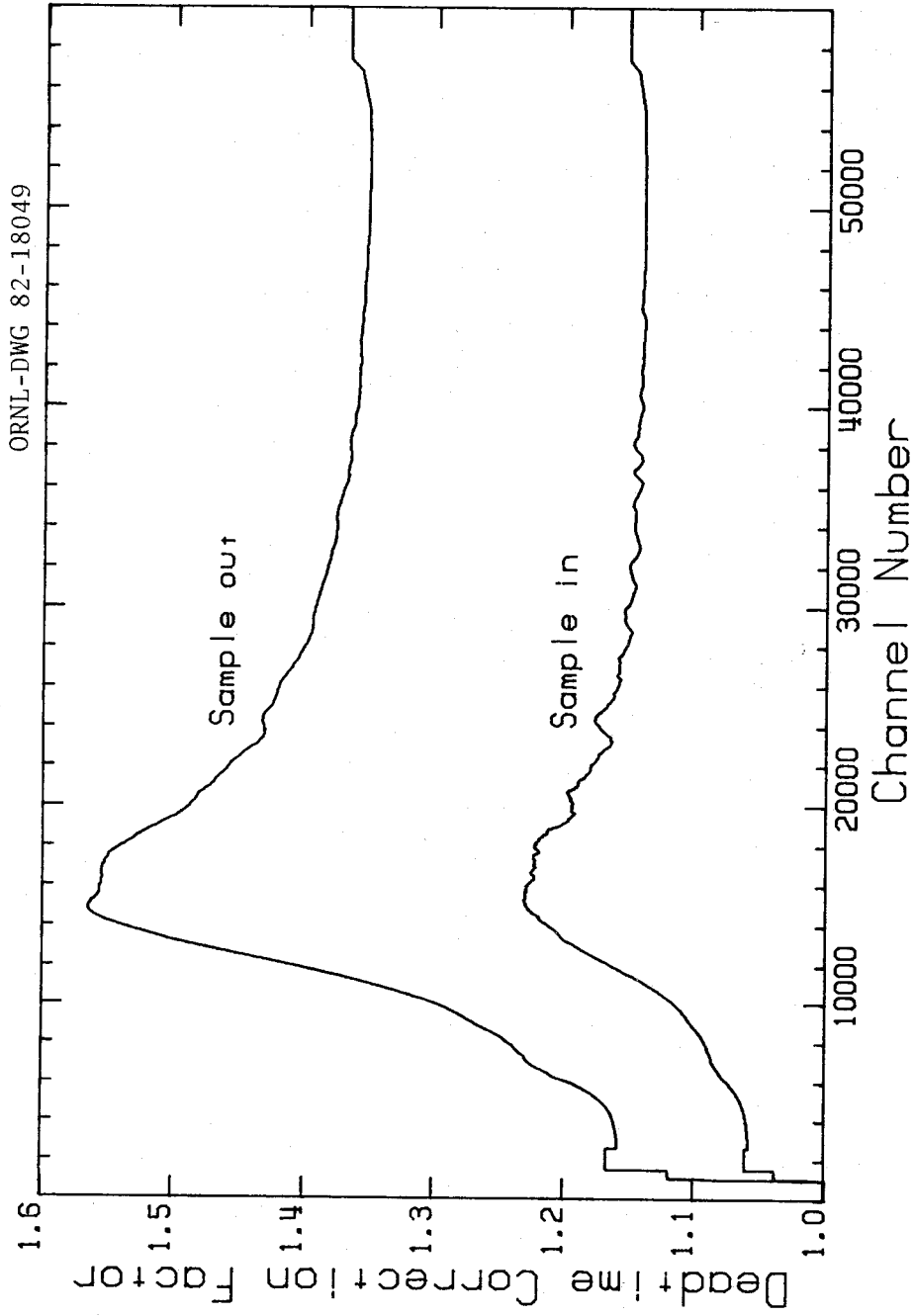


Fig. 8. The deadtime correction factor is plotted as a function of channel number for both sample-in and sample-out for the nickel measurement. The measurement extends to channel 57410.

4.2.1 Time-Independent Background

The pulse repetition rate was 780 Hz for the nickel measurement, resulting in 1282 μsec between bursts. However, the clock was disabled at 1125 μsec following a burst. Below 50 keV, the efficiency of the NE110 detector decreases with decreasing neutron energy such that neutrons arriving at the detector later than $\sim 600 \mu\text{sec}$ ($\sim 600 \text{ eV}$) following a burst are not directly registered by the detector. At these long times, the main contributing term to the background is the time-independent term α . Contributions to α include gamma rays present from various induced activities in the 200-m station as well as long-lived gamma-ray radiation from the neutron source which produce a time-independent gamma-ray background in the NE110 detector. Background measurements made when ORELA is not operating are $\geq 88\%$ of the background extracted at long times from our data. Hence $\leq 12\%$ of the background at long times is machine associated. We assume it is time independent and treat it as a part of the true time-independent background. To estimate and remove the time-independent background for sample-in and sample-out for each bias, the counts are averaged from 1025 to 1125 μsec , and a small correction ($< 5\%$) is made for the effect of the observed 190-eV resonance in the ^{238}U filter based on its observed effect in bias 3 due to the $^{10}\text{B}(n,\alpha\gamma)$ reaction. This constant background is then assumed to be the total background present at long times and is subtracted. Plots for each bias are then made to verify that remaining backgrounds at long times (where the useful neutrons are gone) are negligible.

4.2.2 Background Due to 2.2-MeV Gamma Rays

In the following discussion, it is always assumed that the time-independent background has been removed. One source of time-dependent background is due to the 2.2-MeV gamma ray resulting from neutron moderation and capture in the cooling water surrounding the ORELA target. The effective half-life of the gamma ray has been measured to be 17.6 μsec (mean life of 25.4 μsec) which is in good agreement with Monte Carlo calculations (KI72) of neutron leakage from the source. To determine this background, in a separate measurement we put a 20.3-cm polyethylene filter in the beam; this removes neutrons below $\sim 1 \text{ MeV}$ (16 μsec), leaving the 2.2-MeV gamma rays as the major source of counts for times $\geq 16 \mu\text{sec}$. These data are crunched into 2- μsec bins to facilitate extraction of this background. The binned data for $t \geq 16 \mu\text{sec}$ were least-squares fitted with a form $\beta e^{-t/25.4}$ to extract the magnitude of this time-dependent background. As noted earlier, the largest contribution of this background source is observed in bias 4, and contributions to other biases are obtained by scaling the result for bias 4 by the ratios 0.15:0.16:0.18:1.0 (see Sect. 3.2). This separate measurement was too short to observe statistically significant counts in any but bias 4.

The corresponding background coefficient β for the nickel measurement was deduced from this observed background by first correcting for transmission of the 2.2-MeV gamma ray through 20.3 cm of polyethylene and 2.5 cm of nickel, and then normalizing by the relative number of triggers for the two measurements. This background is small due to the 3.8 cm of ^{238}U in the beam, and its main effect is at high energies (bias 4) at short times.

It should be noted that extraction of this time-dependent background directly from the nickel data is difficult due to the smallness of the background. Simply fitting the time-dependent exponential background to the counts remaining in bias 4 after the primary neutrons have been cut off by the discriminator (i.e., after $\sim 16 \mu\text{sec}$) gives a β coefficient approximately five times larger than obtained from the hydrogen data described above, where the low-energy neutrons have been removed by the polyethylene. In addition, the ratio of the β coefficients for bias 4 to bias 3 should be 1.0:0.2. However, extracting the β 's directly from the nickel data gives a ratio 1.0:1.5. This implies that the counts after passage of the primary neutrons (in particular, for bias 3) are only partly due to the 2.2-MeV gamma-ray time-dependent background, and mainly due to the $^{10}\text{B}(n,\alpha\gamma)$ background.

4.2.3 Background Due to the $^{10}\text{B}(n,\alpha\gamma)$ Reaction

The face of the RCA-8854 phototube used in these measurements is made of Pyrex which contains boron. The $^{10}\text{B}(n,\alpha\gamma)$ reaction produces a 477-keV gamma ray to which our NE110 plastic scintillator is sensitive. The cross section for this reaction increases with decreasing neutron energy, and so our detector system is sensitive to low energy neutrons. As an example, we observe the 190-eV resonance in ^{238}U in the time-of-flight spectrum for bias 3. (Recall that we have 3.8 cm of uranium in the beam as a filter to reduce the magnitude of the gamma flash.) Observation of this resonance can be understood as follows. The transmission of the NE110 plastic scintillator is $\sim 9\%$ for 190-eV neutrons, so only 9% of the 190-eV neutrons pass uncollided through the NE110 and are directly available to induce the $^{10}\text{B}(n,\alpha\gamma)$ reaction. The mean free path (mfp) for a 190-eV neutron in NE110 is ~ 0.8 cm, so our detector is ~ 2.4 mfp thick. This implies multiple scattering occurs in the NE110, and this has been estimated with the O5S (ref. TE68) Monte Carlo code. We find an average of 2.7 collisions per neutron, most of which are with the hydrogen in the NE110. We have also studied the energy and time spectra of neutrons emitted from the face of the NE110 adjacent to the phototube face (about 60% of the incident neutrons) in order to estimate the time dependence of the 477-keV gamma ray resulting from the capture of neutrons in the boron of the phototube. Since the $^{10}\text{B}(n,\alpha)$ cross section is proportional to $1/v$, the neutrons which slow down in the NE110 have a larger probability of inducing this reaction than the 9% which pass through uncollided. In order to estimate the time distribution of the 477-keV gamma rays, we have modified the time spectra of neutrons emitted from the face of the NE110 to correct for the angle of emission (since neutrons emitted at angles other than 90° to the face of the NE110 pass through a greater thickness of the phototube face) and the energy dependence of the cross section. The resulting time spectrum for the 477-keV gamma rays is approximately exponential with a half-life $< 0.5 \mu\text{sec}$. From the ^{238}U transmission measurement of Olsen et al. (OL76), we find that for their 3.8-cm-thick sample the minimum of the 190-eV resonance is ~ 5 eV wide, which corresponds to $\sim 15 \mu\text{sec}$ in our measurement. Since the resonance is much wider in time than the delay due to the $^{10}\text{B}(n,\alpha\gamma)$ detection process, the 190-eV resonance is observed at the expected time-of-flight.

The neutrons which escape from the NE110 in some direction other than into the phototube face have a small probability of reflecting off the walls (~ 2 m away) or the floor (~ 1 m) back into the phototube, and these scattered neutrons make up some of the 12% of the time-independent room background which is beam associated.

After removal of the time-independent background and time-dependent background due to neutron capture in the water moderator, we are left with the background due to the $^{10}\text{B}(n,\alpha\gamma)$ reaction. The discriminators which determine the bias levels were set such that $\sim 50\%$ of this background falls in the bias-3 spectrum. Ideally, we like to isolate more of this background in bias 3 to achieve a better separation of the $\text{H}(n,\gamma)$ background (in bias 4) and this background (in bias 3). To get the amount in the spectra for biases 1, 2, and 4, an auxiliary measurement was performed when the machine was off. A ^7Be source which emits the same 477-keV gamma ray as the $^{10}\text{B}(n,\alpha\gamma)$ reaction was placed on the face of the detector, and the distribution of counts among the four biases was measured. A gamma-ray spectrum was taken for the ^7Be source with a Ge(Li) detector to insure no significant contaminant gamma rays were present. After correcting for deadtime and background effects, these ratios relative to bias 3 are observed to be 0.15:0.32:1.00:0.60 for biases 1, 2, 3, and 4. For the nickel measurement, integrating the remaining counts in each bias, following removal of the backgrounds discussed previously, we find the ratios 0.14:0.27:1.00:0.54, which are in acceptable agreement with the expected $^{10}\text{B}(n,\alpha\gamma)$ ratios. In addition, the magnitude of the spectral shape from bias 3 for $t > 31 \mu\text{sec}$ was normalized to biases 1, 2, and 4 using the measured ratios, and the spectral shapes of the renormalized backgrounds were compared to the bias-3 shape and found to be in good agreement.

For the sample-in data, the low-energy neutrons in the beam which induce the $^{10}\text{B}(n,\alpha\gamma)$ reaction are attenuated by $\geq 90\%$, i.e., most are removed by the nickel. Thus, we observe that this background is negligible for times $t \geq 200 \mu\text{sec}$ ($E \leq 6 \text{ keV}$). The background from 31 to 200 μsec is roughly proportional to E , although the large nickel resonances are observed. For sample-out, however, the low-energy neutrons are not removed, and the shape of this background spectrum is approximately proportional to \sqrt{E} for $31 < t < 1000 \mu\text{sec}$. As expected, the shape of the background for sample-in and sample-out is dependent on the beam filtering material, the neutron source, and the sample properties, so general conclusions cannot be drawn about these background shapes.

This background presents a particular problem in that there is no clear way to understand the shape of the background for times $t < 31 \mu\text{sec}$ since it is masked by the neutrons of interest in bias 3, where its effects are largest. We now describe our method of estimating this background for $t < 31 \mu\text{sec}$.

Looking at the flux shown in Fig. 3 at short times ($t < 14 \mu\text{sec}$), we see that it is rapidly decreasing with decreasing time, so this background must also be decreasing since it is proportional to the flux. In addition, the cross section for $^{10}\text{B}(n,\alpha\gamma)$ decreases with increasing neutron energy (decreasing time). Finally, the estimated moderation efficiency for NE110 is calculated to be $\sim E^{-1/2}$ (KI72), because neutrons are slowed down with less efficiency at the higher energies. Thus, estimating effects on this background at short times due to moderation efficiency of NE110 for high-energy neutrons, detector efficiency, and flux shape, we tried a background which is linear in time as a reasonable approximation for the $^{10}\text{B}(n,\alpha\gamma)$ background for $4 < t < 31 \mu\text{sec}$. However, this overestimates the background from ~ 20 to $30 \mu\text{sec}$, where it should be approximately flat, by at most 50%. To correct for this, we assume a time-independent constant term for this time region. Thus, summarizing this background, we have (a) zero up to 3 μsec , (b) linear in time from 3 to 17 μsec , (c) constant from 17 to 26 μsec , and (d) decreasing as t^{-k} for time greater than 26 μsec , where $k = 1$ for sample-out and 2 for sample-in. For times $t > 31 \mu\text{sec}$, this background component [due to the $^{10}\text{B}(n,\alpha\gamma)$ reaction] is removed by subtracting the appropriate fraction of the *measured* bias-3 spectrum from each of the four bias spectra, in proportion to the ratios obtained using the ^7Be source. This is preferred to utilizing the analytical form g/t^k , since the fit is not exact, in particular at long times where the background is small and where there are large resonances. However, for times $t < 31 \mu\text{sec}$, we must use the analytic form since the background, although present, is masked by the data. Thus the magnitude and shape of the $^{10}\text{B}(n,\alpha\gamma)$ background is based only on heuristic arguments and empirical observations for $t < 31 \mu\text{sec}$, and has large uncertainties associated with it. Thus, for $t < 31 \mu\text{sec}$, the data are corrected with the same approach as for $t > 31 \mu\text{sec}$, but using analytical forms for the background.

In the present measurement with the 7.9-cm-long shadow bar in place, approximately equal areas of (a) the tantalum target and (b) the cooling water moderator are viewed. This arrangement yields fewer hydrogen capture and low-energy neutrons which produce the $^{10}\text{B}(n,\alpha\gamma)$ backgrounds than the other commonly used mode of operation (mainly for small samples) in which a collimator is used such that only the cooling water moderator is viewed. The latter mode of operation produces a softer neutron spectrum, with attendant increases in the backgrounds discussed above. In addition, the shape of the $^{10}\text{B}(n,\alpha\gamma)$ background tends to be flatter (approximately energy independent) when only the moderator is viewed.

Figure 9 shows the total background for the sample-out spectrum as a percentage of sample-out counts. We note that the backgrounds are less than 1% of the sample-out counts from 32 keV to 21 MeV. At higher energies (shorter times), the time-independent and $\text{H}(n,\gamma)$ backgrounds become proportionally more important as the flux is rapidly decreasing. At long times the detector efficiency is decreasing and the time-independent background becomes the important term. It is apparent that the backgrounds are small over the main energy region of interest.

ORNL-DWG 82-18050

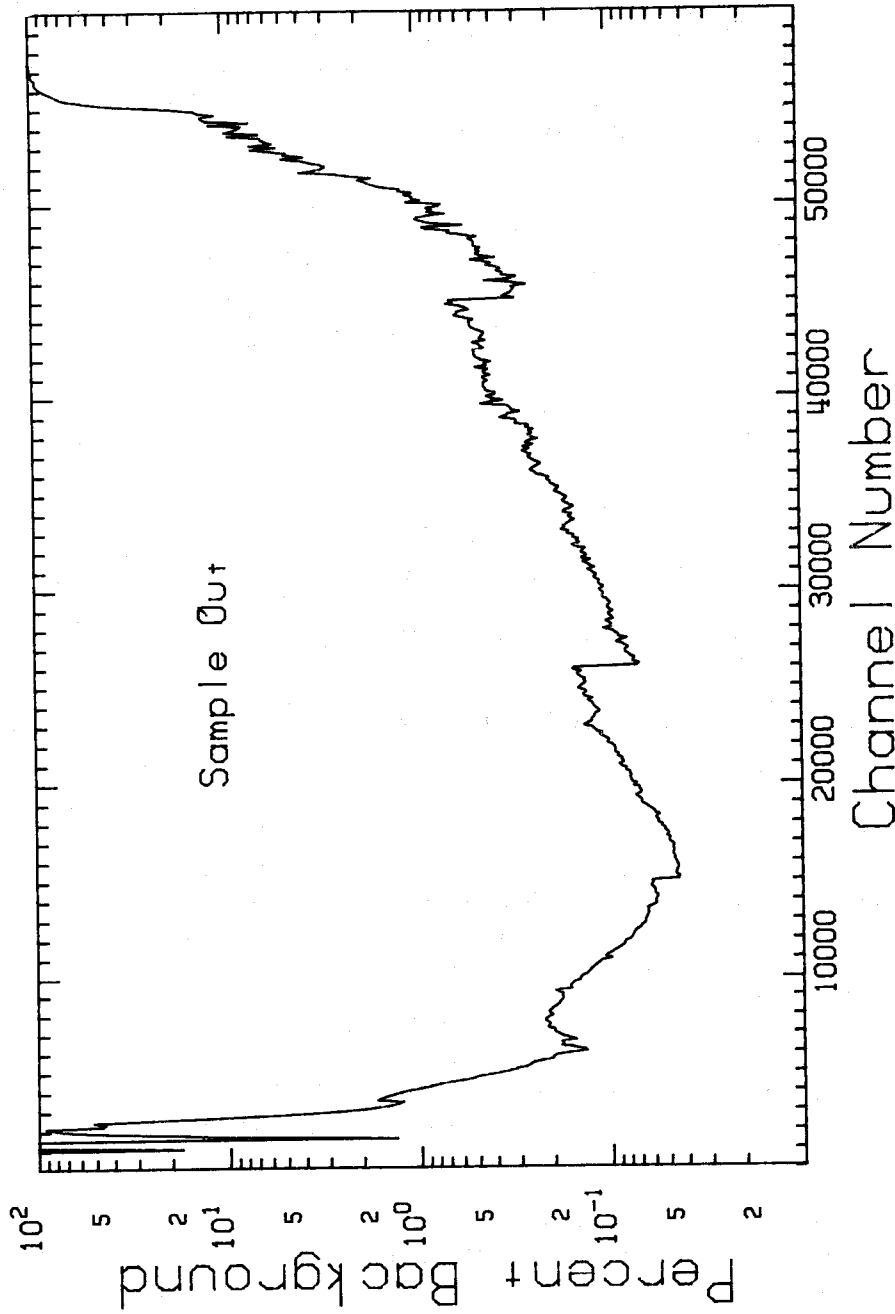


Fig. 9. The percentage background for sample-out is plotted as a function of channel number. The background is less than 1% of the total counts from 32 keV to 20 MeV. The steps result from bin width changes in the data, and selective summing of data from each bias.

Values of the background parameters are given in Table 2 for each bias level for both sample-in and sample-out. They have not been normalized to the monitor counts. The values are in units of counts per 1-nsec channel and must be multiplied by the channel widths given in Table 1 to obtain the appropriate background where channels wider than 1 nsec are used.

Table 2. Values of background parameters as a function of bias level for sample-in and -out for the nickel measurement. The uncertainty in percentage for each parameter is also given. Sample-out values are in parentheses and all values are given in units of counts per 1-ns channel.

Parameters	Bias level				Uncertainty
	1	2	3	4	
α	1.26 (0.91)	1.87 (1.33)	2.31 (1.64)	1.64 (1.16)	4
β	0.10 (0.18)	0.10 (0.19)	0.11 (0.21)	0.63 (1.18)	25
a	0.02 (0.03)	0.05 (0.06)	0.15 (0.19)	0.09 (0.12)	50
f	-0.06 (-0.09)	-0.15 (-0.18)	-0.45 (-0.57)	-0.27 (-0.36)	50
e	0.32 (0.40)	0.68 (0.87)	2.13 (2.66)	1.27 (1.62)	30
g	215 (10.5)	460 (22.5)	1440 (69)	860 (42)	20

4.2.4 Other Possible Sources of Backgrounds

The three backgrounds discussed earlier are relatively easy to determine during the run or to obtain from additional measurements before or after the run. However, there are also backgrounds which arise from the "good" neutrons which are detected at a somewhat "wrong" time (a few percent of the flight time). These backgrounds are very small; it is difficult to establish their presence and measure them accurately. Since these backgrounds have the same sample transmission as the "good" neutrons, they do not produce any appreciable uncertainty in the cross section, if the cross section varies slowly with energy.

Backgrounds of this type can arise from several sources. The most obvious is from "good" neutrons which are scattered from material at the 200-meter station (e.g., the NE110 scintillator, the 0.4-mm Al window \sim 50 cm before the detector and the air between the window and the detector) and return to the detector at a later time (a few percent of the neutron flight time) after scattering from the air around the detector or from the walls of the detector station. Neutrons which are delayed much longer than this probably make up part of the 12% increase in time-independent background over the ambient background, when ORELA is operating (Sect. 4.2.1). However, no pulses can result from "returned" neutrons within 1104 nsec of a neutron scattered from the NE110 scintillator if that scattered neutron produced a measurable pulse since the time digitizer will not be alive due to the deadtime of the time digitizer (clock).

Another time-dependent background can arise from neutrons scattered from the walls of the target room back to the ORELA target and then scattered down the flight tube at a somewhat later time than neutrons of the same energy coming directly from the target. For the Columbia NEVIS high-resolution pulsed-neutron source, this was a large background (\sim 10%) since the neutron target was located between the poles of the cyclotron magnet. In fact, Bill Havens has called this arrangement the largest iron moderated neutron source in the world. Neutrons from the iron which are scattered by the target down the flight tube to the detector produce a long important tail on the resolution function.

A time-dependent background can arise also from the "dark" current in the accelerator, which can produce neutrons over an $\sim 2 \mu\text{sec}$ time period before and after the primary pulse. A 5-nsec, 10-amp linac pulse and an average dark current of 250 μamps over a 2- μsec time period would result in a background of $\sim 1\%$ (assuming the neutron production is as efficient as during the main pulse). Using the selected gating technique, part of the background arising from the dark current can be monitored during the run by measuring the counts from the detector for 100-200 nsec before the gamma flash peak arrives at the detector. For the present measurement, inspection of the data at early times shows that this is a negligible effect. After-pulsing many hundreds of nanoseconds after the main pulse can also be considered a background. A "secondary" gamma flash peak can be observed in the spectrum if after-pulsing is occurring, and the run is stopped if this is large enough to cause a problem. For the present measurement, no significant machine afterpulsing occurred.

These backgrounds are all very small and the estimation or determination of them are difficult. For low-energy neutrons $< 10 \text{ keV}$, a "blacking-out" resonance technique has been used by several experimenters, where various thicknesses of samples are used. The backgrounds at the bottoms of these resonances are observed to decrease with increasing sample thickness. An open-beam background is derived by extrapolation to zero thickness sample. Techniques such as the black and white filter method developed by D. B. Syme (SY82) may be helpful; however, it is probably not sufficiently sensitive to the very small backgrounds in the present experiment.

In experiments using a ^6Li glass scintillation detector at 80 meters at ORELA, the backgrounds other than the 17.6- μsec , 2.2-MeV gamma rays from the target, and the time-independent room background and any overlap neutrons may be as large as $\sim 0.5\%$. This is estimated from the background at the bottom of "blacking-out" resonances in ^{238}U and in Fe transmission data after correcting for these other backgrounds. For neutron energies below $\sim 50 \text{ keV}$ this scattered-neutron background is expected to be somewhat smaller for the NE110 detector than for the ^6Li scintillation detector. From a study of the blacking-out resonances in the present nickel transmission data with the NE110 detector, we conclude that these additional backgrounds are probably $< 0.1\%$ in the regions they can be investigated.

4.3 CONVERSION OF CORRECTED DATA TO CROSS SECTIONS AND ENERGIES

Following removal of the time-independent, hydrogen capture and $^{10}\text{B}(n, \alpha\gamma)$ backgrounds, regions of each bias spectrum were selected, based on total counts and maximum count-to-background ratio, and summed to form the final spectra for both sample-in and sample-out. The regions chosen from each bias for inclusion in the final spectra are given in Table 3.

Table 3. Channels from each bias included in the final spectra for sample-in and sample-out

Bias level	Channels	Energy (MeV)
1	3500 - 60,000	1.8×10^{-4} - 30
2	3500 - 45,000	0.11 - 30
3	3500 - 26,000	0.34 - 30
4	1 - 15,000	1.1 - 30

Parameters for the background, corresponding to the groups of channels selected from each bias, were also summed and, for convenience, are given in Table 4. In addition to the boundaries introduced by the contributing channels from each bias, additional boundaries are required for the different representations of the $^{10}\text{B}(n,\alpha\gamma)$ background as a function of channel.

Table 4. Background parameters for summed spectra
Sample-out values are given in parentheses.

Channel boundaries	α	β	a	f	e	g
1 - 3,000	1.64 (1.16)	0.63 (1.18)				
3,001 - 3,500	1.64 (1.16)	0.63 (1.18)	0.09 (0.12)	-0.27 (-0.36)		
3,501 - 15,000	7.08 (5.04)	0.94 (1.76)	0.32 (0.40)	-0.96 (-1.20)		
15,001 - 17,000	5.44 (3.88)	0.31 (0.58)	0.22 (0.28)	-0.66 (-0.84)		
17,001 - 26,000	5.44 (3.88)	0.31 (0.58)			3.13 (3.93)	
26,001 - 45,000	3.13 (2.24)	0.20 (0.37)				675 (33)
45,001 - 60,000	1.26 (0.91)	0.10 (0.18)				215 (10.5)

The sample-in and sample-out spectra were then normalized to the house-monitor counter; ratios of these spectra were formed, combined with the sample thickness, and converted to cross sections as a function of energy. An interactive computer program was then used to select regions of the cross-section data to be averaged and choose the averaging factor. With the averaging boundaries determined, the code averaged the sample-in and sample-out *counts* (not transmissions or cross sections) to get the desired average cross sections. This reduced the number of data points from 60,000 to 13,696 covering the energy range from 2 keV to 20 MeV.

After this report was essentially finished, a study was done to determine the energy dependence of the flight path length and the resolution function. Those results are reported in ORNL/TM-8880 (LA83), and the energies given in the present report were calculated using results from ORNL/TM-8880.

5. UNCERTAINTY ANALYSIS

The uncertainty on a data point may be described in terms of the various components which contribute to that uncertainty. A major component is the statistical uncertainty which is simply the square root of the measured counts for the data point, and this uncertainty is uncorrelated with all other data points. The second component of the uncertainty on a data point is described as the systematic uncertainty which contains all other sources of uncertainty that can be identified for a given measurement. Systematic uncertainties may be correlated over some energy range. We now discuss in detail the systematic uncertainties identified in our measurements and present these results in terms of a correlation matrix and standard deviations. Since we have measured 60,000 data points, these results must be presented in some reasonable energy group structure of a manageable size. We have chosen to use a 15-group substructure of a 26-group set (MA80) used frequently in fast-reactor calculations. The energy boundaries of the groups are given in Table 5. The gaps in energy which occur for some of the low-energy groups correspond to blacking out resonances in our data.

Table 5. Energy groups used for uncertainty analysis

Group number	E_{MIN} (MeV)	E_{MAX} (MeV)
1	0.022	0.028 ^a
2	0.030	0.036
3	0.0362	0.0409
4	0.0409	0.063
5	0.0674	0.111
6	0.111	0.183
7	0.183	0.302
8	0.302	0.498
9	0.498	0.821
10	0.821	1.35
11	1.35	2.23
12	2.23	3.68
13	3.68	6.06
14	6.06	10.0
15	10.0	19.6

^aMissing regions in this table correspond to energy ranges for which our sample was too thick to obtain data.

5.1 CHANNEL-INDEPENDENT UNCERTAINTIES

We first estimate the uncertainty on parameters which are independent of channel.

5.1.1 Sample Thickness Uncertainties

The uncertainty in the sample thickness can be derived as follows:

$$n = (N\rho x)/A \quad (5.1)$$

where

$$\begin{aligned} N &= \text{Avogadro's number} = 6.025 \times 10^{23}, \\ \rho &= \text{density in g/cm}^3, \\ x &= \text{sample thickness in cm, and} \\ A &= \text{atomic weight of element.} \end{aligned}$$

Rewriting in terms of quantities measured gives

$$n = \frac{N4mx}{A\pi D^2x} = C(m/D^2) \quad (5.2)$$

where m is the mass of the sample in grams, D is its measured diameter in cm, and $C = 4N/\pi A$.

A small increment in n is therefore given by

$$\delta n = (\partial n / \partial m) \delta m + (\partial n / \partial D) \delta D \quad , \quad (5.3)$$

which reduces to

$$\delta n = (n/m) \delta m - (2n/D) \delta D \quad , \quad (5.4)$$

when the derivatives are evaluated. Then the uncertainty in the thickness is given by the square root of the expectation value of δn^2 , where

$$\langle \delta n^2 \rangle = \langle \left\{ (n/m) \delta m - (2n/D) \delta D \right\} \times \left\{ (n/m) \delta m - (2n/D) \delta D \right\} \rangle \quad (5.5)$$

$$= (n/m)^2 \langle \delta m^2 \rangle + (2n/D)^2 \langle \delta D^2 \rangle - (4n^2/mD) \langle \delta m \delta D \rangle \quad . \quad (5.6)$$

Uncertainties in the mass and diameter are uncorrelated ($\langle \delta m \delta D \rangle = 0$) which gives

$$\langle \delta n^2 \rangle \equiv \Delta n^2 = (n/m)^2 \Delta m^2 + (2n/D)^2 \Delta D^2 \quad , \quad (5.7)$$

or

$$(\Delta n/n)^2 = (\Delta m/m)^2 + (2\Delta D/D)^2 \quad . \quad (5.8)$$

With $m = 1820 \pm 2$ g and $D = 10.155 \pm 0.005$ cm, we find

$$\Delta n/n = 0.15\% \quad . \quad (5.9)$$

There may also be an uncertainty due to non-uniform thickness of the sample if the flux is not uniform over the sample. This can be estimated from

$$\delta n' = (\partial n / \partial x) \delta x = (N \rho / A) \delta x = n (\delta x / x) \quad (5.10)$$

Thus the fractional contribution of the uncertainty in the thickness is

$$\Delta n' / n = \Delta x / x \quad (5.11)$$

which, with $x = 2.540 \pm 0.003$ cm, reduces to

$$\Delta n' / n = 0.1\% \quad (5.12)$$

Since these uncertainties are uncorrelated, we can combine them in quadrature to find the total uncertainty on n

$$\Delta n / n = \sqrt{(0.15)^2 + (0.1)^2} = 0.18\% \quad (5.13)$$

5.1.2 Uncertainty Due to Monitor Counter

We now turn to a discussion of the uncertainty to be associated with the house monitor counter, which is used to normalize the sample-in and sample-out spectra. The summed monitor counts for sample-in and sample-out are 1.9×10^9 and 1.4×10^9 respectively. This suggests that, barring systematic uncertainties, the total (Poisson statistics) uncertainties would be 0.0023% and 0.0027%. However, since we can identify several possible sources of systematic uncertainty for the monitor counter, we now analyze the experimental information available to us for this counter to see if it is consistent with the statistical uncertainty only.

The house monitor detector is a ^{235}U fission chamber containing 89 mg of ^{235}U . It is located in the wall of the concrete vault surrounding the neutron-producing target, at a distance of ~ 5 m from the target. The detector is gated on 47 μsec following the gamma flash, counts for 551 μsec and is then gated off. This time range corresponds to t-o-f neutron energies < 100 eV. About 11 counts per burst are obtained for both sample-in and -out. The house monitor counts are sent to a circuit to divide the counts by 10 (or 100) to prevent scaler overflow. For this measurement, the divide-by-100 option was used, so the monitor scaler readings were multiplied by 100 prior to use.

In an attempt to minimize effects of long term (> 1 hr) beam power variations during the run, the sample is cycled in and out of the beam. For sample-in, the measurement is run until a predetermined number of counts (valid stops) is registered in the NE110 detector at 200 m. The sample is then alternated out of the beam, and the measurement continued until a preset number of valid stops for the sample-out is obtained. This cycling continues for the duration of the run and is under computer control. Wall clock times are about 14 minutes for sample-in and 10 minutes for sample-out. For each cycle we store the number of triggers T , valid stops V , house-monitor counts H , and counts from a BF_3 counter B located adjacent to the sample changer. The BF_3 counter is not useful to normalize sample-in and -out, since it is sensitive to neutrons scattered from the sample, but it is useful as a check for consistency when the sample is either in or out.

One way to estimate the uncertainty associated with the house monitor is to study the distribution of values of the ratio V_i/H_i . This ratio corresponds to a ratio of counts in two detectors, viewing the "same" neutron source. The advantage of using this ratio to study the stability of the house monitor is that effects such as beam power variation cancel out, which is not true if the ratio T_i/H_i is used, for example. We then assume that the uncertainty obtained from the analysis of these ratios can be identified with the house monitor uncertainty, since V_i is a (deadtime corrected) constant. To describe our analysis of the house-monitor uncertainty we present here the analysis of data for one day's run; cycle data for other runs have been checked and found to be similar. For this case, the sample was cycled in and out of the beam 67 times. However, prior to evaluation of these ratios, we must correct the valid stops V_i for deadtime effects in the NE110 detector (the valid stop counter). Appendix C describes how this correction for each cycle was done. The deadtimes of the house monitor and BF_3 counter are negligible and are also discussed in Appendix C.

5.1.2.1 *Calculation of uncertainties for the ratio $(V_i/H_i)_i$.* We first calculated the ratios $(V_{in}/H_{in})_i$ and $(V_{out}/H_{out})_i$ for each of the 67 cycles, and determined the mean values of these ratios by averaging. We then obtained the difference of the individual ratios from the mean, and finally the corresponding standard deviation of the ratios about the mean. These results are given in columns 1 and 2 of Table 6, where we express the standard deviations as percent of the mean value. These are to be compared with the corresponding results expected simply from Poisson statistics, given in parenthesis, (i.e., $\sqrt{1/V + 1/H} \times 100$, where the mean values of V and H are used). Clearly, there are sources of uncertainty other than from the counting statistics.

Table 6. Uncertainties for sample-in and sample-out ratios, for sample-in/sample-out ratios (cycling), and the improvement obtained by cycling (gain). The numbers in parentheses are the uncertainties expected from Poisson statistics only.

Ratio	In (%)	Out (%)	Cycling (%)	Gain
V/H	0.45 (0.14)	0.74 (0.12)	0.59 (0.18)	1.5
V/B	1.67 (0.24)	1.31 (0.26)	0.67 (0.36)	3.2
V/T	3.18 (0.18)	3.75 (0.19)	1.99 (0.26)	2.5

5.1.2.2 *Calculation of uncertainties for the ratios V_i/B_i and V_i/T_i .* These ratios were calculated for sample-in and sample-out, and the standard deviations of the ratios about the mean were determined, as described above. These results are also presented in columns 1 and 2 of Table 6. The standard deviations for these ratios are larger than for the house monitor, implying that the BF_3 counter and number of triggers per cycle are not as stable as the house monitor. This is expected for the ratio of V/T , since power level variations will affect the number of triggers required to produce the selected number of valid stops.

5.1.2.3 *Inclusion of cycling.* The above analysis has failed to treat an important feature of our experimental procedure, namely, the effects of sequentially cycling the sample-in and -out of the beam. The cases we have treated above are consistent with measuring all the 14-minute sample-in runs, followed by all the 10-minute sample-out runs, and not interleaving them.

To approximate the effects of cycling, we calculate the ratios $(V_{in}/H_{in})_i/(V_{out}/H_{out})_i$ for each of the 67 cycles. We then calculate the mean value of these ratios by averaging, and obtain the standard deviation of these ratios about the mean value. We also did this for the ratios in Sect. 5.1.2.2, and the results, again expressed as percentage of the mean value, are given in the third column of Table 6. To see how much cycling reduces the uncertainties, we calculate the standard deviation of the ratios of columns 1 and 2, and compare with the results of column 3. This improvement factor is given in column 4 of Table 6, labeled "gain".

From Table 6 we find definite improvements are gained by cycling the sample-in and -out of the beam. Very rapid (pulse-to-pulse) variations in intensity were accounted for in the deadtime correction. Cycling reduces the uncertainty due to power drifts which occur over times longer than the cycle lengths, but we could still have effects due to systematic power variations with periods close to the cycling period. However, our experience has been that the machine is quite stable over times corresponding to the cycle periods.

For the run which we have been studying, the uncertainty in the ratios due just to the statistics is given in parenthesis. We find that the dispersion in the values is much greater than expected just from the statistics on the number of counts. In the case of the ratio of V/T , when cycling was not included, the dispersion can be viewed as a measure of the variation in intensity over the period of the run (1 day), and is $\sim 5\%$. If we look at this ratio in the case of cycling, the intensity variation drops to $\sim 2\%$ due to the shorter time periods involved. Looking at the ratios V/H and V/B , we find good agreement for the standard deviations when cycling is taken into account.

A number of reasons can be thought of for the larger dispersion in the ratios than expected from statistics. The house monitor is located in the wall of the target vault and views the complete neutron producing target. If the electron beam wanders vertically on the target, the neutron intensity at 200 m could be affected, with little or no change seen by the house monitor. Both the house monitor and BF_3 monitor are sensitive to different energy regions of the spectra than is the NE110 valid stop detector, hence if there is any change in spectral shape, the ratios will be affected. The house monitor is sensitive both to low-energy neutrons from the target and higher-energy neutrons which moderate down in the vault wall, while the BF_3 detector sees mainly scattered neutrons from the sample, filters, and nearby collimators.

Most of this monitor study was done after the work for this report was finished; the monitor was determined to be one of the largest sources of uncertainty and was inadequately treated on the first pass. Hence, since in that early work we treated the separate sample-in and sample-out monitor counts rather than the ratio, we now decide how to determine the uncertainties to use consistent with the equations used in that work. Because the gain due to cycling was 1.5, we can reduce the house monitor sample-in and -out uncertainty by 1.5, giving 0.30% for sample-in and 0.50% for sample-out. For this measurement we did not evaluate the ratios for enough of the other runs which make up the final data set to know what is the distribution of the mean values of the ratios. Thus, we choose to take the conservative route of assuming the mean values for other runs would agree no better than the standard deviation of the sample values about the mean for this run (i.e., 0.3% and 0.5%). This is consistent with observations from recent ORELA measurements (PE83). The alternative choice would be to use the standard deviation of the mean value as the uncertainty for the monitors, i.e., divide by $\sqrt{67}$, and assume that the mean values for the other runs would agree to within these uncertainties. This problem will be pursued more fully in analysis of future data. We thus assign an uncertainty of 0.3% for sample-in ($\Delta m/m$), and 0.5% for sample-out ($\Delta M/M$), with the understanding that these results could be as much as $\sqrt{67}$ smaller.

5.2 CHANNEL-DEPENDENT UNCERTAINTIES

We now turn to a description of the uncertainties which are channel-dependent; i.e., uncertainties in the energy scale and corrections for deadtime and for backgrounds. We first discuss uncertainties associated with the energy scale.

5.2.1 Energy-Scale Uncertainties

The non-relativistic energy for channel i can be expressed as

$$E_i = K^2(\varrho^2/t_i'^2) \quad (5.14)$$

where $K = 72.2977$ and

$$t_i' = t_i - t_o \quad , \quad (5.15)$$

where t_i' is the flight time measured relative to t_o . Conversion to relativistic energies is done using the equation $E' = E(1 + 1.5967 \times 10^{-9}E + 2.831906 \times 10^{-18}E^2)$ with E in eV.

An increment in E_i is given in terms of $\delta\varrho$ and $\delta t_i'$ as

$$\delta E_i = (\partial E_i/\partial \varrho)\delta\varrho + (\partial E_i/\partial t_i')\delta t_i' = (2E_i/\varrho)\delta\varrho - (2E_i/t_i')\delta t_i' \quad (5.16)$$

The covariance matrix element for the energies is then

$$\langle \delta E_i \delta E_j \rangle = \frac{4E_i E_j}{\varrho^2} \langle \delta \varrho^2 \rangle + 4E_i E_j \frac{\langle \delta t_i' \delta t_j' \rangle}{t_i' t_j'} \quad (5.17)$$

where $\langle \delta \varrho \delta t' \rangle$ is negligible for our measurement and is set equal to zero.

The diagonal elements of the covariance matrix yield the uncertainty in energy for point i :

$$\langle \delta E_i^2 \rangle = \frac{4E_i^2}{\varrho^2} \langle \delta \varrho^2 \rangle + 4E_i^2 \frac{\langle \delta t_i'^2 \rangle}{t_i'^2}$$

or

$$\left(\frac{\Delta E_i}{E_i}\right)^2 = 4\left(\frac{\Delta \ell}{\ell}\right)^2 + 4\left(\frac{\Delta t'_i}{t'_i}\right)^2 \quad (5.18)$$

which is a familiar result. The off-diagonal terms are given by

$$\frac{\langle \delta E_i \delta E_j \rangle}{E_i E_j} = 4\left(\frac{\Delta \ell}{\ell}\right)^2 + 4\frac{\langle \delta t'_i \delta t'_j \rangle}{t'_i t'_j} \quad (5.19)$$

The last term involves uncertainties in times for two different channels, i and j .

Two possible errors associated with the time measurements are (a) a simple offset (or additive) error and (b) a scale error. Consider first

$$t_i \rightarrow t_i + p \quad \text{and} \quad t_o \rightarrow t_o + p \quad (5.20)$$

Taking small increments yields

$$\delta t_i = \delta p \quad \text{and} \quad \delta t_o = \delta p \quad (5.21)$$

Thus

$$t'_i = t_i - t_o \rightarrow t_i + p - (t_o + p) = t'_i \quad (5.22)$$

and for the last term in Eq. (5.19)

$$\begin{aligned} \langle \delta t'_i \delta t'_j \rangle &= \langle \delta t_i \delta t_j \rangle + \langle \delta t_o^2 \rangle - \langle \delta t_i \delta t_o \rangle - \langle \delta t_o \delta t_j \rangle \\ &= \langle \delta p^2 \rangle + \langle \delta p^2 \rangle - \langle \delta p^2 \rangle - \langle \delta p^2 \rangle = 0 \end{aligned} \quad (5.23)$$

Thus, there is no effect for an additive error in both t_i and t_o , as expected.

Now consider effects due to possible scale errors in the time measurements

$$t_i \rightarrow t_i q \quad (5.24)$$

$$\delta t_i = t_i \delta q \quad (5.25)$$

and

$$t_o \rightarrow t_o q \quad (5.26)$$

$$\delta t_o = t_o \delta q \quad (5.27)$$

where $\langle q \rangle = 1$, and $\langle \delta q^2 \rangle = \Delta q^2$. Evaluating the last term in Eq. (5.19), we find

$$\langle \delta t'_i \delta t'_j \rangle = (t_i t_j + t_o^2 - t_i t_o - t_j t_o) \Delta q^2 = t'_i t'_j \Delta q^2 \quad (5.28)$$

A general combination of the time uncertainties would be a scale error in t and t_o in addition to an absolute error in t_o , i.e.,

$$t_i \rightarrow t_i q \quad \text{and} \quad t_o \rightarrow t_o q \quad (5.29)$$

Thus

$$\delta t_i = t_i \delta q \quad \text{and} \quad \delta t_o = t_o \delta q + q \delta t_o \quad (5.30)$$

With these assumptions, evaluation of the last term in Eq. (5.19) gives

$$\begin{aligned} \langle \delta t'_i \delta t'_j \rangle &= t_i t_j \langle \delta q^2 \rangle + t_o^2 \langle \delta q^2 \rangle + \langle \delta t_o^2 \rangle - t_i t_o \langle \delta q^2 \rangle - t_o t_j \langle \delta q^2 \rangle \\ &= (t_i - t_o)(t_j - t_o) \Delta q^2 + \Delta t_o^2 = t'_i t'_j \Delta q^2 + \Delta t_o^2 \end{aligned} \quad (5.31)$$

where we have used $\langle q \rangle = 1$. Thus for this experimentally useful case, we find for the diagonal elements of the covariance matrix

$$\left(\frac{\Delta E_i}{E_i}\right)^2 = \left(\frac{2\Delta\ell}{\ell}\right)^2 + (2\Delta q)^2 + \left(\frac{2\Delta t_o}{t'_i}\right)^2 \quad (5.32)$$

and for the off-diagonal elements

$$\frac{\langle \delta E_i \delta E_j \rangle}{E_i E_j} = \left(\frac{2\Delta\ell}{\ell}\right)^2 + (2\Delta q)^2 + \frac{(2\Delta t_o)^2}{t'_i t'_j} \quad (5.33)$$

The uncertainty in t_o , Δt_o , is estimated to be 1 ns for the present measurement. Δq is the uncertainty in the scale parameter defined in Eq. (5.24). This term is independent of channel and is expressed explicitly (as opposed to being implicitly included in the first term which is also channel independent) since experimental information may be available for such an uncertainty. For the present measurement we can identify Δq with uncertainties in the timing clock oscillator, which have been measured to be less than 1 part in 50,000, and this uncertainty is negligible for the present work.

As noted earlier, a separate report has been written which details the energy dependence of the flight path length, its uncertainty, t-o-f energies and uncertainties, and the resolution function and its uncertainty. The reader is encouraged to refer to that report (ORNL/TM-8880) (LA83) for details on these topics.

5.2.2 Deadtime Uncertainties

The general form for this correction for channel i is

$$D_i = \frac{1}{1 - \frac{(1 + \sigma^2)\alpha_i}{T}} \quad (5.34)$$

where

$$\alpha_i = \sum_{k=1}^4 \left[\sum_{i < j} c_i + c_j/2 \right]_k \quad (5.35)$$

and the sum includes all appropriate channels (see the discussion in Sect. 4.1). Hereafter, the subscript i will be omitted, for simplicity.

The uncertainty in D is given by

$$\delta D = \frac{\partial D}{\partial \sigma^2} \delta(\sigma^2) + \frac{\partial D}{\partial \alpha} \delta\alpha + \frac{\partial D}{\partial T} \delta T + \frac{\partial D}{\partial \Delta t} \delta(\Delta t) \quad . \quad (5.36)$$

The last term in this equation involves the uncertainty on the deadtime period when the system operates in a multistop-per-start mode. We find experimentally $\Delta t = 1104 \pm 10$ ns. However, since varying the deadtime period in the deadtime correction code shows negligible effects, $\delta(\Delta t)$ is set to zero. The term δT refers to the uncertainty in the number of bursts used for a run, and is assumed to have no uncertainty; that is, δT is set to zero. Since we have a nonextending deadtime, the term α , which is simply a sum of counts registered in channels corresponding to 1104 ns prior to the channel being corrected, has zero uncertainty, so $\delta\alpha$ is also set to zero. (In the case of the single stop-per-start mode, the sum runs over all channels up to the channel under correction, but the uncertainty on the sum is still zero.)

Thus we are left with just the first term in Eq. (5.36). Evaluating this term gives

$$\delta D = \frac{D(D - 1)}{1 + \sigma^2} \delta(\sigma^2) \quad . \quad (5.37)$$

Hence the uncertainty in the deadtime correction depends only on the uncertainty in the intensity variation of the neutron beam for levels of deadtime encountered in this measurement. Various measurements made for the standard deviation of the intensity variation (Sect. 4.1) suggest an uncertainty of $\pm 30\%$ for this parameter.

5.2.3 Background Uncertainties

We now turn to the uncertainties associated with background corrections. Recall that the background consists of three components: (1) a time-independent background, (2) an exponentially decaying background due to hydrogen capture in the water moderator surrounding the target and subsequent emission of a 2.2-MeV gamma ray, and (3) a background due to capture of slow neutrons by the boron in the Pyrex glass face of the photomultiplier tube. As discussed earlier, the background for each bias spectrum can be expressed as

$$B = \alpha + \beta e^{-t/\tau} + (at+f) + e + g/t^k \quad (5.38)$$

where

- α = the time-independent background,
- β = the $H(n,\gamma)$ time-dependent term, with half-life = 0.693τ
- $at+f$ = the $^{10}B(n,\alpha)$ term for $3 < t < 17 \mu\text{sec}$,
- e = this term from $17 < t < 26 \mu\text{sec}$, and
- g = this term for $t > 26 \mu\text{sec}$, with $k=1$ (2) for sample-out (in).

We now review the removal of these backgrounds from each bias spectrum in order to estimate uncertainties and correlations among the terms.

The time-independent term α is obtained at time $t > 1000 \mu\text{sec}$, where the remaining backgrounds are negligible. A small correction (<5%) is made to α to account for the observation of the 190 eV resonance in ^{238}U , which is treated as part of the $^{10}\text{B}(n,\alpha)$ background. A value for α is extracted for each bias level and subtracted for both the sample-in and sample-out spectra. The background due to the 2.2-MeV gamma ray from hydrogen capture is evaluated from a separate short measurement which has 20.3 cm of polyethylene in the beam to remove neutrons. The value of β is then extracted from bias 4, after removal of the time-independent background, and renormalized both to remove attenuation of the 2.2-MeV gamma ray through 20.3 cm of polyethylene and to include the attenuation through the nickel sample for sample-in. β is then normalized to the number of bursts for sample-in and sample-out and finally multiplied by the ratios 0.15:0.16:0.18:1.00 to get the appropriate value for biases 1, 2, and 3. This background is then calculated and subtracted channel by channel from each bias for sample-in and -out. Thus, since the value of β was not extracted from the nickel measurement and the value of β is not affected by the value chosen for α , α and β are uncorrelated. The value of τ is taken from experiment as $25.4 \mu\text{sec}$ (see Sect. 3.1), but clearly is correlated with β .

Finally, the last component of the background, due to the $^{10}\text{B}(n,\alpha\gamma)$ reaction, is evaluated and removed. The term d/t^k is fit to the remaining background in bias 3 of sample-in and -out after the useful neutrons have passed. Inspecting this background in bias 4, where it is smaller but can be observed at shorter times, we find it begins to flatten out for times $< 26 \mu\text{sec}$. We then use the value of g/t^k at $26 \mu\text{sec}$ to establish the constant value e . Thus, g and e are correlated. The background is assumed constant in time from 26 to $17 \mu\text{sec}$, where the flux shape at short times implies it should decrease with decreasing time. We chose a linear dependence for this background from 17 to $3 \mu\text{sec}$. For times $< 3 \mu\text{sec}$, we assume the background due to this process is zero. The terms a and f are obtained from the requirement that the background match onto e at $17 \mu\text{sec}$ and go to zero at $t = 3 \mu\text{sec}$. Thus, the values of a and f are correlated to the parameters e and g . The values of e , and particularly a and f , are poorly known, cannot be extracted from measurement, and can only be estimated. Once parameter values for bias 3 have been obtained, values for biases 1, 2, and 4 are obtained by multiplying the bias-3 parameters by 0.15, 0.32, and 0.60, respectively. As noted earlier in the report, during the data reduction the measured spectra for bias 3, $t > 31 \mu\text{sec}$ was utilized for this background removal, and not the analytic form g/t^k . For times $t < 31 \mu\text{sec}$, the analytic estimate had to be used. The analytic form for $t > 26 \mu\text{sec}$ is necessary for the uncertainty analysis and covariance matrix estimate to be described later in this report.

From this discussion, we find that the parameter β is not correlated to α , but since a , f , e , and g are evaluated after the backgrounds associated with α and β are removed, they are each correlated to α and β . Values for these correlations are not easily estimated, however. Our estimates are described in the following section.

5.3 CROSS-SECTION UNCERTAINTIES AND CORRELATIONS

Once the data are corrected for deadtime effects and backgrounds, they are ready to be converted to cross sections, and appropriate uncertainties must be given for each data point. We now use the information just developed to investigate these uncertainties.

The cross section σ can be written as

$$\sigma = -\frac{1}{n} \ln T \quad (5.39)$$

where n is the sample thickness in atoms/barn, and T is the transmission of neutrons through the sample, given by

$$T = \frac{M}{m} \left(\frac{cd-b}{CD-B} \right) \quad (5.40)$$

where m represents the monitor counts, c represents the measured counts, d is the deadtime correction, and b is the background. The lower-case symbols refer to sample-in, while upper case refers to sample-out. Thus

$$\sigma = -\frac{1}{n} \left[\ln \frac{M}{m} + \ln \left(\frac{cd-b}{CD-B} \right) \right] \quad (5.41)$$

The uncertainty on σ can be derived by considering the small increment in σ due to small increments in these parameters, i.e., from

$$\delta\sigma = \frac{\partial\sigma}{\partial n} \delta n + \frac{\partial\sigma}{\partial M} \delta M + \frac{\partial\sigma}{\partial m} \delta m + \frac{\partial\sigma}{\partial c} \delta c + \dots \quad (5.42)$$

Evaluating the derivatives yields for the increment in the cross section

$$\delta\sigma = - \left\{ \left[\frac{\sigma \delta n}{n} + \frac{\delta M}{nM} - \frac{\delta m}{nm} \right] - \left[\frac{\delta cd + \delta dc - \delta b}{n(cd-b)} \right] + \left[\frac{\delta CD + \delta DC - \delta B}{n(CD-B)} \right] \right\} \quad (5.43)$$

Labeling the three terms X , Y , and Z respectively gives

$$\delta\sigma = -(X - Y + Z) \quad (5.44)$$

The covariance between data points i and j is defined as the expectation value of the product of small increments in σ_i and σ_j .

$$\begin{aligned}
\text{cov}(\sigma_i \sigma_j) &= \langle \delta \sigma_i \delta \sigma_j \rangle \\
&= \langle (X_i - Y_i + Z_i)(X_j - Y_j + Z_j) \rangle \\
&= \langle X_i X_j \rangle - \langle X_i Y_j \rangle + \langle X_i Z_j \rangle - \langle Y_i X_j \rangle + \langle Y_i Y_j \rangle - \langle Y_i Z_j \rangle \\
&\quad + \langle Z_i X_j \rangle - \langle Z_i Y_j \rangle + \langle Z_i Z_j \rangle .
\end{aligned} \tag{5.45}$$

Since the determinations of values and uncertainties for n , m , and M were made independently of the determinations of values and uncertainties for background parameters, deadtime correction factors, and raw data counts, it is reasonable to assume that the term X is not correlated to terms Y and Z . Therefore, cross terms involving X may be dropped, leaving

$$\langle \delta \sigma_i \delta \sigma_j \rangle = \langle X_i X_j \rangle + \langle Y_i Y_j \rangle - \langle Y_i Z_j \rangle - \langle Z_i Y_j \rangle + \langle Z_i Z_j \rangle . \tag{5.46}$$

Each term in this expression may be explicitly evaluated; consider first the term $\langle X_i X_j \rangle$

$$\begin{aligned}
\langle X_i X_j \rangle &= \left(\sigma_i \frac{\delta n}{n} + \frac{\delta M}{nM} - \frac{\delta m}{nm} \right) \left(\sigma_j \frac{\delta n}{n} + \frac{\delta M}{nM} - \frac{\delta m}{nm} \right) \\
&= \sigma_i \sigma_j \frac{\langle \delta n^2 \rangle}{n^2} + \frac{\sigma_i \langle \delta n \delta M \rangle}{n^2 M} - \frac{\sigma_i \langle \delta n \delta m \rangle}{n^2 m} \\
&\quad + \sigma_j \frac{\langle \delta M \delta n \rangle}{n^2 M} + \frac{\langle \delta M^2 \rangle}{n^2 M^2} - \frac{\langle \delta M \delta m \rangle}{n^2 M m} \\
&\quad - \sigma_j \frac{\langle \delta m \delta n \rangle}{n^2 m} - \frac{\langle \delta m \delta M \rangle}{n^2 m M} + \frac{\langle \delta m^2 \rangle}{n^2 m^2}
\end{aligned} \tag{5.47}$$

Let us consider individual terms in the preceding expression: $\langle \delta n \delta M \rangle$ is the correlation between the sample thickness and monitor counts for sample-out. We assume this correlation is zero. Similarly, assume $\langle \delta n \delta m \rangle$, $\langle \delta M \delta n \rangle$, $\langle \delta M \delta m \rangle$, $\langle \delta m \delta M \rangle$, and $\langle \delta m \delta n \rangle = 0$. Thus we are left with

$$\langle X_i X_j \rangle = \frac{\sigma_i \sigma_j \Delta n^2}{n^2} + \frac{\Delta M^2}{n^2 M^2} + \frac{\Delta m^2}{n^2 m^2} \tag{5.49}$$

where Δn^2 , ΔM^2 , and Δm^2 are the variances of the uncertainties of the sample thickness, monitor-out and monitor-in counts, respectively. Values for these uncertainties have been given earlier in this section.

Likewise, the term $\langle Y_i Y_j \rangle$ can be expanded as

$$\begin{aligned} \langle Y_i Y_j \rangle &= \left[\frac{\delta c_i d_i + \delta d_i c_i - \delta b_i}{n(c_i d_i - b_i)} \right] \left[\frac{\delta c_j d_j + \delta d_j c_j - \delta b_j}{n(c_j d_j - b_j)} \right] \quad (5.50) \\ &= \left\{ d_i d_j \langle \delta c_i \delta c_j \rangle + d_i c_j \langle \delta c_i \delta d_j \rangle - d_i \langle \delta c_i \delta b_j \rangle \right. \\ &\quad + c_i d_j \langle \delta d_i \delta c_j \rangle + c_i c_j \langle \delta d_i \delta d_j \rangle + c_i \langle \delta d_i \delta b_j \rangle \\ &\quad \left. - d_j \langle \delta b_i \delta c_j \rangle - c_j \langle \delta b_i \delta d_j \rangle + \langle \delta b_i \delta b_j \rangle \right\} / D1 \quad , \quad (5.51) \end{aligned}$$

where the denominator $D1$ is $n^2(c_i d_i - b_i)(c_j d_j - b_j)$. The following terms are assumed to be uncorrelated, hence their expectation values are zero: $\langle \delta c_i \delta d_j \rangle$, $\langle \delta c_i \delta b_j \rangle$, $\langle \delta d_i \delta c_j \rangle$, and $\langle \delta b_i \delta c_j \rangle$. Thus, this term yields

$$\langle Y_i Y_j \rangle = \left\{ d_i^2 c_i \delta_{ij} + c_i c_j \langle \delta d_i \delta d_j \rangle - c_i \langle \delta d_i \delta b_j \rangle - c_j \langle \delta b_i \delta d_j \rangle + \langle \delta b_i \delta b_j \rangle \right\} / D1 \quad (5.52)$$

where we have used $\langle \delta c_i \delta c_j \rangle = c_i \delta_{ij}$ since raw counts obey a Poisson distribution.

For the next term, we find

$$\begin{aligned} \langle Y_i Z_j \rangle &= \left[\frac{\delta c_i d_i + \delta d_i c_i - \delta b_i}{n(c_i d_i - b_i)} \right] \left[\frac{\delta C_j D_j + \delta D_j C_j - \delta B_j}{n(C_j D_j - B_j)} \right] \quad (5.53) \\ &= \left[d_i D_j \langle \delta c_i \delta C_j \rangle + d_i C_j \langle \delta c_i \delta D_j \rangle - d_i \langle \delta c_i \delta B_j \rangle \right. \\ &\quad + c_i D_j \langle \delta d_i \delta C_j \rangle + c_i C_j \langle \delta d_i \delta D_j \rangle - c_i \langle \delta d_i \delta B_j \rangle \\ &\quad \left. - D_j \langle \delta b_i \delta C_j \rangle - C_j \langle \delta b_i \delta D_j \rangle + \langle \delta b_i \delta B_j \rangle \right] / D2 \quad , \quad (5.54) \end{aligned}$$

where the denominator $D2$ is given by $n^2(c_i d_i - b_i)(C_j D_j - B_j)$. We assume all of these terms involving correlations between sample-in and sample-out quantities are zero, except for two terms. The term involving $\langle \delta d_i \delta D_j \rangle$ is non-zero since the uncertainties for sample-in and -out deadtime corrections are related by the variation in intensity σ^2 . The last term is non-zero since the background due to hydrogen capture for sample-in is obtained by renormalizing the sample-out value. Thus

$$\langle Y_i Z_j \rangle = [c_i C_j \langle \delta d_i \delta D_j \rangle + \langle \delta b_i \delta B_j \rangle] / D2 \quad . \quad (5.55)$$

Similarly, the term $\langle Z_i Y_j \rangle$ is given by

$$\begin{aligned} \langle Z_i Y_j \rangle &= \left(\frac{\delta C_i D_i + \delta D_i C_i - \delta B_i}{n(C_i D_i - B_i)} \right) \left(\frac{\delta c_j d_j + \delta d_j c_j - \delta b_j}{n(c_j d_j - b_j)} \right) \quad (5.56) \\ &= \left[D_i d_j \langle \delta C_i \delta c_j \rangle + D_i c_j \langle \delta C_i \delta d_j \rangle - D_i \langle \delta C_i \delta b_j \rangle \right. \\ &\quad + C_i d_j \langle \delta D_i \delta c_j \rangle + C_i c_j \langle \delta D_i \delta d_j \rangle - C_i \langle \delta D_i \delta b_j \rangle \\ &\quad \left. - d_j \langle \delta B_i \delta c_j \rangle - c_j \langle \delta B_i \delta d_j \rangle + \langle \delta B_i \delta b_j \rangle \right] / D3 \quad , \quad (5.57) \end{aligned}$$

where the denominator $D3$ is $n^2(C_i D_i - B_i)(c_j d_j - b_j)$. Again, as for the last term, there are only two non-zero covariances, so this term reduces to

$$\langle Z_i Y_j \rangle = [C_i c_j \langle \delta D_i \delta d_j \rangle + \langle \delta B_i \delta b_j \rangle] / D3 \quad . \quad (5.58)$$

Finally, we note that the term $\langle Z_i Z_j \rangle$ is similar to the term $\langle Y_i Y_j \rangle$ except it involves the sample-out parameters. Thus, by analogy with Eq. (5.52), we can write

$$\begin{aligned} \langle Z_i Z_j \rangle &= \left[D_i^2 C_i \delta_{ij} + C_i C_j \langle \delta D_i \delta D_j \rangle - C_i \langle \delta D_i \delta B_j \rangle \right. \\ &\quad \left. - C_j \langle \delta B_i \delta D_j \rangle + \langle \delta B_i \delta B_j \rangle \right] / D4 \quad (5.59) \end{aligned}$$

where the denominator $D4$ is given by $n^2(C_i D_i - B_i)(C_j D_j - B_j)$.

Substituting these results in Eq. (5.46) and retaining only the non-zero correlations yields the final expression for the covariance matrix for the corrected data in terms of uncertainties in the corrections.

$$\begin{aligned}
\langle \delta\sigma_i \delta\sigma_j \rangle = & \sigma_i \sigma_j \frac{\Delta n^2}{n^2} + \frac{\Delta M^2}{n^2 M^2} + \frac{\Delta m^2}{n^2 m^2} + \frac{d_i^2 c_i \delta_{ij}}{D1} + \frac{\langle \delta b_i \delta b_j \rangle}{D1} \\
& + \frac{c_i c_j \langle \delta d_i \delta d_j \rangle}{D1} - \frac{c_i \langle \delta d_i \delta b_j \rangle}{D1} - \frac{c_j \langle \delta b_i \delta d_j \rangle}{D1} - \frac{c_i C_j \langle \delta d_i \delta D_j \rangle}{D2} \\
& - \frac{\langle \delta b_i \delta B_j \rangle}{D2} - \frac{C_i c_j \langle \delta D_i \delta d_j \rangle}{D3} - \frac{\langle \delta B_i \delta b_j \rangle}{D3} + \frac{D_i^2 C_i \delta_{ij}}{D4} \\
& + \frac{\langle \delta B_i \delta B_j \rangle}{D4} + C_i C_j \frac{\langle \delta D_i \delta D_j \rangle}{D4} - C_i \frac{\langle \delta D_i \delta B_j \rangle}{D4} - C_j \frac{\langle \delta B_i \delta D_j \rangle}{D4} \quad (5.60)
\end{aligned}$$

where the denominators are previously defined.

Each of these terms can be expanded in terms of the individual expressions for uncertainties in the deadtime and the background, and we now evaluate each term in Eq. (5.60).

Recall the expression for increments in the deadtime correction

$$\delta D = \frac{D(D-1)}{1 + \sigma^2} \delta(\sigma^2) \quad (5.61)$$

Therefore the covariances between the various deadtime corrections for channels i and j are given by

$$\begin{aligned}
\langle \delta D_i \delta D_j \rangle &= \frac{D_i(D_i-1)D_j(D_j-1)}{(1 + \sigma^2)^2} \langle \delta(\sigma^2) \delta(\sigma^2) \rangle \\
&= \frac{D_i D_j (D_i-1)(D_j-1)}{(1 + \sigma^2)^2} \Delta(\sigma^2)^2 \quad (5.62)
\end{aligned}$$

$$\langle \delta d_i \delta D_j \rangle = \frac{d_i D_j (d_i-1)(D_j-1)}{(1 + \sigma^2)^2} \Delta(\sigma^2)^2 \quad (5.63)$$

and

$$\langle \delta d_i \delta d_j \rangle = \frac{d_i d_j (d_i-1)(d_j-1)}{(1 + \sigma^2)^2} \Delta(\sigma^2)^2 \quad (5.64)$$

where $\Delta(\sigma^2)^2$ is the variance of σ^2 , which in turn is the variance (the square of the standard deviation) of the variation in intensity of the neutron beam. Thus, we have the necessary expressions for the deadtime terms in Eq. (5.60).

Similarly, from the expression for the background b

$$b = \alpha + \beta e^{-t/\tau} + (at + f) + e + g/t^k \quad , \quad (5.65)$$

a small increment in b is given by increments in each of the eight background parameters, via

$$\begin{aligned} \delta b = & \frac{\partial b}{\partial \alpha} \delta \alpha + \frac{\partial b}{\partial \beta} \delta \beta + \frac{\partial b}{\partial \tau} \delta \tau + \frac{\partial b}{\partial a} \delta a \\ & + \frac{\partial b}{\partial f} \delta f + \frac{\partial b}{\partial e} \delta e + \frac{\partial b}{\partial g} \delta g + \frac{\partial b}{\partial k} \delta k \end{aligned} \quad (5.66)$$

This reduces to

$$\begin{aligned} \delta b = & \delta \alpha + \delta \beta e^{-t/\tau} + \frac{\beta t}{\tau^2} \delta \tau e^{-t/\tau} \\ & + (\delta at + \delta f) + \delta e + (\delta g/t^k - \ln t \, g/t^k \, \delta k) \end{aligned} \quad (5.67)$$

(It is implicit that only one of the three quantities $(\delta at + \delta f)$, δe , $(\delta g/t^k - \ln t \, g/t^k \, \delta k)$ is present for a given channel. See Sect. 4.2.3 for details.)

We must now form the expectation values for the background and background-deadtime terms in Eq. (5.60). First, consider the background correlation between points i and j for sample-in. The expressions for sample-out, $\langle \delta B_i \delta B_j \rangle$, will have the same form.

$$\begin{aligned} \langle \delta b_i \delta b_j \rangle = & \left[\delta \alpha + \delta \beta e^{-t_i/\tau} + \frac{\beta t_i}{\tau^2} e^{-t_i/\tau} \delta \tau + (\delta at_i + \delta f) \right. \\ & \left. + \delta e + (\delta g/t_i^k - \ln t_i \, g/t_i^k \, \delta k) \right] \\ & \times \left[\delta \alpha + \delta \beta e^{-t_j/\tau} + \frac{\beta t_j}{\tau^2} e^{-t_j/\tau} \delta \tau + (\delta at_j + \delta f) \right. \\ & \left. + \delta e + (\delta g/t_j^k - \ln t_j \, g/t_j^k \, \delta k) \right] \end{aligned} \quad (5.68)$$

Multiplying out these terms and combining yields the result

$$\begin{aligned}
\langle \delta b_i \delta b_j \rangle &= \langle \delta \alpha^2 \rangle + \langle \delta \beta^2 \rangle e^{-(t_i+t_j)/\tau} + \langle \delta \tau^2 \rangle \frac{\beta^2 t_i t_j}{\tau^4} e^{-(t_i+t_j)/\tau} \\
&+ \langle \delta a^2 \rangle t_i t_j + \langle \delta f^2 \rangle + \langle \delta e^2 \rangle + \frac{\langle \delta g^2 \rangle}{t_i^k t_j^k} + \frac{g^2 \varrho n t_i \varrho n t_j}{t_i^k t_j^k} \langle \delta k^2 \rangle \\
&+ \langle \delta \alpha \delta \beta \rangle (e^{-t_i/\tau} + e^{-t_j/\tau}) + \langle \delta \alpha \delta \tau \rangle \frac{\beta}{\tau^2} (t_i e^{-t_i/\tau} + t_j e^{-t_j/\tau}) \\
&+ \langle \delta \alpha \delta a \rangle (t_i + t_j) + 2 \langle \delta \alpha \delta f \rangle + 2 \langle \delta \alpha \delta e \rangle + \langle \delta \alpha \delta g \rangle \left(\frac{1}{t_i^k} + \frac{1}{t_j^k} \right) \\
&- \langle \delta \alpha \delta k \rangle g \left[\frac{\varrho n t_i}{t_i^k} + \frac{\varrho n t_j}{t_j^k} \right] + \langle \delta \beta \delta \tau \rangle \frac{\beta}{\tau^2} e^{-(t_i+t_j)/\tau} (t_i + t_j) \\
&+ \langle \delta \beta \delta a \rangle (t_i e^{-t_i/\tau} + t_j e^{-t_j/\tau}) + \langle \delta \beta \delta f \rangle (e^{-t_i/\tau} + e^{-t_j/\tau}) \\
&+ \langle \delta \beta \delta e \rangle (e^{-t_i/\tau} + e^{-t_j/\tau}) + \langle \delta \beta \delta g \rangle \left(\frac{e^{-t_i/\tau}}{t_j^k} + \frac{e^{-t_j/\tau}}{t_i^k} \right) \\
&- \langle \delta \beta \delta k \rangle g \left[\frac{\varrho n t_i e^{-t_i/\tau}}{t_j^k} + \frac{\varrho n t_j e^{-t_j/\tau}}{t_i^k} \right] + \langle \delta \tau \delta a \rangle \frac{\beta}{\tau^2} t_i t_j (e^{-t_i/\tau} + e^{-t_j/\tau}) \\
&+ \langle \delta \tau \delta f \rangle \frac{\beta}{\tau^2} (t_i e^{-t_i/\tau} + t_j e^{-t_j/\tau}) + \langle \delta \tau \delta e \rangle \frac{\beta}{\tau^2} (t_i e^{-t_i/\tau} + t_j e^{-t_j/\tau}) \\
&+ \langle \delta \tau \delta g \rangle \frac{\beta}{\tau^2} \left(\frac{t_i e^{-t_i/\tau}}{t_j^k} + \frac{t_j e^{-t_j/\tau}}{t_i^k} \right) - \langle \delta \tau \delta k \rangle \frac{g \beta}{\tau^2} \left(\frac{\varrho n t_j t_i e^{-t_i/\tau}}{t_j^k} + \frac{\varrho n t_i t_j e^{-t_j/\tau}}{t_i^k} \right) \\
&+ \langle \delta a \delta f \rangle (t_i + t_j) + \langle \delta a \delta e \rangle (t_i + t_j) + \langle \delta a \delta g \rangle \left(\frac{t_i}{t_j^k} + \frac{t_j}{t_i^k} \right) \\
&- \langle \delta a \delta k \rangle g \left[\frac{\varrho n t_j t_i}{t_j^k} + \frac{\varrho n t_i t_j}{t_i^k} \right] + 2 \langle \delta f \delta e \rangle + \langle \delta f \delta g \rangle \left(\frac{1}{t_i^k} + \frac{1}{t_j^k} \right) \\
&- \langle \delta f \delta k \rangle g \left[\frac{\varrho n t_j}{t_j^k} + \frac{\varrho n t_i}{t_i^k} \right] + \langle \delta e \delta g \rangle \left(\frac{1}{t_i^k} + \frac{1}{t_j^k} \right) \\
&- \langle \delta e \delta k \rangle g k \left[\frac{\varrho n t_i}{t_i^k} + \frac{\varrho n t_j}{t_j^k} \right] - \langle \delta g \delta k \rangle g \left[\frac{\varrho n t_j}{t_i^k t_j^k} + \frac{\varrho n t_i}{t_i^k t_j^k} \right] .
\end{aligned} \tag{5.69}$$

Departing from our convention of small letters for sample-in and capital letters for sample-out, we denote sample-out background parameters by primes.

For sample-in and sample-out backgrounds, only the terms in $\delta\beta$ are correlated, hence (assuming $\tau = \tau'$).

$$\langle \delta b_i \delta B_j \rangle = \langle \delta \beta \delta \beta' \rangle e^{-(t_i + t_j)/\tau} \quad (5.70)$$

and

$$\langle \delta B_i \delta b_j \rangle = \langle \delta \beta' \delta \beta \rangle e^{-(t_i + t_j)/\tau} \quad (5.71)$$

Finally, evaluating covariance terms between deadtime and background corrections, we get

$$\begin{aligned} \langle \delta d_i \delta b_j \rangle &= \frac{d_i(d_i - 1)}{1 + \sigma^2} \left[\langle \delta(\sigma^2) \delta \alpha \rangle + e^{-t_j/\tau} \langle \delta(\sigma^2) \delta \beta \rangle + \frac{\beta t_j}{\tau^2} e^{-t_j/\tau} \langle \delta(\sigma^2) \delta \tau \rangle \right. \\ &\quad + t_j \langle \delta(\sigma^2) \delta a \rangle + \langle \delta(\sigma^2) \delta f \rangle + \langle \delta(\sigma^2) \delta e \rangle \\ &\quad \left. + \frac{1}{t_j^k} \langle \delta(\sigma^2) \delta g \rangle - \frac{g \rho n t_j}{t_j^k} \langle \delta(\sigma^2) \delta k \rangle \right] \quad (5.72) \end{aligned}$$

$$\begin{aligned} \langle \delta b_i \delta d_j \rangle &= \frac{d_j(d_j - 1)}{1 + \sigma^2} \left[\langle \delta \alpha \delta(\sigma^2) \rangle + e^{-t_i/\tau} \langle \delta \beta \delta(\sigma^2) \rangle + \frac{\beta t_i}{\tau^2} e^{-t_i/\tau} \langle \delta \tau \delta(\sigma^2) \rangle \right. \\ &\quad + t_i \langle \delta a \delta(\sigma^2) \rangle + \langle \delta f \delta(\sigma^2) \rangle + \langle \delta e \delta(\sigma^2) \rangle + \frac{1}{t_i^k} \langle \delta g \delta(\sigma^2) \rangle \\ &\quad \left. - \frac{g \rho n t_i}{t_i^k} \langle \delta k \delta(\sigma^2) \rangle \right] \quad (5.73) \end{aligned}$$

$$\begin{aligned}
\langle \delta D_i \delta B_j \rangle = & \frac{D_i(D_i-1)}{1+\sigma^2} \left[\langle \delta(\sigma^2) \delta \alpha' \rangle + e^{-t_j/\tau'} \langle \delta(\sigma^2) \delta \beta' \rangle + \frac{\beta' t_j}{\tau^2} e^{-t_j/\tau'} \langle \delta(\sigma^2) \delta \tau \rangle \right. \\
& + t_j \langle \delta(\sigma^2) \delta a' \rangle + \langle \delta(\sigma^2) \delta f' \rangle + \langle \delta(\sigma^2) \delta e' \rangle \\
& \left. + \frac{1}{t_j^{k'}} \langle \delta(\sigma^2) \delta g' \rangle - \frac{g' \rho n t_j}{t_j^{k'+1}} \langle \delta(\sigma^2) \delta k' \rangle \right] \quad (5.74)
\end{aligned}$$

$$\begin{aligned}
\langle \delta B_i \delta D_j \rangle = & \frac{D_j(D_j-1)}{1+\sigma^2} \left[\langle \delta \alpha' \delta(\sigma^2) \rangle + e^{-t_i/\tau'} \langle \delta \beta' \delta(\sigma^2) \rangle + \frac{\beta' t_i}{\tau^2} e^{-t_i/\tau'} \langle \delta \tau \delta(\sigma^2) \rangle \right. \\
& + t_i \langle \delta a' \delta(\sigma^2) \rangle + \langle \delta f' \delta(\sigma^2) \rangle + \langle \delta e' \delta(\sigma^2) \rangle \\
& \left. + \frac{1}{t_i^{k'}} \langle \delta g' \delta(\sigma^2) \rangle - \frac{g' \rho n t_i}{t_i^{k'+1}} \langle \delta k' \delta(\sigma^2) \rangle \right] \quad (5.75)
\end{aligned}$$

We now have explicit expressions for each term in Eq. (5.60) in terms of covariances of parameter uncertainties.

From Eq. (5.60) we know which terms of the covariance matrix we must evaluate, and in Eqs. (5.61) to (5.75) we carry out the algebra of expressing these covariances in terms of the measured parameters. To summarize this information, Table 7 presents a matrix of all parameters pertinent to the uncertainty analysis and indicates those parameters which have non-zero covariances. Since there are 30 parameters, we have $(30 \times 29)/2 = 435$ possible off-diagonal components of this symmetric matrix, plus the uncertainties on each of the 30 parameters, for a total of 465 terms to evaluate. In Table 7 the non-zero entries for which we have derived parameter relationships are labeled to distinguish whether they refer to sample-in or sample-out covariances, or whether they are independent of sample-in or -out.

We count 105 non-zero terms, or about 25% of the total number of possible entries. Note that we have chosen to list the α background contributions for each of the four bias spectra separately, rather than combine them as was done to form the final sample-in and sample-out spectra, since this is the way the data reduction process was done. Similarly, the β parameter was extracted from an independent measurement for bias 4 and renormalized for the present data. The ratios r_1 , r_2 , and r_3 are then used to normalize β_4 for biases 1, 2, and 3 (See Sect. 3.2). Parameters g and g' were obtained from the bias-3 data and normalized by the ratios s_1 , s_2 , and s_4 obtained from another separate measurement to obtain the values for biases 1, 2, and 4.

Considering the diagonal terms (variances) for the parameters, we have discussed uncertainties on n , m , M , and σ^2 previously in this section. Uncertainties on the α 's for sample-in and sample-out were determined directly from the fitting procedure which provided the values of these parameters. Likewise, the values and uncertainties for g and g' were given by the fitting procedures (See Sect. 4.2.3). All other uncertainties and covariances are yet to be determined, and we now turn to this problem.

We first evaluate the term $\Delta\beta'^2$ by considering the term $\langle\delta\beta\delta\beta'\rangle$ in Eq. (5.70). Recall from Sect. 5.2.3 that we can write the value of β for bias 4 sample-out in terms of the β measured in the auxiliary measurement as

$$\beta'_4 = \beta_a \left(\frac{T'}{u_p T_a} \right) \quad (5.76)$$

where the primes refer to sample-out, T is the number of bursts, and subscript a refers to the auxiliary measurement. u_p is the transmission of a 2.2-MeV gamma ray through 20.3 cm of polyethylene. For sample-in

$$\beta_4 = \beta_a \left(\frac{T u_{Ni}}{T_a u_p} \right) \quad (5.77)$$

where u_{Ni} represents the transmission of the 2.2-MeV gamma ray through 2.54 cm of nickel. To evaluate β in biases 1, 2, and 3, we multiply the bias-4 value by r_i , where $r_1 = 0.15$, $r_2 = 0.16$, and $r_3 = 0.18$. Thus

$$\beta'_i = \frac{\beta_a T'}{u_p T_a} r_i \quad (5.78)$$

and

$$\beta_i = \frac{\beta_a T u_{Ni}}{T_a u_p} r_i \quad (5.79)$$

For sample-out, taking small increments and recalling from Sect. 5.2.2 that $\delta T = \delta T' = \delta T_a = 0$, we find

$$\delta\beta'_i = \frac{\partial\beta'_i}{\partial\beta_a} \delta\beta_a + \frac{\partial\beta'_i}{\partial u_p} \delta u_p + \frac{\partial\beta'_i}{\partial r_i} \delta r_i$$

which gives

$$\delta\beta'_i = \beta'_i \left(\frac{\delta\beta_a}{\beta_a} \right) - \beta'_i \left(\frac{\delta u_p}{u_p} \right) + \beta'_i \left(\frac{\delta r_i}{r_i} \right) \quad (5.80)$$

and for sample-in

$$\delta\beta_i = \frac{\partial\beta_i}{\partial\beta_a} \delta\beta_a + \frac{\partial\beta_i}{\partial u_p} \delta u_p + \frac{\partial\beta_i}{\partial u_{Ni}} \delta u_{Ni} + \frac{\partial\beta_i}{\partial r_i} \delta r_i$$

which gives

$$\delta\beta_i = \beta_i \left(\frac{\delta\beta_a}{\beta_a} \right) - \beta_i \left(\frac{\delta u_p}{u_p} \right) + \beta_i \left(\frac{\delta u_{Ni}}{u_{Ni}} \right) + \beta_i \left(\frac{\delta r_i}{r_i} \right) \quad (5.81)$$

Since $(\delta\beta_a/\beta_a)$ is estimated to be 30%, and since ref. ST70, from which the gamma-ray interaction cross sections were taken, suggests a 3% uncertainty on $(\delta u_p/u_p)$ and $(\delta u_{Ni}/u_{Ni})$, we can drop these last two terms. This leaves

$$\delta\beta'_i = \beta'_i \left(\frac{\delta\beta_a}{\beta_a} \right) + \beta'_i \left(\frac{\delta r_i}{r_i} \right) \quad (5.82)$$

and for sample-in

$$\delta\beta_j = \beta_j \left(\frac{\delta\beta_a}{\beta_a} \right) + \beta_j \left(\frac{\delta r_j}{r_j} \right) \quad (5.83)$$

Thus, for two biases i and j , we obtain the desired results

$$\langle \delta\beta'_i \delta\beta_j \rangle = \beta'_i \beta_j (\Delta\beta_a/\beta_a)^2 + \beta'_i \beta_j \left(\frac{\langle \delta r_i \delta r_j \rangle}{r_i r_j} \right) \quad (5.84)$$

We also obtain the results for the covariances between sample-in terms as

$$\langle \delta\beta_i \delta\beta_j \rangle = \beta_i \beta_j (\Delta\beta_a / \beta_a)^2 + \beta_i \beta_j \left(\frac{\langle \delta r_i \delta r_j \rangle}{r_i r_j} \right) \quad (5.85)$$

and for $i = j$

$$(\Delta\beta_i)^2 = \beta_i^2 (\Delta\beta_a / \beta_a)^2 + \beta_i^2 (\Delta r_i / r_i)^2 \quad (5.86)$$

The results for sample-out terms are similar:

$$\langle \delta\beta'_i \delta\beta'_j \rangle = \beta'_i \beta'_j (\Delta\beta_a / \beta_a)^2 + \beta'_i \beta'_j \left(\frac{\langle \delta r_i \delta r_j \rangle}{r_i r_j} \right) \quad (5.87)$$

and for $i = j$

$$(\Delta\beta'_i)^2 = (\beta'_i)^2 (\Delta\beta_a / \beta_a)^2 + (\beta'_i)^2 (\Delta r_i / r_i)^2 \quad (5.88)$$

However, we note that β_i and β'_i are related by a constant number with a negligible uncertainty which we have ignored, i.e., via

$$\beta_i = \beta'_i u_{Ni} T/T' \quad (5.89)$$

Thus Eq. (5.84) becomes

$$\begin{aligned} \langle \delta\beta'_i \delta\beta_i \rangle &= \beta'_i \beta_i \left(\frac{\Delta\beta_a}{\beta_a} \right)^2 + \beta'_i \beta_i \left(\frac{\Delta r_i}{r_i} \right)^2 \\ &= (\beta'_i)^2 u_{Ni} T/T' \left(\frac{\Delta\beta_a}{\beta_a} \right)^2 + (\beta'_i)^2 u_{Ni} T/T' \left(\frac{\Delta r_i}{r_i} \right)^2 \end{aligned}$$

or

$$\langle \delta\beta'_i \delta\beta_i \rangle = u_{Ni} T/T' (\Delta\beta'_i)^2 \quad (5.90)$$

Similarly, Eq. (5.86) becomes

$$\begin{aligned}
(\Delta\beta_i)^2 &= (\beta'_i)^2(u_{Ni} T/T')^2 \left(\frac{\Delta\beta_a}{\beta_a} \right)^2 + (\beta'_i)^2(u_{Ni} T/T')^2 \left(\frac{\Delta\beta_a}{\beta_a} \right)^2 \\
&= (u_{Ni} T/T')^2 \Delta\beta_i'^2
\end{aligned} \tag{5.91}$$

Since the off-diagonal and diagonal covariance matrix elements can be written in terms of the sample-out uncertainty, Table 7 contains an entry only for $(\Delta\beta')^2$, the sample-out uncertainty.

We now consider the entries in Table 7 for r_1 , r_2 , and r_3 . Recall we define the ratios r_n for sample-out by

$$r_n = \frac{\beta'_n}{\beta_4} \tag{5.92}$$

Taking small increments we find

$$\delta r_n = \frac{\partial r_n}{\partial \beta'_n} \delta \beta'_n + \frac{\partial r_n}{\partial \beta'_4} \delta \beta'_4$$

or

$$\delta r_n = r_n \left(\frac{\delta \beta'_n}{\beta'_n} \right) - r_n \left(\frac{\delta \beta'_4}{\beta'_4} \right) \tag{5.93}$$

Forming the matrix element for two ratios m and n , we get

$$\begin{aligned}
\langle \delta r_n \delta r_m \rangle &= \frac{r_n r_m}{\beta'_n \beta'_m} \langle \delta \beta'_n \delta \beta'_m \rangle + \frac{r_n r_m}{\beta_4^2} \langle \delta \beta_4'^2 \rangle \\
\langle \delta r_n \delta r_m \rangle &= r_n r_m \left[\left(\frac{\Delta \beta'_n}{\beta'_n} \right)^2 \delta_{nm} + \left(\frac{\Delta \beta'_4}{\beta'_4} \right)^2 \right]
\end{aligned} \tag{5.94}$$

since $\langle \delta \beta'_n \delta \beta'_4 \rangle = \langle \delta \beta'_m \delta \beta'_4 \rangle = 0$.

From Eq. (5.76), we see that the (relative) uncertainty $(\Delta\beta'_4/\beta'_4)$ can be replaced by the uncertainty on $(\Delta\beta_a/\beta_a)$, which is the measured quantity. Thus

$$\langle \delta r_n \delta r_m \rangle = r_n r_m \left[\left(\frac{\Delta \beta'_n}{\beta'_n} \right)^2 \delta_{nm} + \left(\frac{\Delta \beta_a}{\beta_a} \right)^2 \right] \quad (5.95)$$

As noted earlier in this section, the uncertainty $\Delta \beta_a / \beta_a$ is estimated to be 25%, and the uncertainties $\Delta \beta'_n / \beta'_n$ are estimated to be 30%, 20%, and 20% for $n = 1, 2,$ and $3,$ respectively. With the ratios $r_1 = 0.15, r_2 = 0.16,$ and $r_3 = 0.18,$ we can evaluate the above matrix elements.

The value of τ was fixed at $25.4 \mu\text{sec},$ corresponding to a half-life of $0.693 \times 25.4 = 17.6 \mu\text{sec}.$ This value is based on calculations (KI72) and results of previous measurements. The uncertainty is estimated to be $1.0 \mu\text{sec}.$

We now develop expressions for uncertainties on parameters associated with the $^{10}\text{B}(n, \alpha \gamma)$ background. The ratios which give the distribution of the $^{10}\text{B}(n, \alpha \gamma)$ background among biases 1, 2, and 4 are also obtained from a separate measurement. Since the purity of the source is measured and the statistical uncertainty on the counts for each bias level is less than 0.1%, these ratios are assumed to be known to 5%, to allow some possible systematic uncertainty.

To evaluate the covariance matrix terms for the ratios $s_1, s_2,$ and $s_4,$ we recall

$$s_i = I_i / I_3 \quad (5.96)$$

where I_i is the integrated spectrum for bias i from the auxiliary measurement.

Taking small increments, we find

$$\delta s_i = \frac{\partial s_i}{\partial I_i} \delta I_i + \frac{\partial s_i}{\partial I_3} \delta I_3$$

or

$$\delta s_i = s_i \left(\frac{\delta I_i}{I_i} \right) - s_i \left(\frac{\delta I_3}{I_3} \right) \quad (5.97)$$

For the covariance between two biases i and j

$$\langle \delta s_i \delta s_j \rangle = s_i s_j \left[\left(\frac{\Delta I_i}{I_i} \right)^2 \delta_{ij} + \left(\frac{\Delta I_3}{I_3} \right)^2 \right] \quad (5.98)$$

where $\langle \delta I_i \delta I_3 \rangle = \langle \delta I_j \delta I_3 \rangle = 0.$

With $s_1 = 0.15$, $s_2 = 0.32$, $s_4 = 0.60$, $(\Delta I_i/I_i) = 5\%$, and $(\Delta I_3/I_3) = 5\%$, we can evaluate the diagonal and off-diagonal terms.

Uncertainties for parameters associated with the $^{10}\text{B}(n,\alpha\gamma)$ background are now developed. The fitting procedure assumed the parameter k was fixed; to estimate the uncertainty on k , we consider the uncertainty δb_4 on this term of the background at time $t_4 = 50 \mu\text{sec}$ (an arbitrary time, chosen for convenience).

$$\delta b_4 = \delta(g/t_4^k) = \frac{\delta g}{t_4^k} - \ln t_4 (g/t_4^k) \delta k \quad (5.99)$$

(We can write the background $b_4 = g/t_4^k$ equivalently as $b = g(\theta/t)^k$ where $\theta = 1 \mu\text{sec}$ so the argument of the logarithm is a dimensionless quantity. This is implicitly assumed for the remainder of this work.)

Thus, Eq. (5.99) yields an expression for δk

$$\delta k = \left(\frac{\delta g}{g} - \frac{\delta b_4}{b_4} \right) \frac{1}{\ln t_4} \quad (5.100)$$

for a small increment in k .

Thus forming the expectation value gives

$$\langle \delta k \delta k \rangle = \Delta k^2 = \frac{1}{(\ln t_4)^2} \left[\left(\frac{\Delta g}{g} \right)^2 + \left(\frac{\Delta b_4}{b_4} \right)^2 \right] \quad (5.101)$$

for the uncertainty on k , where we have assumed $\langle \delta g \delta b_4 \rangle = 0$. To obtain the covariance between g and k , multiply Eq. (5.100) by δg and take the expectation value

$$\langle \delta g \delta k \rangle = \frac{\Delta g^2}{g \ln t_4} \quad (5.102)$$

Both $\Delta g/g$ and $\Delta b_4/b_4$ are extractable from the data, so there is no ambiguity in Eqs. (5.101) and (5.102).

The value of e is fixed at $t_3 = 26 \mu\text{sec}$. It is convenient to define a term e_o via

$$e = \frac{g}{t_3^k} + e_o \quad (5.103)$$

where the value of e_o is zero but its uncertainty is non-zero. (e_o is independent of g and k .) A small increment in e is related to increments in g , k , and e_o via

$$\delta e = \frac{\partial e}{\partial g} \delta g + \frac{\partial e}{\partial k} \delta k + \frac{\partial e}{\partial e_o} \delta e_o = \frac{\delta g}{t_3^k} - \ln t_3 \frac{g}{t_3^k} \delta k + \delta e_o \quad (5.104)$$

Substituting Eq. (5.100) for δk and Eq. (5.103) for t_3^k (with $e_o = 0$) gives

$$\delta e = \frac{e \delta g}{g} \left[1 - \frac{\ln t_3}{\ln t_4} \right] + \delta e_o + \frac{e \ln t_3}{\ln t_4} \frac{\delta b_4}{b_4} \quad (5.105)$$

For simplicity, set $q = \ln t_3 / \ln t_4$ and form $\langle \delta e \delta e \rangle (= \Delta e^2)$

$$\left(\frac{\Delta e}{e} \right)^2 = (1 - q)^2 \left(\frac{\Delta g}{g} \right)^2 + \left(\frac{\Delta e_o}{e} \right)^2 + q^2 \left(\frac{\Delta b_4}{b_4} \right)^2 \quad (5.106)$$

where $\Delta g/g$ and $\Delta b_4/b_4$ are known and $\Delta e_o/e$ is estimated to be 0.25. Multiplying Eq. (5.105) by δg (or δk) and taking expectation values gives

$$\langle \delta e \delta g \rangle = e g (1 - q) \left(\frac{\Delta g}{g} \right)^2 \quad (5.107)$$

and

$$\langle \delta e \delta k \rangle = \frac{e}{\ln t_4} \left[(1 - q) \left(\frac{\Delta g}{g} \right)^2 - q \left(\frac{\Delta b_4}{b_4} \right)^2 \right] \quad (5.108)$$

In a similar manner, values for a and f are fixed by setting, at $t_1 = 3 \mu\text{sec}$

$$at_1 + f = a_0 t_1 + f_0 \quad (5.109)$$

and at $t_2 = 17 \mu\text{sec}$

$$at_2 + f = e + a_0 t_2 + f_0 \quad (5.110)$$

where $\langle a_0 \rangle$ and $\langle f_0 \rangle = 0$, but the corresponding uncertainties are non-zero. a_0 and f_0 are, moreover, assumed to be independent of each other and of all other parameters. Solving these equations for a and f give

$$a = \frac{e}{t_2 - t_1} + a_0 \quad (5.111)$$

and

$$f = f_0 - \frac{et_1}{t_2 - t_1} \quad (5.112)$$

Small increments in a and f yield

$$\delta a = \frac{\delta e}{t_2 - t_1} + \delta a_0 = a(\delta e/e) + \delta a_0 \quad (5.113)$$

$$\delta f = \delta f_0 - \delta e \left[\frac{t_1}{t_2 - t_1} \right] = \delta f_0 + f(\delta e/e) \quad (5.114)$$

Calculating the expectation values produces

$$\frac{\langle \delta a^2 \rangle}{a^2} = \left(\frac{\Delta a}{a} \right)^2 = \left(\frac{\Delta e}{e} \right)^2 + \left(\frac{\Delta a_0}{a} \right)^2 \quad (5.115)$$

and

$$\frac{\langle \delta f^2 \rangle}{f^2} = \left(\frac{\Delta f}{f} \right)^2 = \left(\frac{\Delta e}{e} \right)^2 + \left(\frac{\Delta f_o}{f} \right)^2 \quad (5.116)$$

since a , e , and f are assumed to be uncorrelated. Values for $\Delta a_o/a$ and $\Delta f_o/f$ may then be guesstimated; the value 0.4 is used for both. Since values of Δe have already been determined, Δa and Δf are now known.

To obtain the covariance of a (or f) with e , simply multiply Eq. (5.113) or Eq. (5.114) by δe and take expectation values.

$$\langle \delta a \delta e \rangle = (a/e) \Delta e^2 \quad (5.117)$$

and

$$\langle \delta f \delta e \rangle = (f/e) \Delta e^2 \quad (5.118)$$

The covariance between a and f is found from the product of Eqs. (5.113) and (5.114).

$$\langle \delta a \delta f \rangle = af(\Delta e/e)^2 \quad (5.119)$$

By combining Eqs. (5.113) and (5.114) with Eqs. (5.107) and (5.108), the remaining covariances can be evaluated in terms of the known uncertainty Δg and Δb_4 :

$$\langle \delta a \delta g \rangle = ag(1 - q) \left(\frac{\Delta g}{g} \right)^2 \quad (5.120)$$

$$\langle \delta a \delta k \rangle = \left(\frac{a}{\ell n t_4} \right) \left[(1 - q) \left(\frac{\Delta g}{g} \right)^2 - q \left(\frac{\Delta b_4}{b_4} \right)^2 \right] \quad (5.121)$$

$$\langle \delta f \delta g \rangle = fg(1 - q) \left(\frac{\Delta g}{g} \right)^2 \quad (5.122)$$

$$\langle \delta f \delta k \rangle = \left(\frac{f}{\ell t_4} \right) \left[(1 - q) \left(\frac{\Delta g}{g} \right)^2 - q \left(\frac{\Delta b_4}{b_4} \right)^2 \right] \quad (5.123)$$

Similarly, we need to determine the covariances of $\delta\sigma^2$ with the background parameters, since changing σ^2 in the deadtime correction clearly affects the values of the background parameters. At long times, where the background parameter α is extracted for each bias, the net counts $c'_i = c_i d - b_i$ are zero. Hence, since c , d , and b are all nearly independent of channel at long times,

$$b = \alpha = cd \quad (5.124)$$

and

$$\delta\alpha = c\delta d + d\delta c \quad (5.125)$$

but

$$\delta d = \left(\frac{d(d-1)}{1+\sigma^2} \right) \delta\sigma^2 \quad (5.126)$$

so

$$\delta\alpha = \frac{cd(d-1)}{1+\sigma^2} \delta\sigma^2 + d\delta c \quad (5.127)$$

Forming the covariance with $\delta\sigma^2$, and using $\alpha = cd$, gives

$$\langle \delta\alpha \delta\sigma^2 \rangle = \frac{\alpha(d-1)}{1+\sigma^2} \langle \delta\sigma^2 \delta\sigma^2 \rangle + d \langle \delta c \delta\sigma^2 \rangle \quad (5.128)$$

The last term is zero, so for each bias i we have

$$\langle \delta\alpha_i \delta\sigma^2 \rangle = \frac{\alpha_i(d-1)}{1+\sigma^2} (\Delta\sigma^2)^2 \quad (5.129)$$

An identical relation holds for sample-out, with $\alpha_i \rightarrow \alpha'_i$, $d \rightarrow D$.

Following removal of the background α , the remaining background at intermediate times (a few hundred μsec) is given by g/t^k and represents the $^{10}\text{B}(n,\alpha\gamma)$ background. Thus

$$c' = cd - b = 0 \text{ for } b = g/t^k \quad (5.130)$$

so that

$$g/t^k = cd \quad (5.131)$$

or

$$g = cd t^k \quad (5.132)$$

and

$$\begin{aligned} \delta g &= \frac{\partial g}{\partial c} \delta c + \frac{\partial g}{\partial d} \delta d + \frac{\partial g}{\partial k} \delta k + \frac{\partial g}{\partial t} \delta t \\ &= dt^k \delta c + ct^k \delta d + t^k \ln t \delta k + kt^{k-1} \delta t \end{aligned} \quad (5.133)$$

Forming the covariance with $\delta\sigma^2$

$$\langle \delta g \delta \sigma^2 \rangle = dt^k \langle \delta c \delta \sigma^2 \rangle + ct^k \langle \delta d \delta \sigma^2 \rangle + t^k \ln t \langle \delta k \delta \sigma^2 \rangle + kt^{k-1} \langle \delta t \delta \sigma^2 \rangle \quad (5.134)$$

Only the second term is non-zero, so

$$\langle \delta g \delta \sigma^2 \rangle = ct^k \frac{d(d-1)}{1+\sigma^2} \langle \delta \sigma^2 \delta \sigma^2 \rangle \quad (5.135)$$

where we have used $\delta d = \frac{d(d-1)}{1+\sigma^2} \delta \sigma^2$.

Since $ct^k = g/d$, if we use an average value of the deadtime correction, we finally obtain

$$\langle \delta g \delta \sigma^2 \rangle = \frac{g(\bar{d} - 1)}{1 + \sigma^2} (\Delta \sigma^2)^2 \quad (5.136)$$

Again, an identical relation holds for sample-out, with $g \rightarrow g'$, $\bar{d} \rightarrow \bar{D}$.

Now we can develop the covariance matrix elements between $\delta \sigma^2$ and δa , δf , and δe . In particular, from Eq. (5.104)

$$\delta e = \frac{\delta g}{t_3^k} - e \ln t_3 \delta k + \delta e_o \quad (5.137)$$

Thus, forming the covariance

$$\langle \delta e \delta \sigma^2 \rangle = \frac{1}{t_3^k} \langle \delta g \delta \sigma^2 \rangle - e \ln t_3 \langle \delta k \delta \sigma^2 \rangle + \langle \delta e_o \delta \sigma^2 \rangle \quad (5.138)$$

Since k was fixed, we assume $\langle \delta k \delta \sigma^2 \rangle = 0$, and we assume the last term is also zero. Thus

$$\langle \delta e \delta \sigma^2 \rangle = \frac{e(\bar{d} - 1)}{1 + \sigma^2} (\Delta \sigma^2)^2 \quad (5.139)$$

Similarly, from Eq. (5.113)

$$\delta a = a \delta e/e + \delta a_o \quad (5.140)$$

Thus

$$\langle \delta a \delta \sigma^2 \rangle = a/e \langle \delta e \delta \sigma^2 \rangle + \langle \delta a_o \delta \sigma^2 \rangle \quad (5.141)$$

We assume $\langle \delta a_o \delta \sigma^2 \rangle = 0$, so

$$\langle \delta a \delta \sigma^2 \rangle = \frac{a(\bar{d} - 1)}{1 + \sigma^2} (\Delta \sigma^2)^2 \quad (5.142)$$

Finally, from Eq. (5.114)

$$\delta f = \frac{f \delta e}{e} + \delta f_o \quad (5.143)$$

Thus

$$\langle \delta f \delta \sigma^2 \rangle = f/e \langle \delta e \delta \sigma^2 \rangle + \langle \delta f_o \delta \sigma^2 \rangle \quad (5.144)$$

Again assuming the last term is zero gives

$$\langle \delta f \delta \sigma^2 \rangle = \frac{f(\bar{d} - 1)}{1 + \sigma^2} (\Delta \sigma^2)^2 \quad (5.145)$$

As before, sample-out matrix elements have the identical forms of the above equations, with substitution of the appropriate sample-out parameters.

We now have explicit algebraic relationships for all of the diagonal and many of the off-diagonal entries in Table 7, in terms of the measurement parameters and their uncertainties. In Table 8 we summarize the values of these parameters and their variances. Thus, at this point we are able to calculate numerical values for many of the entries in Table 7.

It remains to determine the off-diagonal covariances between α , β , τ , and the other parameters. In this case, no obvious analytic relationships are available so we must resort to rather crude estimates. Recall that the covariance between two parameters P_1 and P_2 can always be written in terms of a correlation $c_{1,2}$ via

$$\langle \delta P_1 \delta P_2 \rangle = \sqrt{\Delta P_1^2 \Delta P_2^2} c_{1,2} \quad (5.146)$$

where $|c_{1,2}| \leq 1$, and ΔP_1 and ΔP_2 are the uncertainties (i.e., the square root of the variances) of these parameters. These variances are available for all the parameters from Table 8, and the sign for $c_{1,2}$ can generally be determined by physical intuition. We can estimate the magnitude of $|c_{1,2}|$ and use Eq. (5.146) to obtain our "best guess" for the remaining covariances in Table 7.

We now describe our methods for estimating the magnitude and signs of $c_{1,2}$ for the remaining covariances. Since parameters for the $^{10}\text{B}(n, \alpha \gamma)$ background are extracted from bias-3 data following removal of α_3 and β' , a non-zero correlation is expected between α_3 and g , k , e , a , and f . It is plausible that if we increase α_3 , there would be less $^{10}\text{B}(n, \alpha)$ background to remove, so the sign of $c_{1,2}$ is taken as negative. We arbitrarily choose $|c_{1,2}| = 0.5$ for $\langle \delta \alpha_3 \delta g \rangle$. Thus

Table 8. Summary of the values and variances of the data correction parameters used in this work. Some parameters were assigned absolute uncertainties while others were relative.

Parameter number	Symbol	Value	Absolute uncertainty	Percent uncertainty
1	n	0.2304	0.00041	
2	m	19,137,531		0.3
3	M	13,610,924		0.5
4	σ^2	0.02		30.0
5	α_1	1.26		4.0
6	α_2	1.87		4.0
7	α_3	2.31		4.0
8	α_4	1.64		4.0
9	α'_1	0.91		4.0
10	α'_2	1.33		4.0
11	α'_3	1.64		4.0
12	α'_4	1.16		4.0
13	β'	1.18		25.0
14	ψ	25.4	1.0	
15	r_1	0.15		38.9
16	r_2	0.16		32.0
17	r_3	0.18		32.0
18	g	1,440		20.0
19	k	2.0	0.0723	
20	e	2.13		30.0
21	a	0.152		50.0
22	f	-0.456		50.0
23	g'	69.0		20.0
24	k'	1.0	0.0723	
25	e'	2.66		30.0
26	a'	0.190		50.0
27	f'	-0.570		50.0
28	s_1	0.15		7.1
29	s_2	0.32		7.1
30	s_4	0.60		7.1

$$\langle \delta\alpha_3 \delta g \rangle = -0.5 \Delta\alpha_3 \Delta g \quad (5.147)$$

Equations (5.100), (5.105), (5.113), and (5.114) give us expressions for δk , δe , δa , and δf which can be expressed in terms of δg , so the covariance terms $\langle \delta\alpha_3 \delta k \rangle$, $\langle \delta\alpha_3 \delta e \rangle$, $\langle \delta\alpha_3 \delta a \rangle$ and $\langle \delta\alpha_3 \delta f \rangle$ can be written in terms of $\langle \delta\alpha_3 \delta g \rangle$. We will not go through the algebra here, but the final results will be displayed later. The same expressions are valid for the sample-out covariances by substituting the sample-out parameters.

We note that the covariance between $\delta\sigma^2$ and $\delta\beta'$ is zero since β' is evaluated from a separate measurement, so changing σ^2 in the present measurement would not change the value of β' . Similarly, $\delta\sigma^2$ and $\delta\tau$ are uncorrelated.

To obtain a relation between $\delta\beta'$ and $\delta\tau$, we can set a small increment in this background component to zero to see how the terms compensate.

$$b = \beta' e^{-t/\tau}$$

$$\delta b = \frac{\partial b}{\partial \beta'} \delta\beta' + \frac{\partial b}{\partial \tau} \delta\tau = 0 \quad (5.148)$$

This yields

$$\delta\beta' = -\beta' t \left(\frac{\delta\tau}{\tau^2} \right) \quad (5.149)$$

Thus, multiplying by $\delta\tau$ and taking the expectation value gives

$$\begin{aligned} \langle \delta\beta' \delta\tau \rangle &= -\beta' t \left(\frac{\langle \delta\tau^2 \rangle}{\tau^2} \right) \\ &= -\beta' t \left(\frac{\Delta\tau}{\tau} \right)^2 \\ &= - \left(\frac{\beta'}{\Delta\beta'} \right) \left(\frac{\Delta\tau}{\tau} \right) \left(\frac{t}{\tau} \right) \Delta\beta' \Delta\tau \end{aligned} \quad (5.150)$$

Evaluating arbitrarily at $t = \tau$, we find

$$\langle \delta\beta' \delta\tau \rangle = - \left(\frac{\beta'}{\Delta\beta'} \right) \left(\frac{\Delta\tau}{\tau} \right) \Delta\beta' \Delta\tau \quad (5.151)$$

This can now be evaluated using values from Table 8.

Since the $^{10}\text{B}(n,\alpha\gamma)$ background is removed following the $\text{H}(n,\gamma)$ background described by $\beta'e^{-t/\tau}$, correlations exist among the parameters β' and τ and the parameters describing the ^{10}B background. Since increasing β' would leave less ^{10}B background, the sign of the correlation is negative. We arbitrarily choose a correlation coefficient of -0.5 for $\langle \delta\beta' \delta g \rangle$. Thus,

$$\langle \delta\beta' \delta g \rangle = -0.5 \Delta\beta' \Delta g \quad (5.152)$$

and as we noted previously, we have expressions for δk , δe , δa and δf in terms of δg , so the assumption of -0.5 can be propagated for the other covariances between $\delta\beta'$ and the ^{10}B parameters. Also, the sample-out covariances are obtained by replacing $\delta g \rightarrow \delta g'$, etc.

Finally, we need to evaluate the covariance terms between $\delta\tau$ and the parameter uncertainties in the ^{10}B background. From Eq. (5.149) we found

$$\delta\beta' = -\beta'(t/\tau)(\delta\tau/\tau)$$

We choose to evaluate this at $t = \tau$ for convenience, so

$$\delta\beta' = -\beta'(\delta\tau/\tau) \quad (5.153)$$

Thus, we can easily evaluate the required terms, i.e., substituting for $\delta\beta'$,

$$\begin{aligned} \langle \delta\beta' \delta g \rangle &= -0.5 \Delta\beta' \Delta g && \text{becomes} \\ \langle \delta\tau \delta g \rangle &= +0.5(\tau/\beta') \Delta\beta' \Delta g && \text{or} \\ \langle \delta\tau \delta g \rangle &= +(\tau/\beta') \langle \delta\beta' \delta g \rangle \end{aligned} \quad (5.154)$$

So we find that the covariance terms involving $\delta\tau$ can be obtained from the covariance terms $\delta\beta'$ by multiplying the latter terms by τ/β' . The sample-out results for g' etc., easily follow as noted earlier. This completes the derivation of all non-zero terms in Table 7.

5.4. THE UNCERTAINTY PROPAGATION CODE ALEX

The estimates of parameter uncertainties and correlations described in earlier sections were used as input to the computer program ALEX, which is a generalized data uncertainty propagation program designed to provide variances and covariances for experimental data, including the capability to combine the results into a covariance matrix of manageable size. The code ALEX is described in detail in another report (LA83a).

Input to ALEX (*Analysis of Experimental Data*, with honors going to Alex Zucker who authorized its development) consists of the following pieces of information:

1. Raw data (counts) for sample-in and sample-out.
2. Dead-time correction factors for sample-in and sample-out.
3. Channel structure for storage of (1) and (2).
4. Analytic expressions for the five functions f in the expression

$$X = f_1 \left(\frac{f_2 c + f_3}{f_4 C + f_5} \right)$$

where X is either the cross section or the transmission.

5. Derivatives of each of these five functions with respect to the parameters in the functions.
6. Values and covariances for all parameters appearing in any of the five functions (non-zero entries in Table 7 and parameter values and uncertainties from Table 8).
7. Group structure (energy boundaries) for output of binned cross sections (Table 5).

Output produced by ALEX includes

1. A computer data file containing the coefficients of the various components of the uncertainty on each data point. The size of this file is (number of data points) \times (number of parameters + 2). This file is produced by using Inputs (1) through (5) above. Combining this file with (6) above would yield the full data covariance matrix, whose size is the square of the number of data channels; i.e., unmanageably large for a typical ORELA measurement (3.6 billion numbers for the present case).
2. The average cross section and associated covariance matrix for the energy groups specified in (7) above. The results are found by summing over the appropriate channels.

The resulting correlation matrix for the nickel measurement will be presented in the following section of this report.

6. DISCUSSION OF RESULTS

6.1 NICKEL CROSS-SECTION RESULTS

The ENDF/B-V evaluation for natural nickel was done by Divadeenam (DI79). The total cross section from 1.0×10^{-5} eV to 650 keV is given in terms of resonance parameters and a smooth background file. This portion of the evaluation is taken over from evaluation work of Stieglitz et al. (ST73) which formed part of the ENDF/B-II file for nickel. Resonance parameters from that work were based on an R-matrix analysis of data from Stieglitz et al. (ST71), Farrell et al. (FA66), and Garg et al. (GA71). Details of the analysis are given in ref. ST73 and are summarized here. In that work, the above data sets were surveyed and a preliminary set of resonance parameters were picked from reports accompanying the data or from BNL-325, Second Edition. This set of resonance parameters was then used in an R-matrix code to generate the total cross-section. Parameters were then modified and resonances added to provide a better visual fit to the experimental data. The set of parameters which ultimately provided the best visual fit to the above data sets was then adopted for the evaluation up to 650 keV and still form the evaluation up to 650 keV for ENDF/B-V. We note here that a new resonance parameter evaluation (PE82) has been completed for ^{60}Ni and is underway for ^{58}Ni . This analysis, utilizing a newly developed R-matrix code (LA80a) which uses Bayes' theorem for parameter searching, has been applied to available isotopic data (HA77) from ORELA measured at the 80-m flight path.

Comparisons of our averaged cross sections with the ENDF/B-V evaluation are shown in Figs. 10 through 22. Point cross sections were constructed from the resonance parameters given in the evaluation and combined with the background cross section in file 3 to form the results shown here.

Our sample was too thick to allow extraction of peak cross sections for $l = 0$ resonances near 4.5 keV in ^{62}Ni , 12.5 keV in ^{60}Ni , 15.5 keV in ^{58}Ni , 28.6 keV in ^{60}Ni , 63 keV in ^{58}Ni , and 65.4 keV in ^{60}Ni . Below ~ 20 keV, the resonances noted above removed nearly all the neutrons except for a window near 7 keV where some useful data were obtained, although the background contributed about 20% of the raw counts. Up to 95 keV, the resonance energies of the evaluation are generally in good agreement with our results. However, a number of resonances not contained in the evaluation are observed; most of the larger ones are $l > 0$ resonances in ^{58}Ni . Above 95 keV, most of the resonances in the evaluation are at a lower energy than we observe in our measurement. This energy shift results in a particularly poor representation of cross-section minima around 135 keV and 205 keV. An accurate energy scale is especially important for cross-section minima in shielding calculations when a combination of materials is used, such as nickel in stainless steel. We observe many more resonances up to 650 keV than exist in the present evaluation, and some of the existing ones in the evaluation apparently have the wrong spin.

From 650 to 700 keV, the evaluation is probably based on the data of Schwartz et al. (SC74), although it is not clear since the evaluation documentation (ST73, DI79) differ on the description of this energy region. From 700 keV to 20 MeV the evaluation is based on a 50-m transmission measurement by Perey, Love, and Kinney (PE73). In their measurement, neutron transmission was measured through thin (2.54 cm) and thick (10.2 cm) nickel samples with a nominal resolution of 0.12 ns/m. During the evaluation process, a spline fit was done, using the thin sample data for the peaks and the thick sample data for the minima. The present data were taken with the same 2.54-cm-thick sample and a nominal resolution of 0.04 ns/m. The higher resolution of the present data is apparent in Figs. 17 through 22, which compare the ENDF/B-V evaluation with our present data.

In Fig. 23 we have plotted the percent difference between the nickel data described in this report and the present evaluation for ENDF/B-V. This figure demonstrates that above ~ 500 keV our data

ORNL-DWG 82-18032

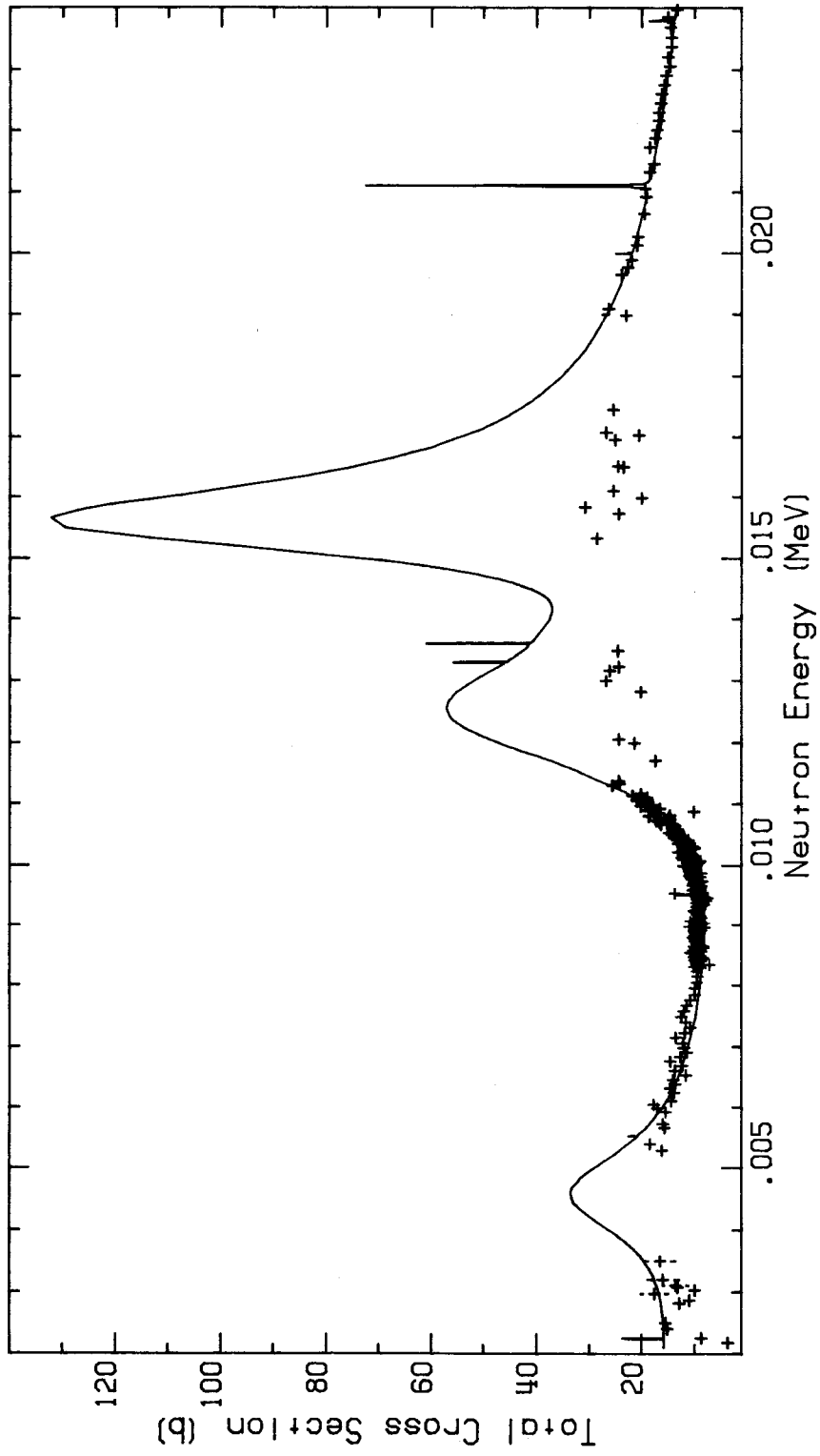


Fig. 10. Comparison of our averaged data (+) with the ENDF/B-V evaluation (-) from 2 to 24 keV.

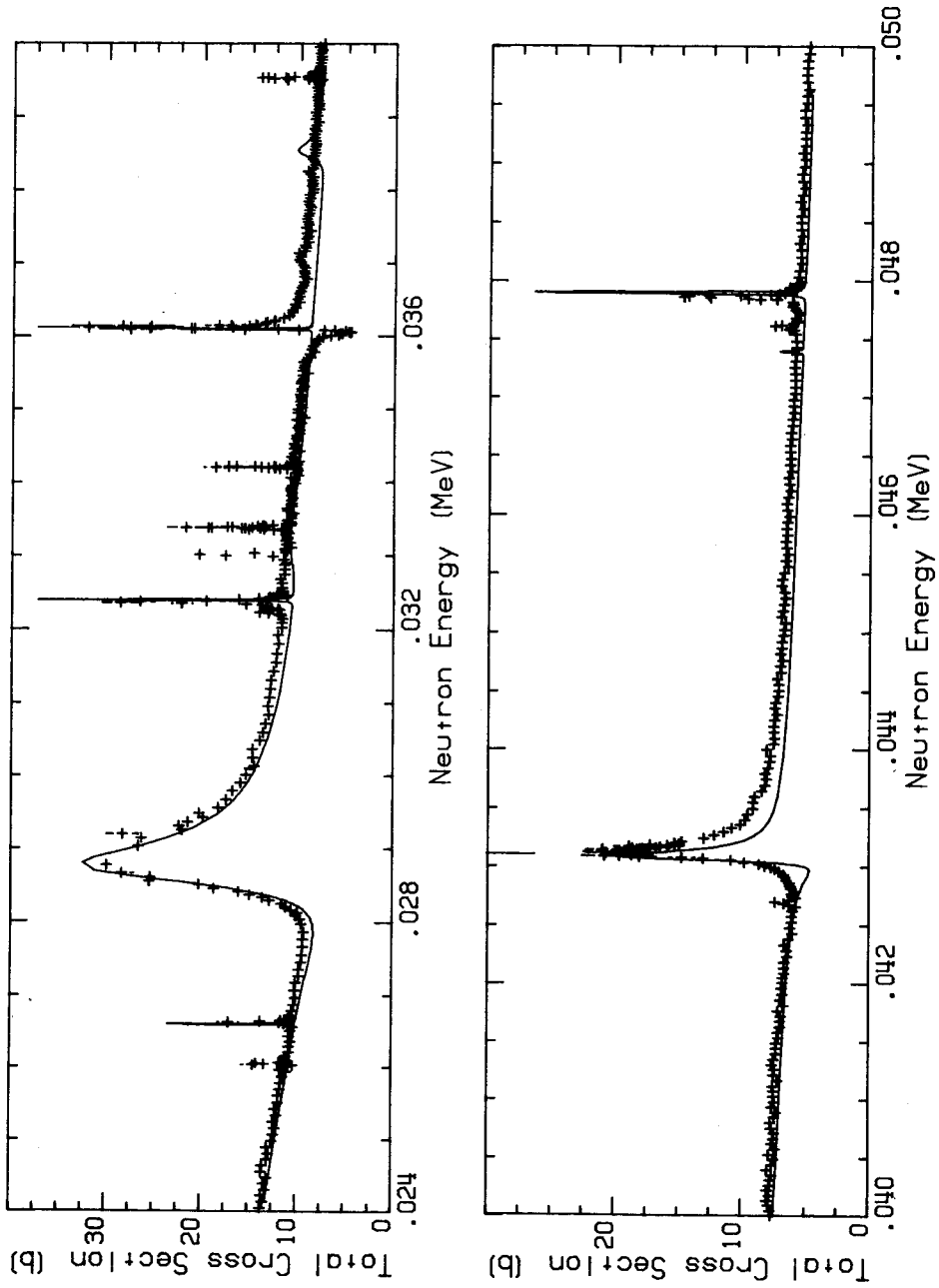


Fig. 11. Comparison of our averaged data with the ENDF/B-V evaluation from 24 to 50 keV.

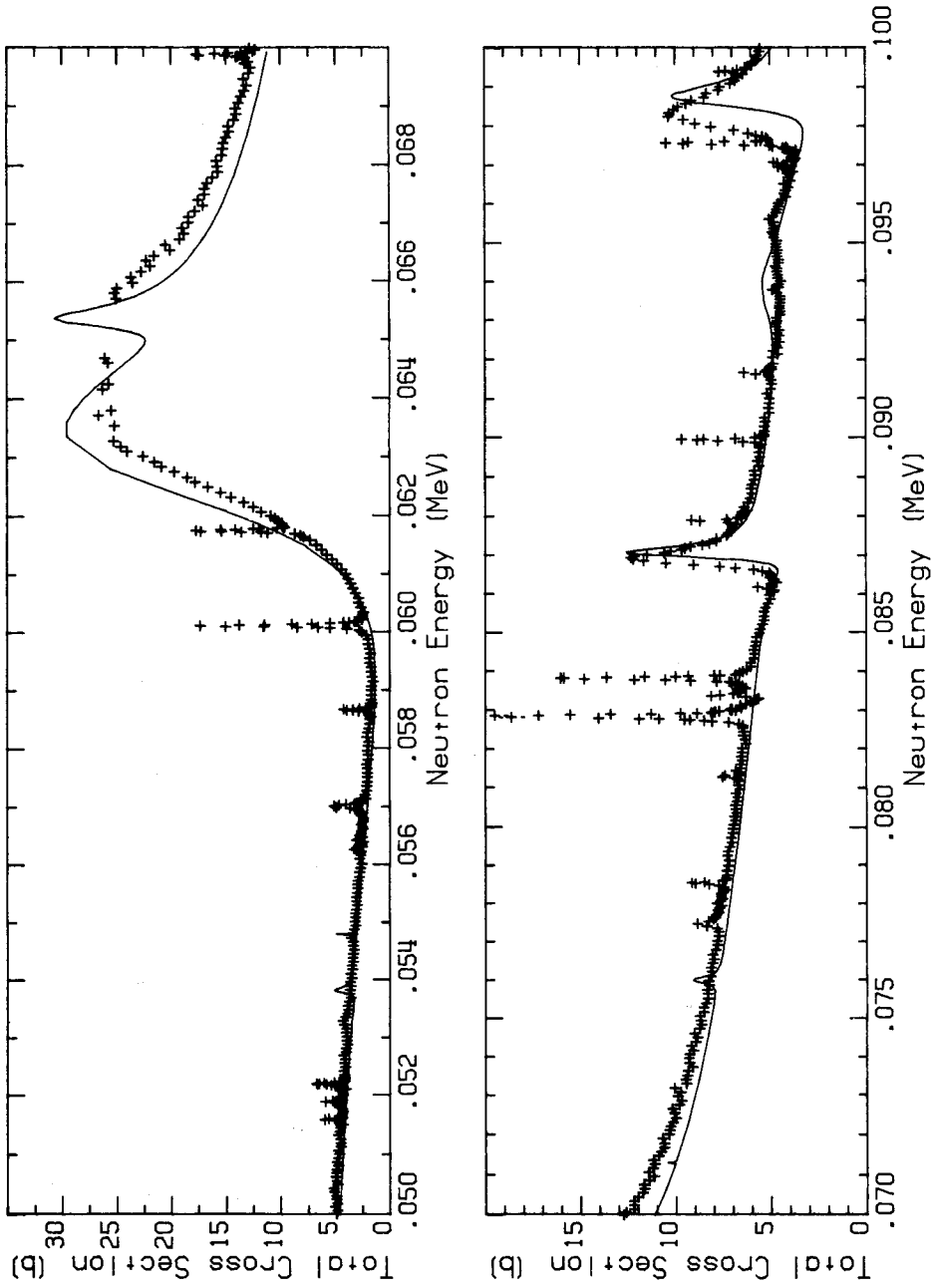


Fig. 12. Comparison of our averaged data with the ENDF/B-V evaluation from 50 to 100 keV.

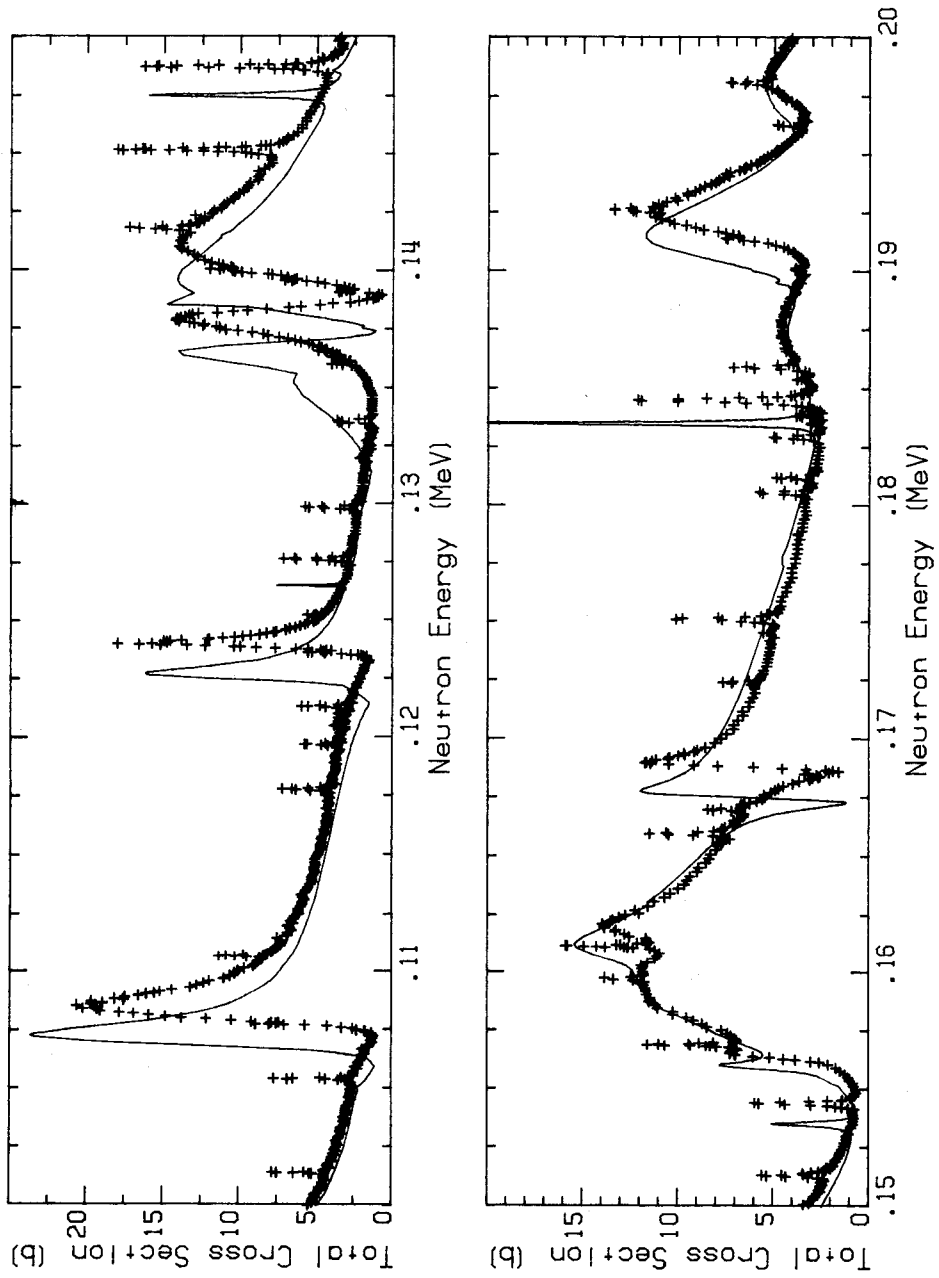


Fig. 13. Comparison of our averaged data with the ENDF/B-V evaluation from 100 to 200 keV.

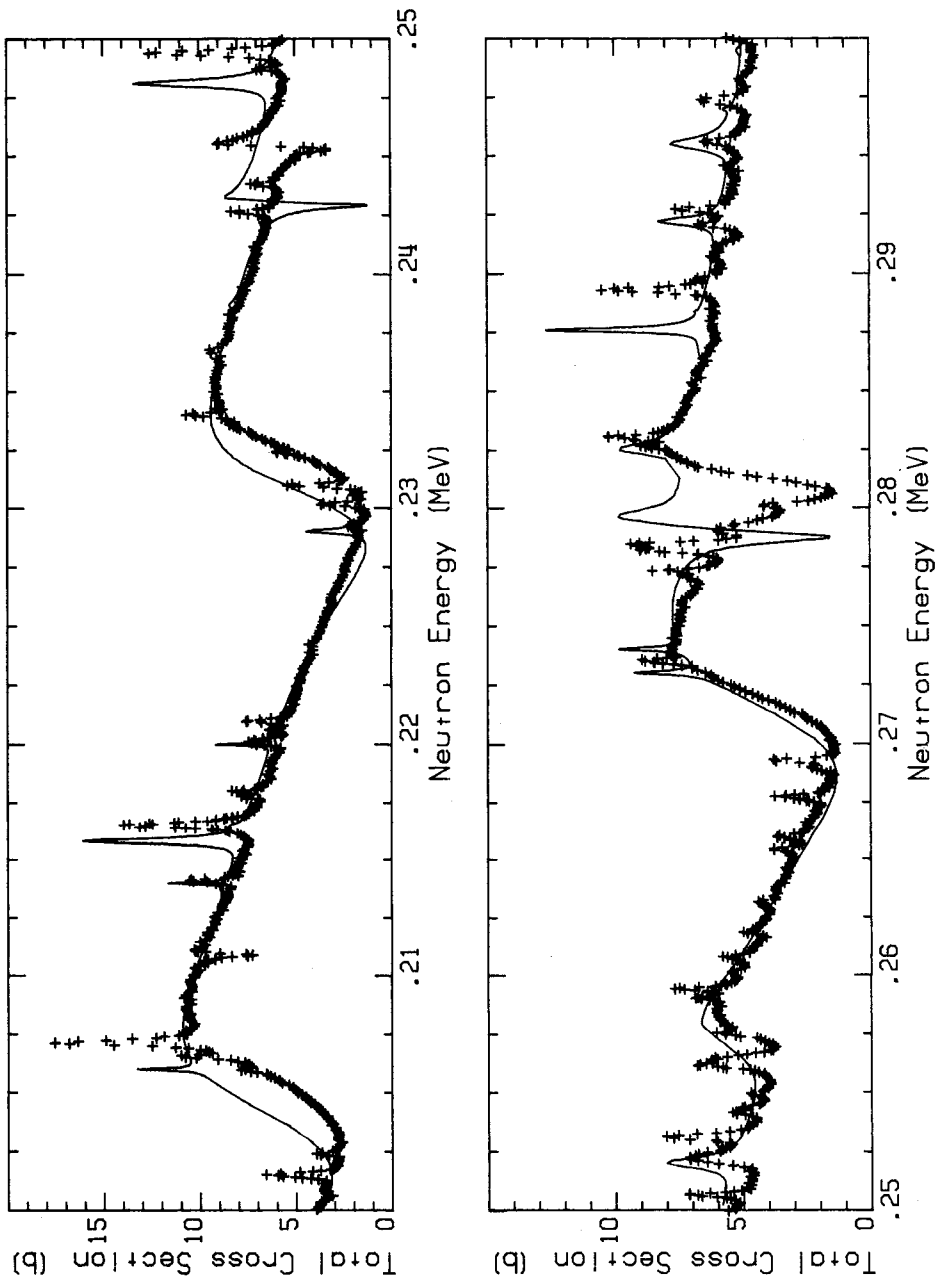


Fig. 14. Comparison of our averaged data with the ENDF/B-V evaluation from 200 to 300 keV.

ORNL-DWG 82-18037

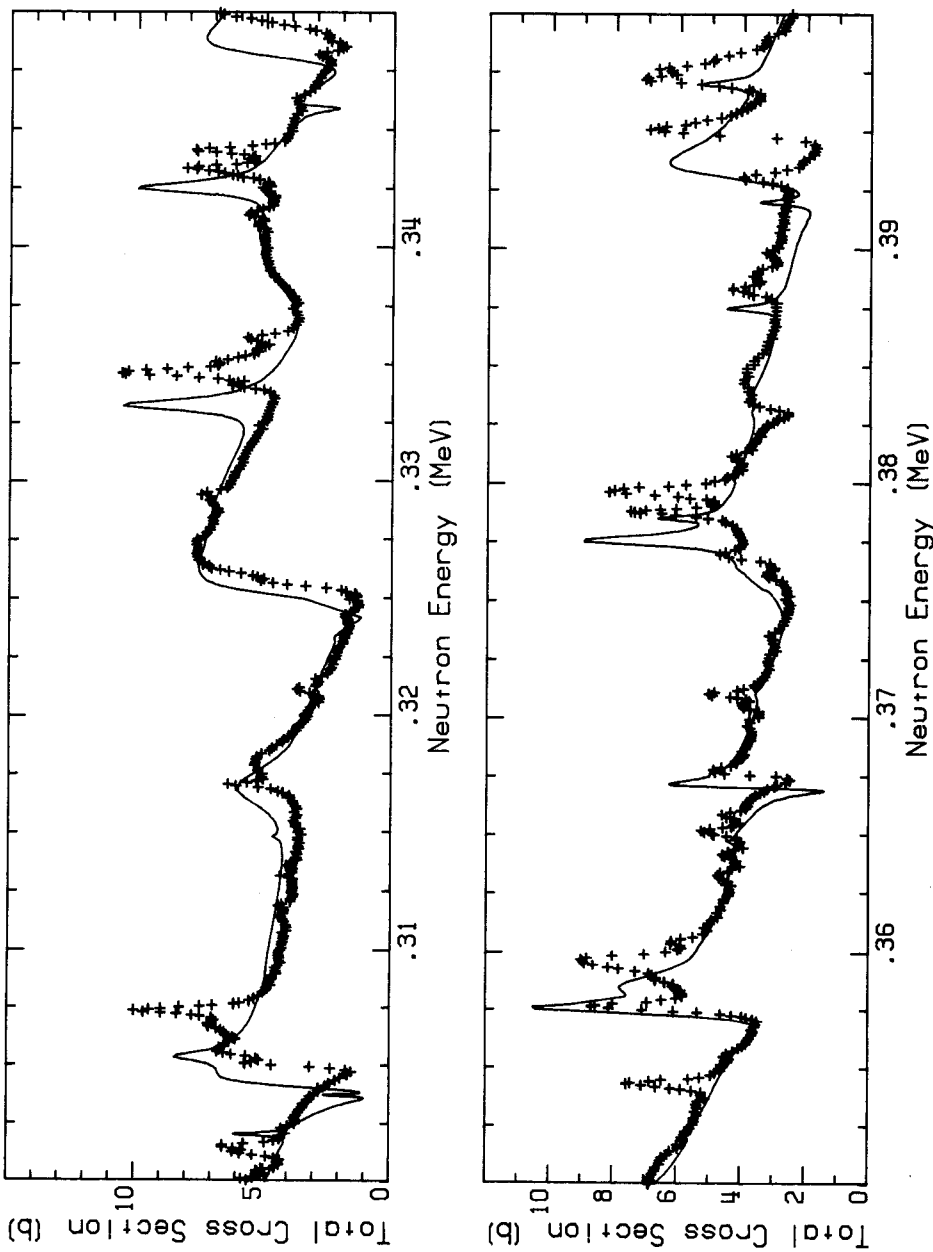


Fig. 15. Comparison of our averaged data with the ENDF/B-V evaluation from 300 to 400 keV.

ORNL-DWG 82-18038

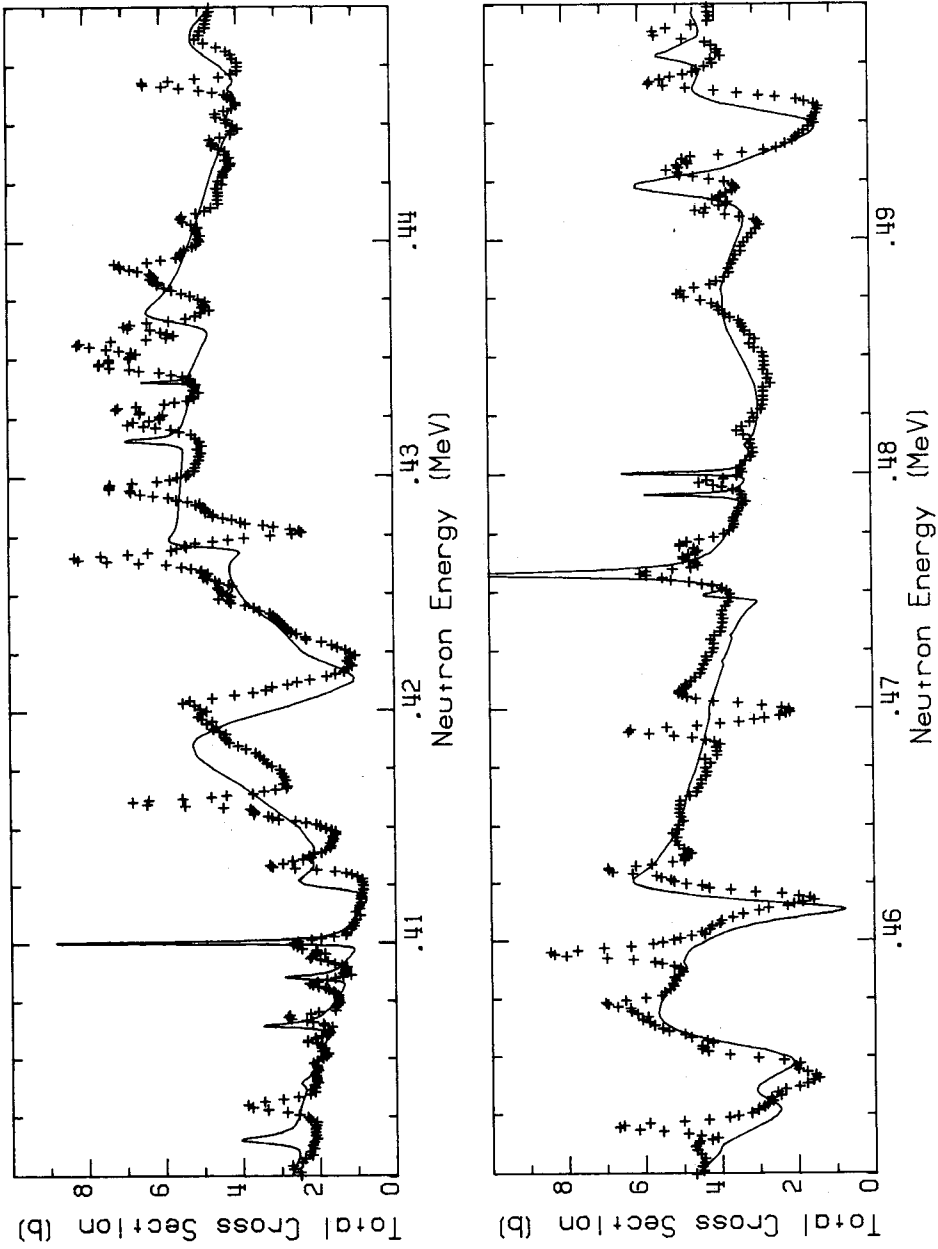


Fig. 16. Comparison of our averaged data with the ENDF/B-V evaluation from 400 to 500 keV.

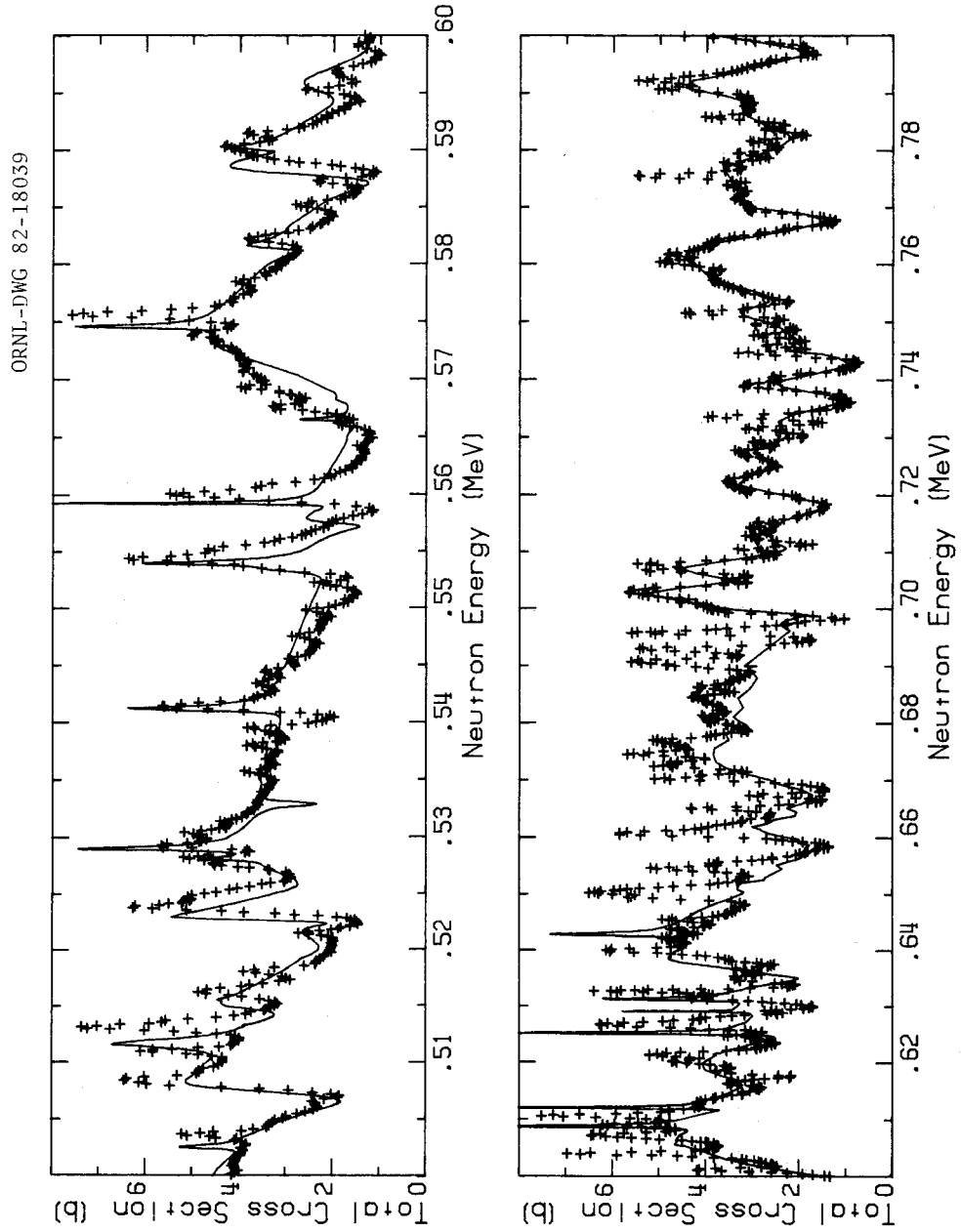


Fig. 17. Comparison of our averaged data with the ENDF/B-V evaluation from 500 to 800 keV.

ORNL-DWG 82-18040

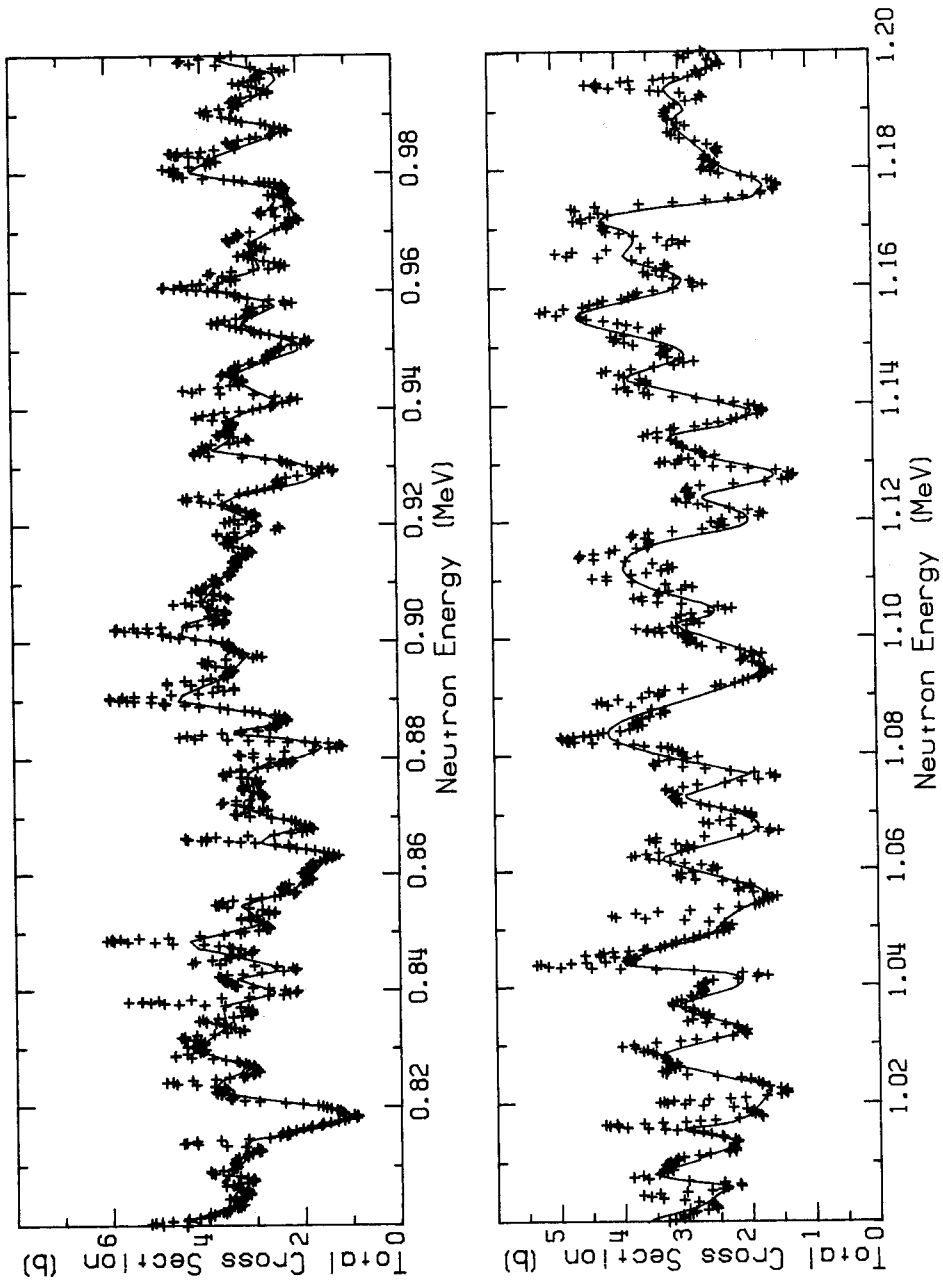


Fig. 18. Comparison of our averaged data with the ENDF/B-V evaluation from 800 keV to 1.2 MeV.

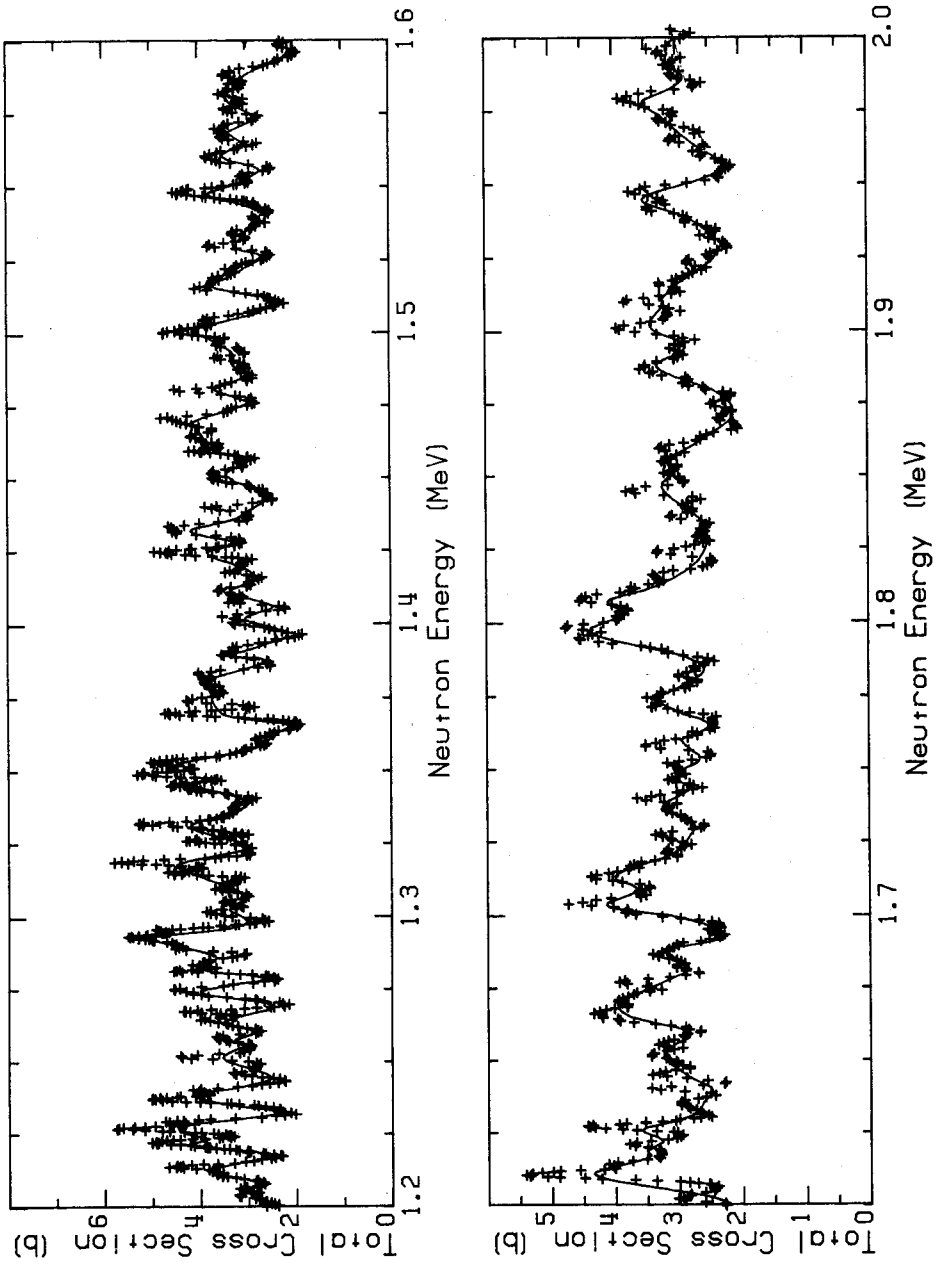


Fig. 19. Comparison of our averaged data with the ENDF/B-V evaluation from 1.2 to 2.0 MeV.

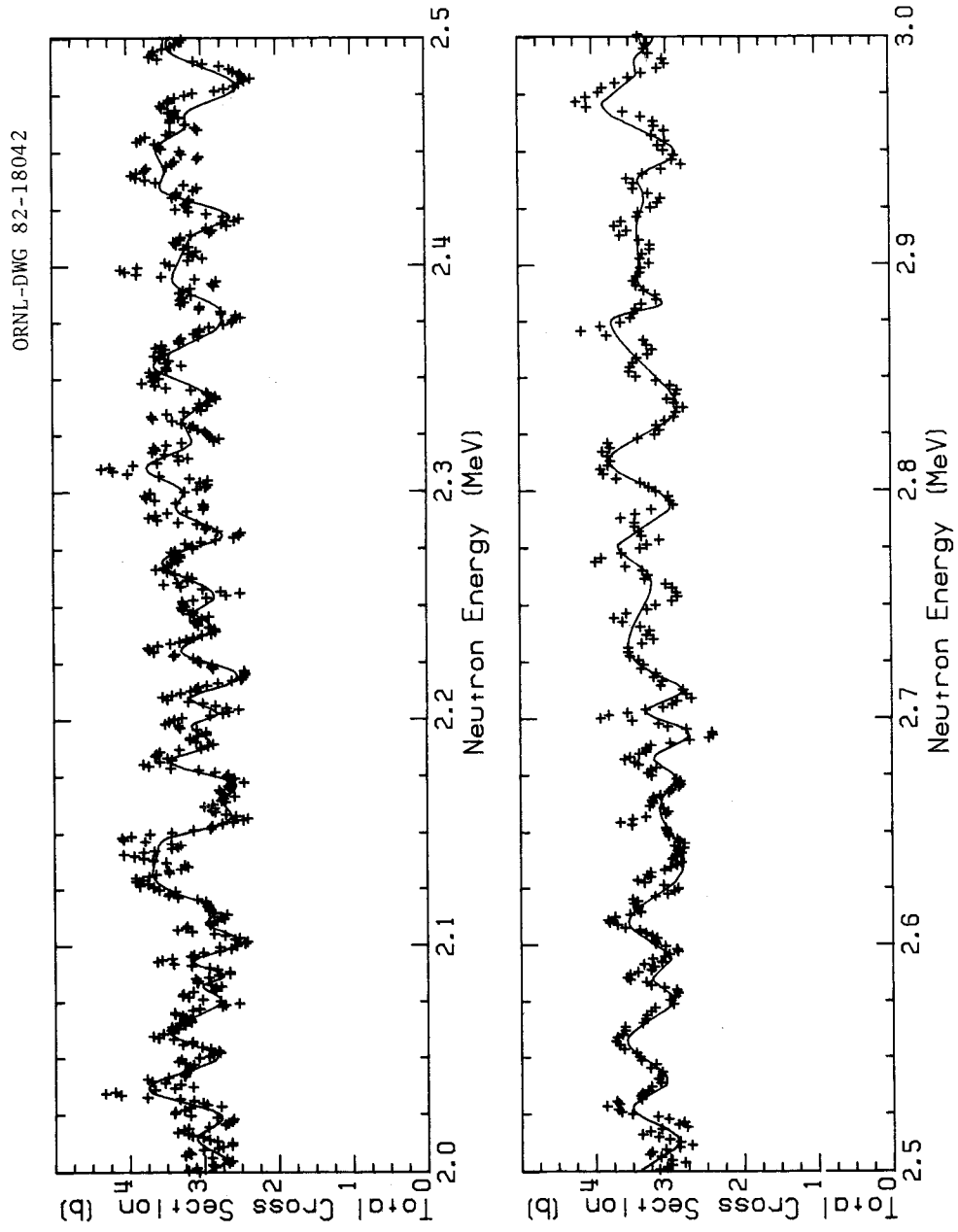


Fig. 20. Comparison of our averaged data with the ENDF/B-V evaluation from 2.0 to 3.0 MeV.

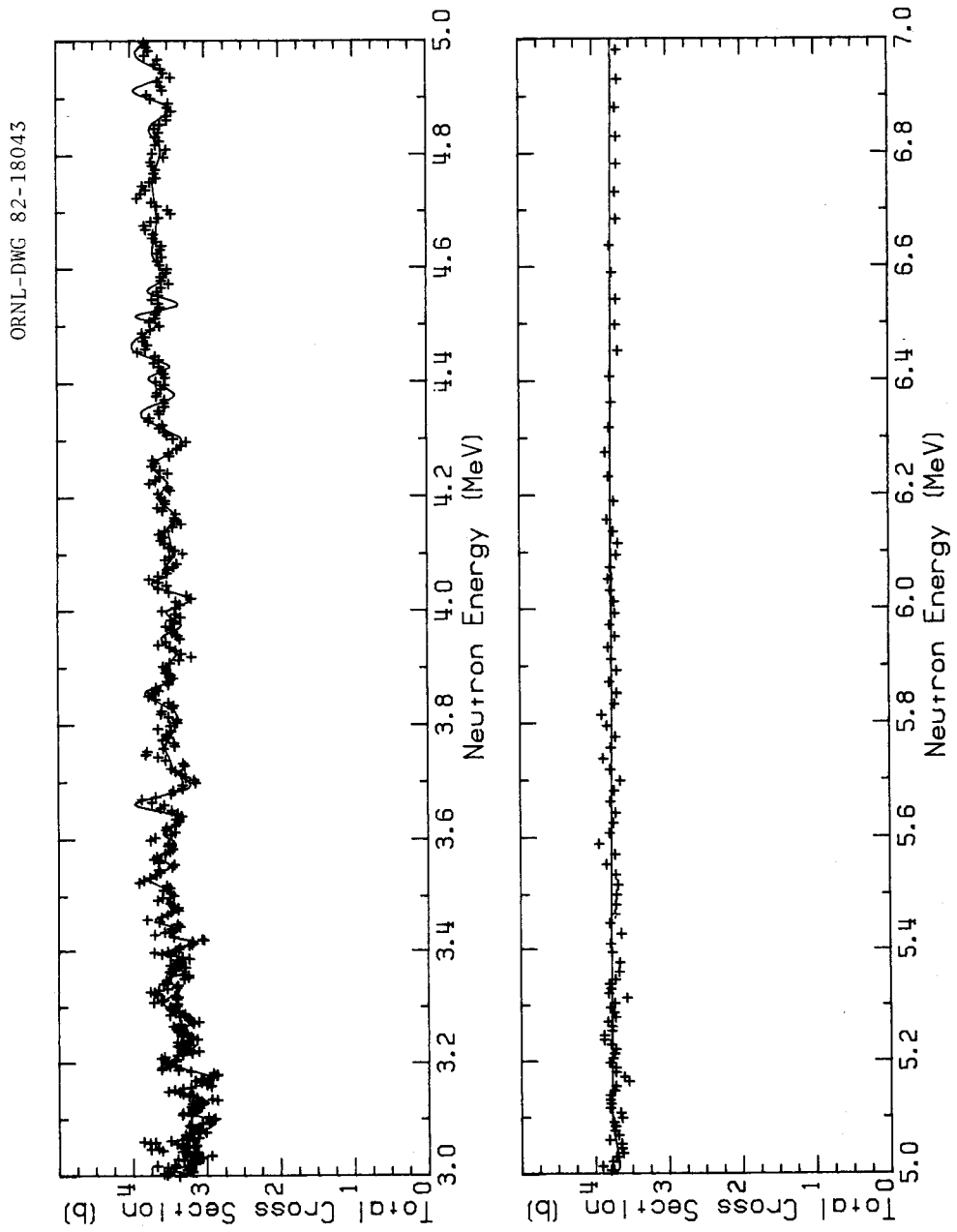


Fig. 21. Comparison of our averaged data with the ENDF/B-V evaluation from 3.0 to 7.0 MeV.

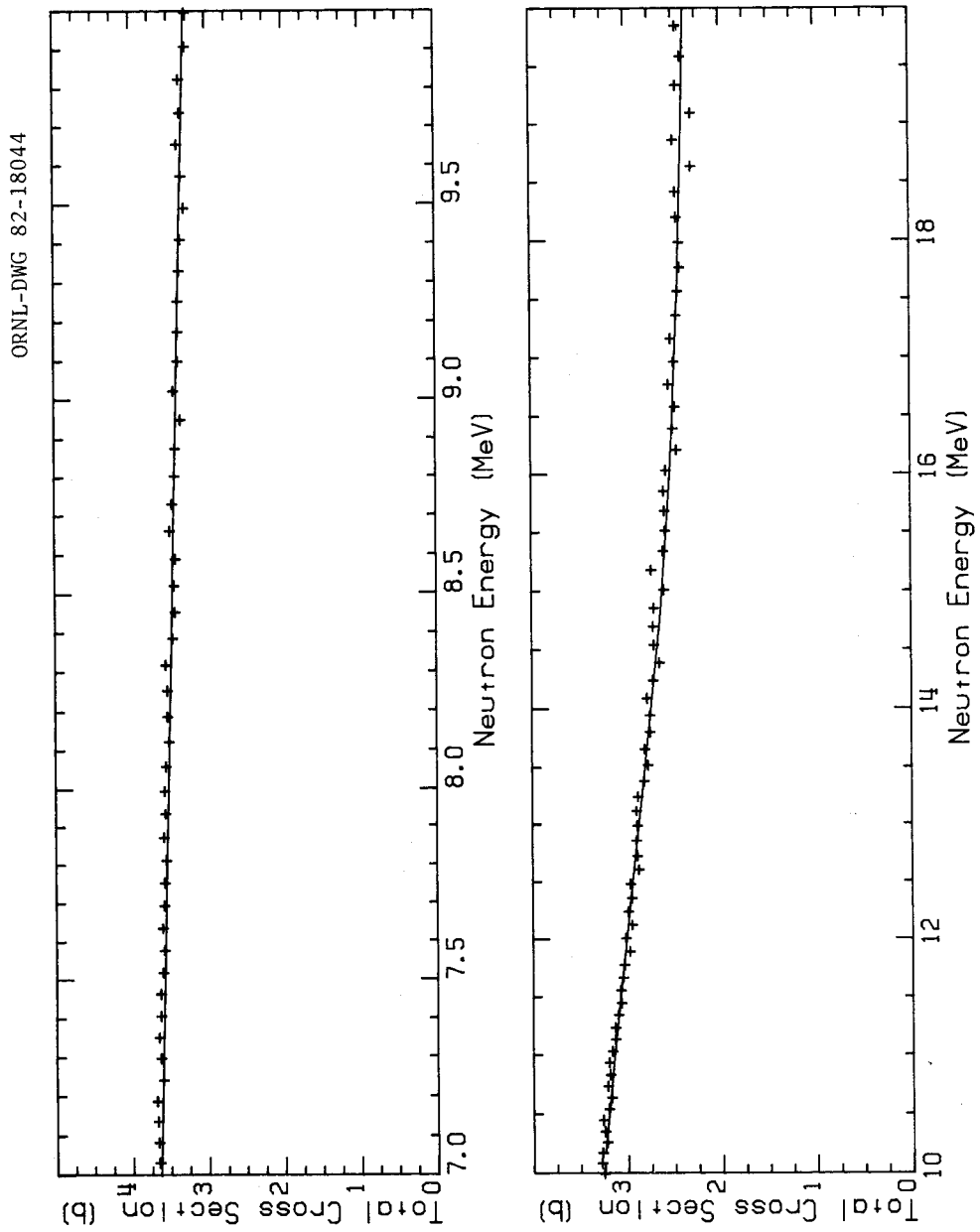


Fig. 22. Comparison of our averaged data with the ENDF/B-V evaluation from 7.0 to 20.0 MeV.

ORNL-DWG 82-18045

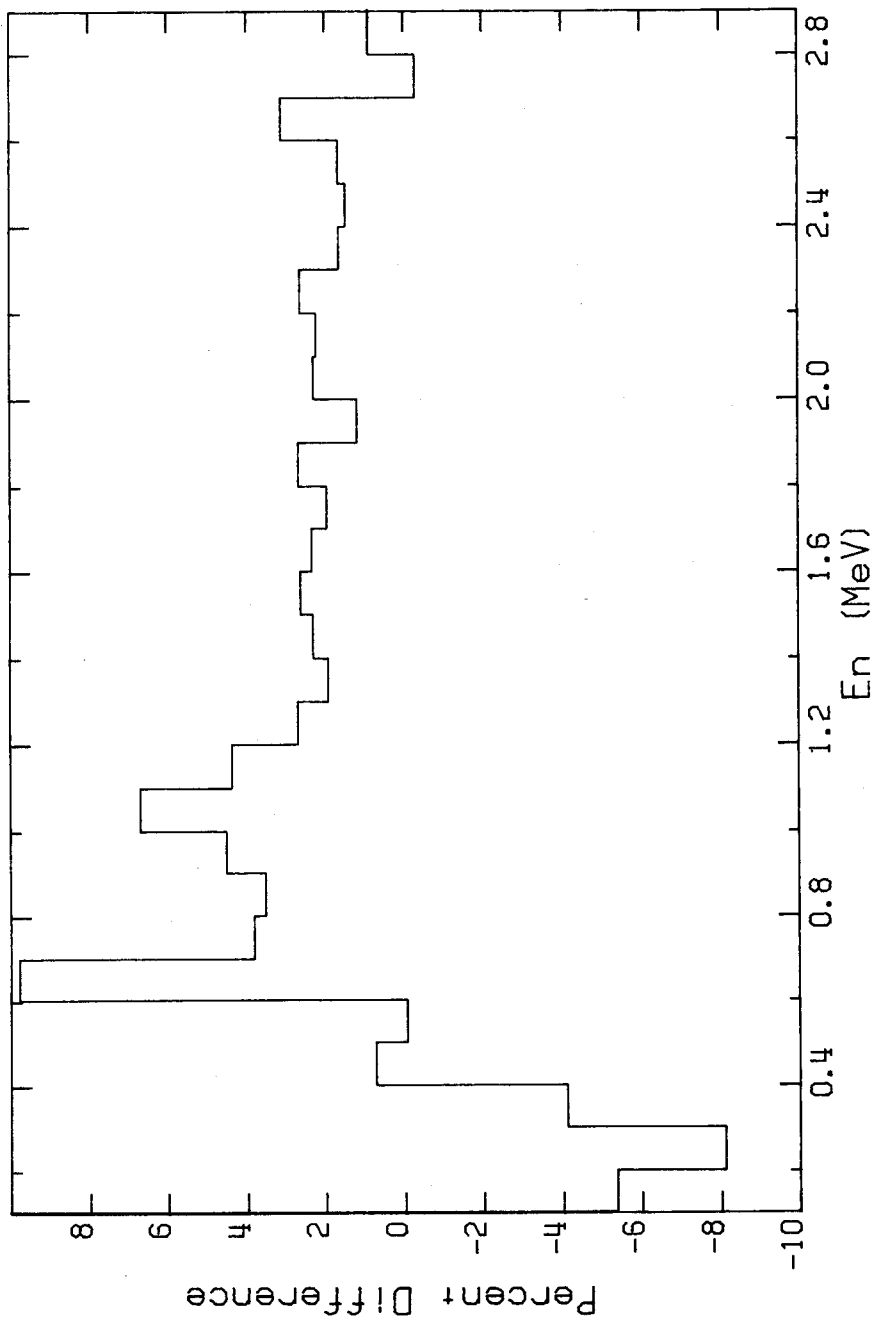


Fig. 23. Percent difference (EXPT-EVAL)/EXPT between our nickel total cross section and the ENDF/B-V evaluation from 0.1 to 2.9 MeV.

are indeed larger than the present evaluation, but not by the 15-20% implied by the thick-sample broomstick measurement (MA76, WE82). This raises the question as to whether the nickel broomstick benchmark may be in error.

6.2 COVARIANCE ANALYSIS RESULTS

As noted at the end of the last section, uncertainties and correlations on the input parameters involved in the cross-section determination were used to generate a covariance matrix for the output cross sections. Since this is the first application of such a detailed uncertainty analysis to an ORELA transmission measurement, we spent some time considering the effects which uncertainties on the input parameters had on the output uncertainties for the cross sections. Here we summarize some of those results.

6.2.1 *Uncertainty Analysis Results Where Cross Sections Have Been Averaged Into a 15-Group Set and All Correlations in Input Parameters Are Included*

In this case, all uncertainty information is included and should be considered as the primary uncertainty analysis result. Since we are averaging the data from $\sim 60,000$ points down to 15 groups, we can expect that the statistical uncertainty on each group will be very small, and the correlation matrix will be dominated by the longer range, systematic uncertainties.

For this first example, we present the complete output from the code ALEX, as it provides a convenient summary of the whole uncertainty analysis. For later cases, we will present only the final correlation matrix. This output for the first example is labeled as Table 9, and an explanation of its various sections is given here. The crunch boundaries given in Table 1 are given first, followed by the energy group boundaries for the final results (Table 5). Displayed next are the values of the 30 parameters and their uncertainties, expressed both in absolute units and as percentages. This information comes from Table 8. Following this is the correlation matrix for the input parameters. These numbers are derived from the algebraic expressions obtained in the last section and correspond to the non-zero entries in Table 7. The first column of this table lists the parameter number, followed by its standard deviation and its correlation with other parameters. The group boundaries and the quantity $\text{SIGMA} = \Sigma\sigma(E)\Delta E$ is given next, along with the values of the derivatives with respect to the parameters. For example, the first few terms are $\partial\sigma/\partial n$, $\partial\sigma/\partial m$, $\partial\sigma/\partial M$, etc., and are evaluated from the equations given in Sect. 5. Also note that effects of the summing of selected regions from each bias spectrum for the final sample-in and -out spectra are observed, for instance, in α_3 and α_4 , since data from these biases are not used for the lower energies. Following this, the group energy boundaries, average cross section within the group, and the total uncertainty for that group are given, along with the contributions of the statistical uncertainties for sample-in and -out, followed by the contribution to the total uncertainty by each of the thirty parameters. From this section of output we can observe the relative importance of each parameter to the analysis. The explicit relations used to calculate the total uncertainty for a group are given by

$$\Delta\sigma^2 = \Delta\sigma_{SI}^2 + \Delta\sigma_{SO}^2 + \sum_{\ell,\ell'} \sum_{j,k=1}^{30} \frac{\partial\sigma_{\ell}}{\partial P_j} (\delta P_j \delta P_k) \frac{\partial\sigma_{\ell'}}{\partial P_k} \quad (6.1)$$

Table 9.

***** INPUT DATA IS FOUND ON FILE "LFTM.DCL" *****

NCHN,NCHNMN= 55668 4175
 TIME DELAY (NS) AND FLIGHT PATH LENGTH (MM) ARE 836.000 AND 201442.

CRUNCH BOUNDARIES AND CHANNEL WIDTHS IN NANoseconds

34836	1.00000
7000	2.00000
8000	4.00000
5000	16.00000
2000	200.00000
3164	1000.00000

ENERGY INTERVALS IN MEV

1	0.022000	0.028000
2	0.030000	0.036000
3	0.036200	0.040900
4	0.040900	0.063000
5	0.067400	0.111000
6	0.111000	0.183000
7	0.183000	0.302000
8	0.302000	0.498000
9	0.498000	0.821000
10	0.821000	1.350000
11	1.350000	2.230000
12	2.230000	3.680000
13	3.680000	6.060000
14	6.060000	10.000000
15	10.000000	19.600000

PAR NO.	USED	PARAMETER	UNCERTAINTY	% UNCERTAINTY	
1	1	0.230400	0.000415	0.180	THICKNESS OF SAMPLE
2	2	19137531.000000	57412.593300	0.300	MONITOR FOR SAMPLE -IN
3	3	13610924.000000	68054.620100	0.500	MONITOR FOR SAMPLE -OUT
4	4	0.021000	0.006300	30.000	VRIANCE IN MAGNITUDE OF FLUX INTENSITY
5	5	1.260000	0.050400	4.000	ALPHA FOR BIAS 1, SAMPLE-IN
6	6	1.870000	0.074800	4.000	ALPHA FOR BIAS 2, SAMPLE-IN
7	7	2.310000	0.092400	4.000	ALPHA FOR BIAS 3, SAMPLE-IN
8	8	1.640000	0.065600	4.000	ALPHA FOR BIAS 4, SAMPLE-IN
9	9	0.910000	0.036400	4.000	ALPHA FOR BIAS 1, SAMPLE-OUT
10	10	1.330000	0.053200	4.000	ALPHA FOR BIAS 2, SAMPLE-OUT
11	11	1.640000	0.065600	4.000	ALPHA FOR BIAS 3, SAMPLE-OUT
12	12	1.160000	0.046400	4.000	ALPHA FOR BIAS 4, SAMPLE-OUT
13	13	1.180000	0.295000	25.000	BETA FOR SAMPLE-OUT
14	14	25.400000	1.000000	3.937	PSI
15	15	0.150000	0.058417	38.944	RATIO OF BETAS FOR BIAS 1 (R-1)
16	16	0.160000	0.051225	32.016	RATIO OF BETAS FOR BIAS 2 (R-2)
17	17	0.180000	0.057628	32.016	RATIO OF BETAS FOR BIAS 3 (R-3)
18	18	1440.000000	288.000000	20.000	G FOR BIAS 3, SAMPLE-IN
19	19	2.000000	0.072301	3.615	EXPONENT FOR SAMPLE-IN
20	20	2.130000	0.639000	30.000	E FOR BIAS 3, SAMPLE-IN
21	21	0.152000	0.076000	50.000	A FOR BIAS 3, SAMPLE-IN
22	22	-0.456000	0.228000	50.000	F FOR BIAS 3, SAMPLE-IN
23	23	69.000000	13.800000	20.000	G FOR BIAS 3, SAMPLE-OUT
24	24	1.000000	0.072301	7.230	EXPONENT FOR SAMPLE-OUT
25	25	2.660000	0.798000	30.000	E FOR BIAS 3, SAMPLE-OUT
26	26	0.190000	0.095000	50.000	A FOR BIAS 3, SAMPLE-OUT
27	27	-0.570000	0.285000	50.000	F FOR BIAS 3, SAMPLE-OUT
28	28	0.150000	0.010607	7.071	RATIO OF BIAS 1 TO 3 (S-1)
29	29	0.320000	0.022627	7.071	RATIO OF BIAS 2 TO 3 (S-2)
30	30	0.600000	0.042426	7.071	RATIO OF BIAS 4 TO 3 (S-4)

Table 9. (contd)

*****CORRELATION MATRIX FOR PARAMETERS

STD. DEV.	CORRELATION																														
	1	2	3	4	5	6	7	8	9	10	11	12	13	14	15	16	17	18	19	20	21	22	23	24	25	26	27	28	29	30	
1 4.14720E-04	100																														
2 57413.	0	100																													
3 68055.	0	0	100																												
4 6.30000E-03	0	0	0	100																											
5 5.04000E-02	0	0	0	0	100																										
6 7.48000E-02	0	0	0	0	0	100																									
7 9.24000E-02	0	0	0	0	0	0	100																								
8 6.56000E-02	0	0	0	0	0	0	0	100																							
9 3.64000E-02	0	0	0	0	0	0	0	0	100																						
10 5.32000E-02	0	0	0	0	0	0	0	0	0	100																					
11 6.56000E-02	0	0	0	0	0	0	0	0	0	0	100																				
12 4.64000E-02	0	0	0	0	0	0	0	0	0	0	0	100																			
13 0.29500	0	0	0	0	0	0	0	0	0	0	0	0	100																		
14 1.0000	0	0	0	0	0	0	0	0	0	0	0	0	0	100																	
15 5.84166E-02	0	0	0	0	0	0	0	0	0	0	0	0	0	0	100																
16 5.12250E-02	0	0	0	0	0	0	0	0	0	0	0	0	0	0	0	100															
17 5.76281E-02	0	0	0	0	0	0	0	0	0	0	0	0	0	0	0	0	100														
18 288.00	0	0	0	0	0	0	0	0	0	0	0	0	0	0	0	0	0	100													
19 7.23009E-02	0	0	0	0	0	0	0	0	0	0	0	0	0	0	0	0	0	0	100												
20 0.63900	0	0	0	0	0	0	0	0	0	0	0	0	0	0	0	0	0	0	0	100											
21 7.60000E-02	0	0	0	0	0	0	0	0	0	0	0	0	0	0	0	0	0	0	0	0	100										
22 0.22800	0	0	0	0	0	0	0	0	0	0	0	0	0	0	0	0	0	0	0	0	0	100									
23 13.800	0	0	0	0	0	0	0	0	0	0	0	0	0	0	0	0	0	0	0	0	0	0	100								
24 7.23009E-02	0	0	0	0	0	0	0	0	0	0	0	0	0	0	0	0	0	0	0	0	0	0	0	100							
25 0.79800	0	0	0	0	0	0	0	0	0	0	0	0	0	0	0	0	0	0	0	0	0	0	0	0	100						
26 9.50000E-02	0	0	0	0	0	0	0	0	0	0	0	0	0	0	0	0	0	0	0	0	0	0	0	0	0	100					
27 0.28500	0	0	0	0	0	0	0	0	0	0	0	0	0	0	0	0	0	0	0	0	0	0	0	0	0	0	100				
28 1.06066E-02	0	0	0	0	0	0	0	0	0	0	0	0	0	0	0	0	0	0	0	0	0	0	0	0	0	0	0	100			
29 2.26274E-02	0	0	0	0	0	0	0	0	0	0	0	0	0	0	0	0	0	0	0	0	0	0	0	0	0	0	0	0	100		
30 4.24264E-02	0	0	0	0	0	0	0	0	0	0	0	0	0	0	0	0	0	0	0	0	0	0	0	0	0	0	0	0	0	100	

RATIO OF BETA (SAMPLE-IN) TO BETA (SAMPLE-OUT) IS 0.540691093

BORON BOUNDARIES
 3000
 17000
 26000
 45000
 60000

UPPER END OF BIAS BOUNDARY
 3500
 15000
 26000
 45000
 60000

BIASES INCLUDED
 4 0 0 0
 1 2 3 4
 1 2 3 0
 1 2 0 0
 1 0 0 0

 PRE-EXISTING DERIVATIVE FILE USED BY THIS RUN IS CALLED TMFIX.ODF
 PRE-EXISTING SUMMED DERIVATIVE FILE USED BY THIS RUN IS CALLED XLARGE.ODF

Table 9. (contd)

***** SUMMED CROSS SECTION AND PARTIAL DERIVATIVES

EL	EH	SIGMA	DERIVATIVES WRT PARAMETERS							
			1 THICKNESS OF SAMPLE	2 MONITOR FOR SAMPLE -IN	3 MONITOR FOR SAMPLE -OUT	4 VARIANCE IN MAGNITUDE OF FLUX INTENSITY	5 ALPHA FOR BIAS 1, SAMPLE-IN	6 ALPHA FOR BIAS 2, SAMPLE-IN	7 ALPHA FOR BIAS 3, SAMPLE-IN	
1	0.02200	0.02800	7.6703E-02	-0.3329	1.3608E-09	-1.9133E-09	9.5676E-03	5.5594E-03	0.0000	0.0000
2	0.03000	0.03600	7.0505E-02	-0.3060	1.3608E-09	-1.9133E-09	9.5415E-03	2.9416E-03	0.0000	0.0000
3	0.03620	0.04090	4.1531E-02	-0.1803	1.0659E-09	-1.4987E-09	7.4700E-03	6.9897E-04	0.0000	0.0000
4	0.04090	0.06300	0.1235	-0.5360	5.0121E-09	-7.0473E-09	3.5256E-02	1.5255E-03	4.9871E-04	0.0000
5	0.06740	0.11100	0.3190	-1.385	9.8882E-09	-1.3903E-08	7.0261E-02	1.8436E-03	1.8436E-03	0.0000
6	0.11100	0.18300	0.4088	-1.774	1.6329E-08	-2.2960E-08	0.1186	9.5936E-04	9.5936E-04	0.0000
7	0.18300	0.30200	0.6895	-2.993	2.6988E-08	-3.7947E-08	0.2069	6.0706E-04	6.0706E-04	0.0000
8	0.30200	0.49800	0.8207	-3.562	4.4452E-08	-6.2501E-08	0.3809	2.7630E-04	2.7630E-04	2.0593E-04
9	0.49800	0.82100	1.076	-4.670	7.3254E-08	-1.0300E-07	0.7463	1.8048E-04	1.8048E-04	1.8048E-04
10	0.82100	1.35000	1.731	-7.515	1.1997E-07	-1.6869E-07	1.305	2.0349E-04	2.0349E-04	2.0349E-04
11	1.35000	2.23000	2.800	-12.15	1.9958E-07	-2.8062E-07	1.577	5.1600E-04	5.1600E-04	5.1600E-04
12	2.23000	3.68000	4.861	-21.10	3.2885E-07	-4.6238E-07	1.817	1.8412E-03	1.8412E-03	1.8412E-03
13	3.68000	6.06000	8.732	-37.90	5.3977E-07	-7.5894E-07	2.494	4.3393E-03	4.3393E-03	4.3393E-03
14	6.06000	10.00000	13.98	-60.68	8.9357E-07	-1.2564E-06	3.485	6.5840E-03	6.5840E-03	6.5840E-03
15	10.00000	19.60000	26.29	-114.1	2.1772E-06	-3.0613E-06	7.201	4.2754E-02	4.2754E-02	4.2754E-02

DERIVATIVES WRT PAR, CONTINUED

PAR NUM	8		9		10		11		12		13		14		15		16	
	ALPHA FOR BIAS 4, SAMPLE-IN	ALPHA FOR BIAS 1, SAMPLE-OUT	ALPHA FOR BIAS 2, SAMPLE-OUT	ALPHA FOR BIAS 3, SAMPLE-OUT	ALPHA FOR BIAS 4, SAMPLE-OUT	BETA FOR SAMPLE-OUT	PSI	RATIO OF BETAS FOR BIAS 1 (R-1)	RATIO OF BETAS FOR BIAS 2 (R-2)									
1	0.0000	-3.0728E-04	0.0000	0.0000	0.0000	-1.2090E-06	-2.0401E-07	-9.5108E-06	0.0000									
2	0.0000	-2.1536E-04	0.0000	0.0000	0.0000	-1.3691E-06	-2.0080E-07	-1.0770E-05	0.0000									
3	0.0000	-1.1899E-04	0.0000	0.0000	0.0000	-9.5330E-07	-1.2970E-07	-7.4993E-06	0.0000									
4	0.0000	-2.9755E-04	-4.9531E-05	0.0000	0.0000	-4.2326E-06	-4.9264E-07	-2.7273E-05	-5.6467E-06									
5	0.0000	-2.8777E-04	-2.8777E-04	0.0000	0.0000	-1.2877E-05	-1.1522E-06	-4.9015E-05	-4.9015E-05									
6	0.0000	-2.4511E-04	-2.4511E-04	0.0000	0.0000	-1.6560E-05	-1.1674E-06	-6.3034E-05	-6.3034E-05									
7	0.0000	-1.8406E-04	-1.8406E-04	0.0000	0.0000	-1.7364E-05	-9.5673E-07	-6.6094E-05	-6.6094E-05									
8	0.0000	-1.3653E-04	-1.3653E-04	-1.0531E-04	0.0000	-2.4516E-05	-1.0411E-06	-6.3932E-05	-6.3932E-05									
9	0.0000	-1.1240E-04	-1.1240E-04	-1.1240E-04	0.0000	-2.6795E-05	-8.9525E-07	-6.4527E-05	-6.4527E-05									
10	1.1326E-04	-1.3199E-04	-1.3199E-04	-1.3199E-04	-7.1900E-05	-7.9756E-05	-1.9908E-06	-8.9464E-05	-8.9464E-05									
11	5.1600E-04	-3.4750E-04	-3.4750E-04	-3.4750E-04	-3.4750E-04	-3.3845E-04	-6.6779E-06	-2.6803E-04	-2.6803E-04									
12	1.8412E-03	-1.1901E-03	-1.1901E-03	-1.1901E-03	-1.1901E-03	-1.2710E-03	-1.9648E-05	-1.0066E-03	-1.0066E-03									
13	4.3393E-03	-2.6183E-03	-2.6183E-03	-2.6183E-03	-2.6183E-03	-2.9995E-03	-3.6606E-05	-2.3754E-03	-2.3754E-03									
14	6.5840E-03	-4.1036E-03	-4.1036E-03	-4.1036E-03	-4.1036E-03	-4.9895E-03	-4.7102E-05	-3.9514E-03	-3.9514E-03									
15	4.2754E-02	-3.2732E-02	-3.2732E-02	-3.2732E-02	-3.2732E-02	-4.2098E-02	-2.8757E-04	-3.3339E-02	-3.3339E-02									

DERIVATIVES WRT PAR, CONTINUED

PAR NUM	17		18		19		20		21		22		23		24		25	
	RATIO OF BETAS FOR BIAS 3 (R-3)	G FOR BIAS 3, SAMPLE-IN	EXPONENT FOR SAMPLE-IN	E FOR BIAS 3, SAMPLE-IN	A FOR BIAS 3, SAMPLE-IN	F FOR BIAS 3, SAMPLE-IN	G FOR BIAS 3, SAMPLE-OUT	EXPONENT FOR SAMPLE-OUT	E FOR BIAS 3, SAMPLE-OUT									
1	0.0000	9.3622E-08	-6.1290E-04	0.0000	0.0000	0.0000	-4.9789E-07	1.5553E-04	0.0000									
2	0.0000	6.7049E-08	-4.2437E-04	0.0000	0.0000	0.0000	-4.0215E-07	1.2170E-04	0.0000									
3	0.0000	1.8800E-08	-1.1676E-04	0.0000	0.0000	0.0000	-2.3982E-07	7.1315E-05	0.0000									
4	0.0000	1.0197E-07	-6.0442E-04	0.0000	0.0000	0.0000	-9.5396E-07	2.7299E-04	0.0000									
5	0.0000	3.4972E-07	-1.9635E-03	0.0000	0.0000	0.0000	-2.7515E-06	7.3900E-04	0.0000									
6	0.0000	3.1071E-07	-1.6269E-03	0.0000	0.0000	0.0000	-2.9807E-06	7.5108E-04	0.0000									
7	0.0000	3.1071E-07	-1.5241E-03	0.0000	0.0000	0.0000	-2.8689E-06	6.7377E-04	0.0000									
8	-5.0612E-05	4.9727E-08	-2.3270E-04	3.0272E-04	0.0000	0.0000	-5.6790E-07	1.2743E-04	-1.5480E-04									
9	-6.4527E-05	0.0000	0.0000	2.6147E-04	6.1871E-05	3.8360E-06	0.0000	0.0000	-1.6212E-04									
10	-8.9464E-05	0.0000	0.0000	0.0000	5.1115E-03	3.6708E-04	0.0000	0.0000	0.0000									
11	-2.6803E-04	0.0000	0.0000	0.0000	1.1564E-02	1.0681E-03	0.0000	0.0000	0.0000									
12	-1.0066E-03	0.0000	0.0000	0.0000	3.2220E-02	3.8114E-03	0.0000	0.0000	0.0000									
13	-2.3754E-03	0.0000	0.0000	0.0000	5.9917E-02	8.9823E-03	0.0000	0.0000	0.0000									
14	-3.9514E-03	0.0000	0.0000	0.0000	7.0600E-02	1.3629E-02	0.0000	0.0000	0.0000									
15	-3.3339E-02	0.0000	0.0000	0.0000	0.3326	8.8501E-02	0.0000	0.0000	0.0000									

DERIVATIVES WRT PAR, CONTINUED

PAR NUM	26		27		28		29		30	
	A FOR BIAS 3, SAMPLE-OUT	F FOR BIAS 3, SAMPLE-OUT	RATIO OF BIAS 1 TO 3 (S-1)	RATIO OF BIAS 2 TO 3 (S-2)	RATIO OF BIAS 3 TO 3 (S-3)	RATIO OF BIAS 4 TO 3 (S-4)				
1	0.0000	0.0000	-2.2903E-04	0.0000	0.0000	0.0000				
2	0.0000	0.0000	-1.8499E-04	0.0000	0.0000	0.0000				
3	0.0000	0.0000	-1.1032E-04	0.0000	0.0000	0.0000				
4	0.0000	0.0000	-3.1600E-04	-5.7572E-05	0.0000	0.0000				
5	0.0000	0.0000	-4.0394E-04	-4.0394E-04	0.0000	0.0000				
6	0.0000	0.0000	-4.3759E-04	-4.3759E-04	0.0000	0.0000				
7	0.0000	0.0000	-4.2118E-04	-4.2118E-04	0.0000	0.0000				
8	0.0000	0.0000	-3.6349E-04	-3.6349E-04	0.0000	0.0000				
9	-5.0166E-05	-3.1111E-06	-2.9864E-04	-2.9864E-04	0.0000	0.0000				
10	-3.3095E-03	-2.3716E-04	-2.7839E-04	-2.7839E-04	-1.4065E-04	0.0000				
11	-7.7764E-03	-7.1932E-04	-5.1570E-04	-5.1570E-04	-5.1570E-04	0.0000				
12	-2.0856E-02	-2.4636E-03	-1.2359E-03	-1.2359E-03	-1.2359E-03	0.0000				
13	-3.6211E-02	-5.4199E-03	-1.8313E-03	-1.8313E-03	-1.8313E-03	0.0000				
14	-4.3891E-02	-8.4945E-03	-1.6896E-03	-1.6896E-03	-1.6896E-03	0.0000				
15	-0.2533	-6.7754E-02	-4.5961E-03	-4.5961E-03	-4.5961E-03	0.0000				

Table 9. (contd)

***** CROSS SECTIONS AND CONTRIBUTIONS TO UNCERTAINTIES

EL	EH	SIGMA	UNCERT.	(S-I)	(S-O)	DERIVATIVES WRT PAR, TIMES DELPAR					
						1 THICKNESS OF SAMPLE	2 MONITOR FOR SAMPLE -IN	3 MONITOR FOR SAMPLE -OUT	4 VRIANCE IN MAGNITUDE OF FLUX	5 ALPHA FOR BIAS 1, SAMPLE-IN INTENSITY	
1	0.02200	0.02800	12.78377	0.06560	0.02782	0.00525	2.3011E-02	1.3021E-02	2.1701E-02	1.0046E-02	4.6699E-02
2	0.03000	0.03600	11.75086	0.04917	0.02375	0.00542	2.1152E-02	1.3021E-02	2.1701E-02	1.0019E-02	2.4710E-02
3	0.03620	0.04090	8.83632	0.03548	0.01307	0.00575	1.5905E-02	1.3021E-02	2.1701E-02	1.0013E-02	7.4953E-03
4	0.04090	0.06300	5.58761	0.03037	0.00742	0.00238	1.0058E-02	1.3021E-02	2.1701E-02	1.0050E-02	3.4790E-03
5	0.06740	0.11100	7.31754	0.03101	0.00436	0.00181	1.3172E-02	1.3021E-02	2.1701E-02	1.0152E-02	2.1312E-03
6	0.11100	0.18300	5.67804	0.02942	0.00270	0.00146	1.0220E-02	1.3021E-02	2.1701E-02	1.0378E-02	6.7156E-04
7	0.18300	0.30200	5.79451	0.02958	0.00182	0.00112	1.0430E-02	1.3021E-02	2.1701E-02	1.0956E-02	2.5711E-04
8	0.30200	0.49800	4.18720	0.02917	0.00110	0.00087	7.5370E-03	1.3021E-02	2.1701E-02	1.2243E-02	7.1049E-05
9	0.49800	0.82100	3.33150	0.02983	0.00080	0.00071	5.9967E-03	1.3021E-02	2.1701E-02	1.4557E-02	2.8161E-05
10	0.82100	1.35000	3.27286	0.03031	0.00078	0.00071	5.8911E-03	1.3021E-02	2.1701E-02	1.5541E-02	1.9387E-05
11	1.35000	2.23000	3.18206	0.02837	0.00108	0.00097	5.7277E-03	1.3021E-02	2.1701E-02	1.1292E-02	2.9552E-05
12	2.23000	3.68000	3.35210	0.02741	0.00176	0.00151	6.0338E-03	1.3021E-02	2.1701E-02	7.8939E-03	6.3999E-05
13	3.68000	6.06000	3.66883	0.02731	0.00233	0.00193	6.6039E-03	1.3021E-02	2.1701E-02	6.6025E-03	9.1891E-05
14	6.06000	10.00000	3.54833	0.02699	0.00254	0.00212	6.3870E-03	1.3021E-02	2.1701E-02	5.5721E-03	8.4222E-05
15	10.00000	19.60000	2.73853	0.02745	0.00436	0.00402	4.9294E-03	1.3021E-02	2.1701E-02	4.7259E-03	2.2446E-04

DERIVATIVES WRT PAR, TIMES DELPAR, CONTINUED									
PAR NUMBER	6	7	8	9	10	11	12	13	14
	ALPHA FOR BIAS 2, SAMPLE-IN	ALPHA FOR BIAS 3, SAMPLE-IN	ALPHA FOR BIAS 4, SAMPLE-IN	ALPHA FOR BIAS 1, SAMPLE-OUT	ALPHA FOR BIAS 2, SAMPLE-OUT	ALPHA FOR BIAS 3, SAMPLE-OUT	ALPHA FOR BIAS 4, SAMPLE-OUT	BETA FOR SAMPLE-OUT	PSI
1	0.0000	0.0000	0.0000	1.8642E-03	0.0000	0.0000	0.0000	5.9443E-05	3.4002E-05
2	0.0000	0.0000	0.0000	1.3065E-03	0.0000	0.0000	0.0000	6.7312E-05	3.3467E-05
3	0.0000	0.0000	0.0000	9.2158E-04	0.0000	0.0000	0.0000	5.9835E-05	2.7595E-05
4	1.6879E-03	0.0000	0.0000	4.9008E-04	1.1923E-04	0.0000	0.0000	5.6498E-05	2.2292E-05
5	3.1629E-03	0.0000	0.0000	2.4025E-04	3.5113E-04	0.0000	0.0000	8.7124E-05	2.6427E-05
6	9.9677E-04	0.0000	0.0000	1.2392E-04	1.8111E-04	0.0000	0.0000	6.7849E-05	1.6214E-05
7	3.8158E-04	0.0000	0.0000	5.6301E-05	8.2287E-05	0.0000	0.0000	4.3045E-05	8.0398E-06
8	1.0545E-04	9.7081E-05	0.0000	2.5356E-05	3.7059E-05	3.5246E-05	0.0000	3.6899E-05	5.3118E-06
9	4.1795E-05	5.1629E-05	0.0000	1.2667E-05	1.8514E-05	2.2829E-05	0.0000	2.4472E-05	2.7717E-06
10	2.8773E-05	3.5543E-05	1.4045E-05	9.0818E-06	1.3273E-05	1.6367E-05	6.3066E-06	4.4477E-05	3.7634E-06
11	4.3860E-05	5.4180E-05	3.8465E-05	1.4374E-05	2.1008E-05	2.5904E-05	1.8323E-05	1.1346E-04	7.5885E-06
12	9.4982E-05	1.1733E-04	8.3300E-05	2.9876E-05	4.3665E-05	5.3843E-05	3.8084E-05	2.5858E-04	1.3551E-05
13	1.3638E-04	1.6847E-04	1.1960E-04	4.0044E-05	5.8527E-05	7.2168E-05	5.1046E-05	3.7178E-04	1.5381E-05
14	1.2500E-04	1.5441E-04	1.0962E-04	3.7912E-05	5.5409E-05	6.8324E-05	4.8327E-05	3.7358E-04	1.1955E-05
15	3.3313E-04	4.1151E-04	2.9215E-04	1.2411E-04	1.8139E-04	2.2367E-04	1.5820E-04	1.2936E-03	2.9955E-05

DERIVATIVES WRT PAR, TIMES DELPAR, CONTINUED									
PAR NUMBER	15	16	17	18	19	20	21	22	23
	RATIO OF BETAS FOR BIAS 1 (R-1)	RATIO OF BETAS FOR BIAS 2 (R-2)	RATIO OF BETAS FOR BIAS 3 (R-3)	G FOR BIAS 3, SAMPLE-IN	EXPONENT FOR SAMPLE-IN	E FOR BIAS 3, SAMPLE-IN	A FOR BIAS 3, SAMPLE-IN	F FOR BIAS 3, SAMPLE-IN	G FOR BIAS 3, SAMPLE-OUT
1	9.2598E-05	0.0000	0.0000	4.4938E-03	7.3855E-03	0.0000	0.0000	0.0000	1.1451E-03
2	1.0486E-04	0.0000	0.0000	3.2183E-03	5.1137E-03	0.0000	0.0000	0.0000	9.2494E-04
3	9.3209E-05	0.0000	0.0000	1.1520E-03	1.7961E-03	0.0000	0.0000	0.0000	7.0416E-04
4	7.2091E-05	1.3088E-05	0.0000	1.3288E-03	1.9774E-03	0.0000	0.0000	0.0000	5.9596E-04
5	6.5671E-05	5.7586E-05	0.0000	2.3101E-03	3.2560E-03	0.0000	0.0000	0.0000	8.7088E-04
6	5.1142E-05	4.4846E-05	0.0000	1.2428E-03	1.6337E-03	0.0000	0.0000	0.0000	5.7130E-04
7	3.2445E-05	2.8451E-05	0.0000	7.5197E-04	9.2602E-04	0.0000	0.0000	0.0000	3.3269E-04
8	1.9054E-05	1.6709E-05	1.4881E-05	7.3068E-05	8.5840E-05	9.8691E-04	0.0000	0.0000	3.9985E-05
9	1.1670E-05	1.0233E-05	1.1513E-05	0.0000	0.0000	5.1727E-04	1.4558E-05	2.7077E-06	0.0000
10	9.8794E-06	8.6632E-06	9.7461E-06	0.0000	0.0000	0.0000	7.3436E-04	1.5821E-04	0.0000
11	1.7793E-05	1.5602E-05	1.7553E-05	0.0000	0.0000	0.0000	9.9875E-04	2.7674E-04	0.0000
12	4.0552E-05	3.5559E-05	4.0004E-05	0.0000	0.0000	0.0000	1.6888E-03	5.9930E-04	0.0000
13	5.8304E-05	5.1126E-05	5.7517E-05	0.0000	0.0000	0.0000	1.9133E-03	8.6049E-04	0.0000
14	5.8586E-05	5.1373E-05	5.7795E-05	0.0000	0.0000	0.0000	1.3618E-03	7.8867E-04	0.0000
15	2.0287E-04	1.7790E-04	2.0013E-04	0.0000	0.0000	0.0000	2.6330E-03	2.1019E-03	0.0000

DERIVATIVES WRT PAR, TIMES DELPAR, CONTINUED									
PAR NUMBER	24	25	26	27	28	29	30		
	EXPONENT FOR SAMPLE-OUT	E FOR BIAS 3, SAMPLE-OUT	A FOR BIAS 3, SAMPLE-OUT	F FOR BIAS 3, SAMPLE-OUT	RATIO OF BIAS 1 TO 3 (S-1)	RATIO OF BIAS 2 TO 3 (S-2)	RATIO OF BIAS 4 TO 3 (S-4)		
1	1.8742E-03	0.0000	0.0000	0.0000	4.0487E-04	0.0000	0.0000		
2	1.4665E-03	0.0000	0.0000	0.0000	3.2702E-04	0.0000	0.0000		
3	1.0971E-03	0.0000	0.0000	0.0000	2.4896E-04	0.0000	0.0000		
4	8.9308E-04	0.0000	0.0000	0.0000	1.5166E-04	5.8946E-05	0.0000		
5	1.2255E-03	0.0000	0.0000	0.0000	9.8267E-05	2.0964E-04	0.0000		
6	7.5422E-04	0.0000	0.0000	0.0000	6.4463E-05	1.3752E-04	0.0000		
7	4.0937E-04	0.0000	0.0000	0.0000	3.7540E-05	8.0085E-05	0.0000		
8	4.7005E-05	6.3027E-04	0.0000	0.0000	1.9670E-05	4.1964E-05	0.0000		
9	0.0000	4.0054E-04	1.4755E-05	2.7451E-06	9.8067E-06	2.0921E-05	0.0000		
10	0.0000	0.0000	5.9433E-04	1.2777E-04	5.5817E-06	1.1908E-05	1.1281E-05		
11	0.0000	0.0000	8.3950E-04	2.3296E-04	6.2157E-06	1.3260E-05	2.4863E-05		
12	0.0000	0.0000	1.3664E-03	4.8422E-04	9.0407E-06	1.9287E-05	3.6163E-05		
13	0.0000	0.0000	1.4454E-03	6.4902E-04	8.1612E-06	1.7411E-05	3.2645E-05		
14	0.0000	0.0000	1.0583E-03	6.1445E-04	4.5485E-06	9.7034E-06	1.8194E-05		
15	0.0000	0.0000	2.5070E-03	2.0115E-03	5.0780E-06	1.0833E-05	2.0312E-05		

Table 9. (contd)

***** FINAL COVARIANCE MATRIX

	ELOW	EHIGH	% STD.DEV.	CORRELATION																					
				1	2	3	4	5	6	7	8	9	10	11	12	13	14	15							
1	0.02200	0.02800	0.51	100																					
2	0.03000	0.03600	0.42	75	100																				
3	0.03620	0.04090	0.40	63	73	100																			
4	0.04090	0.06300	0.54	58	70	86	100																		
5	0.06740	0.11100	0.42	57	71	88	95	100																	
6	0.11100	0.18300	0.52	53	68	88	96	97	100																
7	0.18300	0.30200	0.51	52	68	88	96	97	99	100															
8	0.30200	0.49800	0.70	50	65	86	95	96	99	99	100														
9	0.49800	0.82100	0.90	48	63	84	94	94	97	98	99	100													
10	0.82100	1.35000	0.93	48	62	83	93	93	97	97	99	100	100												
11	1.35000	2.23000	0.89	48	63	84	94	95	98	98	99	99	99	100											
12	2.23000	3.68000	0.82	49	63	84	94	95	97	98	98	97	96	99	100										
13	3.68000	6.06000	0.74	49	64	84	94	94	97	97	97	95	95	98	99	100									
14	6.06000	10.00000	0.76	48	63	84	93	94	96	96	96	95	94	97	99	99	100								
15	10.00000	19.60000	1.00	46	60	79	89	89	92	92	92	91	90	94	96	96	96	100							

REAL ARRAY SIZE USED FOR ALEX IS 1441

INTEGER ARRAY SIZE USED FOR ALEX IS 401

or

$$\Delta\sigma^2 = \Delta\sigma_{stat}^2 + \Delta\sigma_{syst}^2 \quad (6.2)$$

where the statistical uncertainty is given by (for sample-in)

$$\Delta\sigma_{stat}^2 = \sum_{\ell, \ell', j, k} \frac{\partial\sigma_{\ell}}{\partial c_j} \langle \delta c_j \delta c_k \rangle \frac{\partial\sigma_{\ell'}}{\partial c_k} \quad (6.3)$$

From Poisson statistics

$$\langle \delta c_j \delta c_k \rangle = c_j \delta_{jk} \quad (6.4)$$

and since the raw data counts are independent for each channel

$$\frac{\partial\sigma_{\ell}}{\partial c_j} = \frac{\partial\sigma_{\ell}}{\partial c_{\ell}} \delta_{j\ell} \quad (6.5)$$

so

$$\Delta\sigma_{stat}^2 = \sum_{\ell} \left(\frac{\partial\sigma_{\ell}}{\partial c_{\ell}} \right)^2 c_{\ell} \quad (6.6)$$

with a similar expression for sample-out. Similarly, for the systematic uncertainty

$$\Delta\sigma_{syst}^2 = \sum_{\ell, \ell'} \sum_{j, k=1}^{30} \frac{\partial\sigma_{\ell}}{\partial P_j} (\delta P_j \delta P_k) \frac{\partial\sigma_{\ell'}}{\partial P_k} \quad (6.7)$$

where the sum over ℓ runs over the number of channels in an energy group.

The final piece of output is the covariance matrix for the output cross sections, expressed for convenience as a correlation matrix. The standard deviations of the group cross sections are also given, expressed as percentages. We note from the previous discussion that for this example the (uncorrelated) statistical uncertainties are small, due to the large number of points included in a group. The

uncertainties are thus dominated by the parameter uncertainties; this is evident by looking at the output correlation matrix where the uncertainties at the lowest and highest energies are nearly 50% correlated with each other.

In order to more easily visualize the importance of the various parameter uncertainties, in Figs. 24 and 25 we have plotted the magnitude of the uncertainty for each of the 30 terms and counting statistics as a function of energy for this example. We see that n , m , M , and σ^2 are the major contributors.

6.2.2 Same Example as in Sect. 6.2.1, but With Diagonal Covariance Matrix for the Input Parameters

The purpose of this example is to understand the importance of the off-diagonal matrix elements for the input parameters. To study this effect, we set all off-diagonal terms in Table 7 to zero. Recall that many of these terms were evaluated by estimating the magnitude and sign of the correlation coefficient $c_{1,2}$, and are rather poorly known. Table 10 shows the resulting output correlation matrix.

Comparing these results with the output correlation matrix for the previous example, we find very little difference between the two cases. In particular, the correlations change by, at most, one unit. This result is not surprising since from Table 9 we see that the largest contributions to the uncertainties are caused by the parameters which are taken to be uncorrelated even in the correlated case, i.e., n , m , and M . Thus, we find that neglecting the off-diagonal terms for the input parameter covariance matrix is a good approximation. This conclusion should be valid for similar transmission measurements made at ORELA in which the correlated uncertainties are frequently small.

6.2.3 Example of Small Energy Intervals and Full Covariance Matrix for Input Parameters

The 15-group cross-section analysis is useful for evaluation and reactor analysis, but provides a somewhat distorted picture of the measurement since the statistical uncertainties become insignificant. As a counter-example to the previous two cases, we look at a case where we choose the energies boundaries to be ~ 1 channel wide. For convenience, the channels are taken to be those which form the energy boundaries of the previous 15-group case. The results of this example are shown in Table 11, where we display selected portions of the ALEX output, namely the part of the "contributions to uncertainties" which has the statistical uncertainties and the resulting correlation matrix.

From the "contributions to uncertainties" part, we observe that the statistical uncertainties are now much larger, as expected, and, in fact, dominate the uncertainties. This results in smaller values for entries in the correlation matrix, since the correlated uncertainties are a smaller part of the total uncertainty. We also ran this case with zero off-diagonal contributions to the input parameter covariance matrix (similar to Sect. 6.2.2), and the only change was the $c_{11,15}$ term which decreased from 10 to 9%.

6.2.4 Example of 15-Group Cross Sections With Full Parameter Matrix for Input Parameters, but Uncertainties on n , m , M , and σ^2 Decreased by 100

In Sect. 6.2.2, we found negligible effects if the off-diagonal input parameter covariance terms were set to zero. This resulted because the largest contributions to the output covariance matrix were from n , m , M , and σ^2 , and uncertainties on the first three of these are uncorrelated to other parameter uncertainties, while σ^2 is only weakly correlated. In this case and the following one, we investigate the results by reducing the uncertainties on n , m , M , and σ^2 by 100, thus making the uncertainties on the remaining input parameters proportionately more important. Table 12 gives the final output correlation matrix for this case.

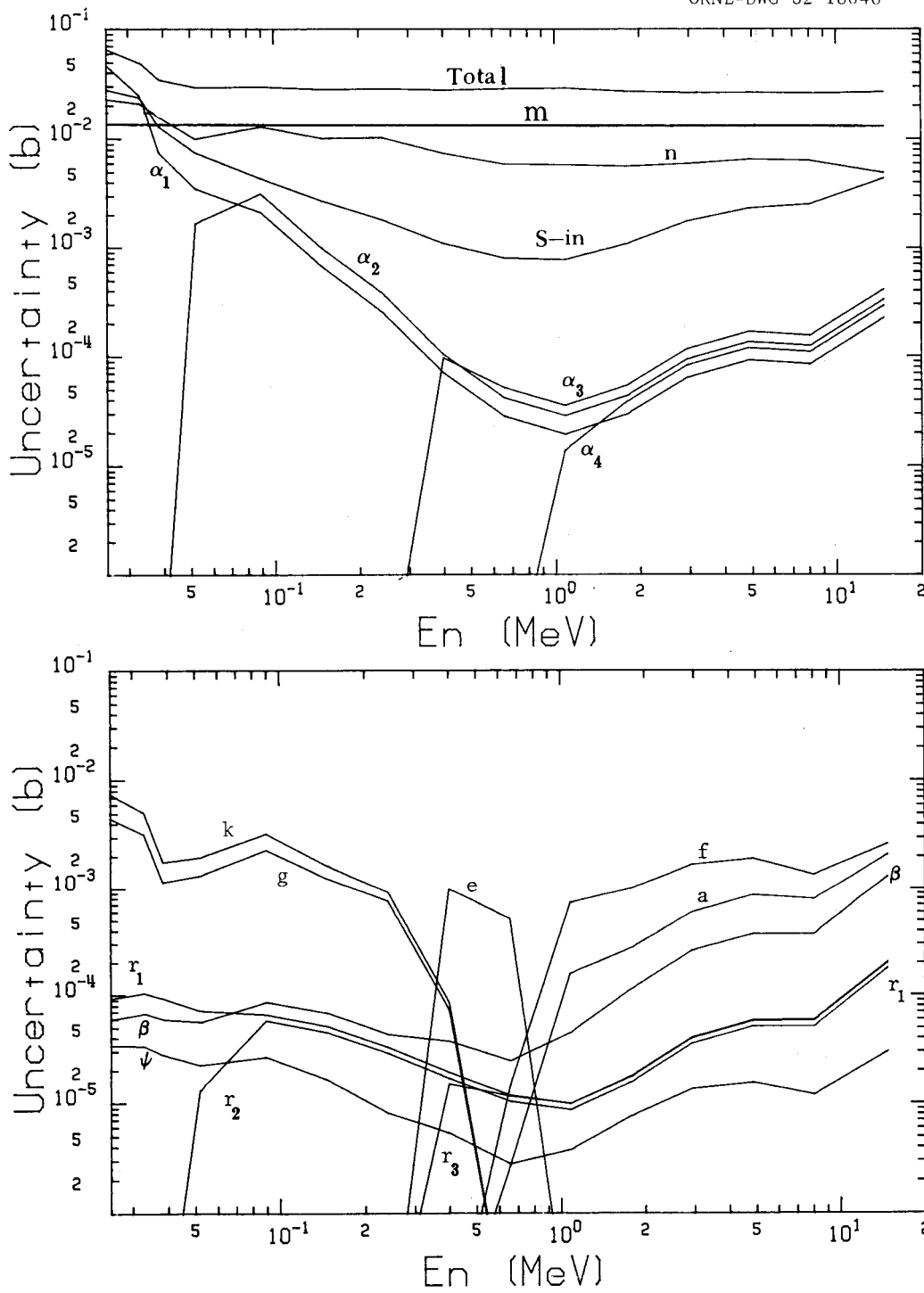


Fig. 24. The total uncertainty, expressed in barns, and the contributions of 17 of the 32 components which make up the total. S-in is the contribution of the sample-in counting statistics. This figure and Fig. 25 are for the case discussed in Sect. 6.2.1.

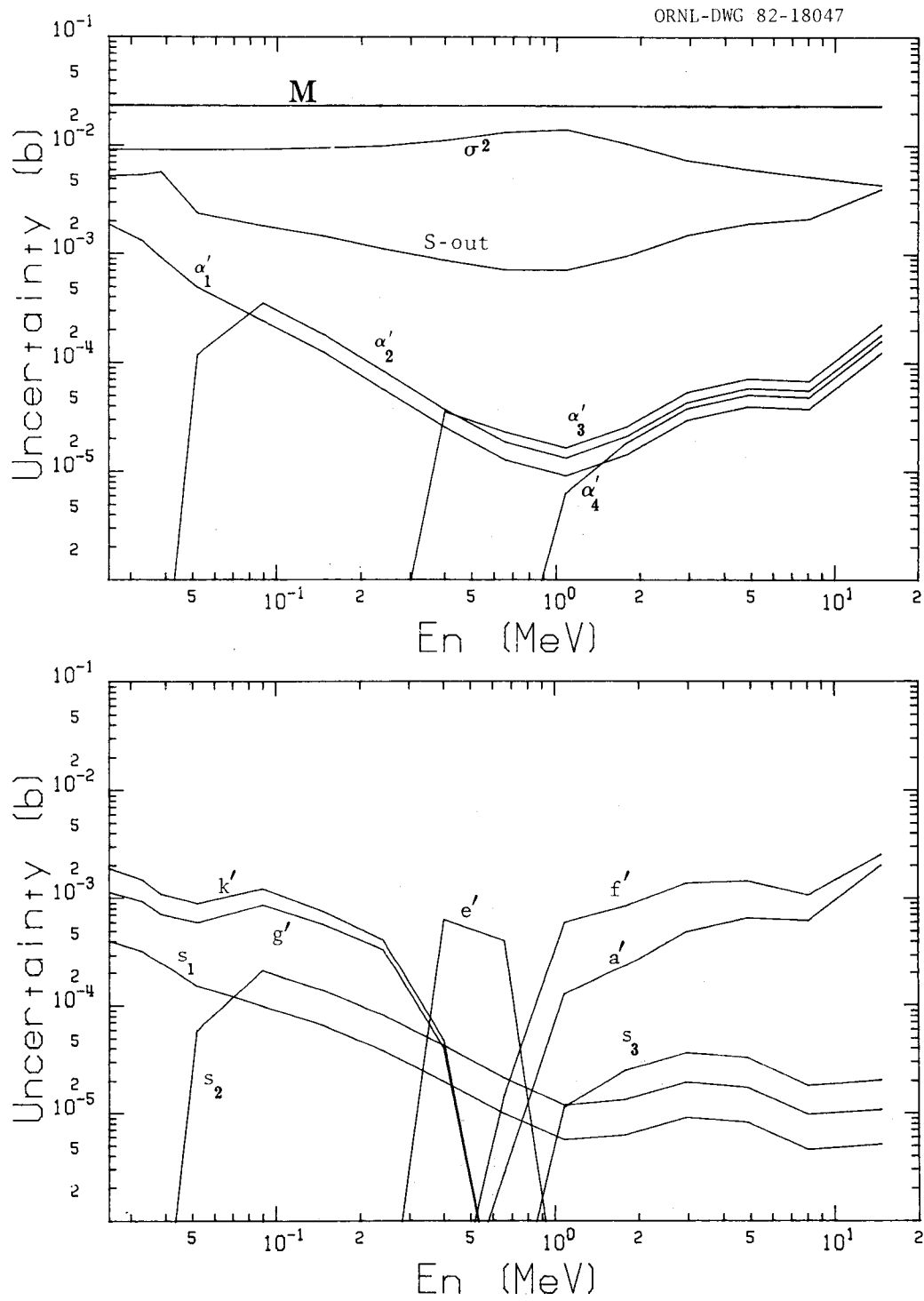


Fig. 25. Contributions of the remaining 15 contributors to the total uncertainty shown in Fig. 24. S-out is the contribution of the sample-out statistics.

Table 12. Covariance matrix for case where uncertainties on n, m, M, and σ^2 are decreased by 100

	ELOW	EHIGH	% STD.DEV.	CORRELATION															
				1	2	3	4	5	6	7	8	9	10	11	12	13	14	15	
1	0.02200	0.02800	0.44	100															
2	0.03000	0.03600	0.31		63	100													
3	0.03620	0.04090	0.22		44	43	100												
4	0.04090	0.06300	0.24		37	40	51	100											
5	0.06740	0.11100	0.17		33	38	53	74	100										
6	0.11100	0.18300	0.19		25	33	53	75	86	100									
7	0.18300	0.30200	0.19		22	30	53	75	85	94	100								
8	0.30200	0.49800	0.30		20	29	53	75	85	94	97	100							
9	0.49800	0.82100	0.44		20	29	53	75	84	95	98	99	100						
10	0.82100	1.35000	0.48		20	29	53	75	84	95	98	99	100						
11	1.35000	2.23000	0.36		20	29	53	75	84	94	97	98	99	100					
12	2.23000	3.68000	0.26		19	28	50	71	80	88	90	92	93	94	100				
13	3.68000	6.06000	0.21		19	26	46	65	74	82	83	86	85	88	88	100			
14	6.06000	10.00000	0.19		18	25	44	63	71	78	80	82	82	83	84	81	100		
15	10.00000	19.60000	0.34		14	18	29	41	48	50	51	53	52	53	56	63	64	60	100

Here we find that the correlations are smaller, since we have reduced the effects of the four major contributors (and thereby enhanced the uncorrelated statistical contribution) which are fully correlated over the full-energy range. This is especially evident for the block of the correlation matrix which corresponds to the long-range correlations. We also note that the percent standard deviation on each group is smaller, as expected, since the major contributors were decreased.

6.2.5 *Same Example as Previous Case, Except a Diagonal Covariance Matrix was Used for the Input Parameters*

Table 13 shows the final covariance matrix which results from dropping the off-diagonal terms for the input parameters. Looking at Table 13 we see that the effects of dropping the off-diagonal elements of the input covariance matrix are much more significant than for case 6.2.2; i.e., the long-range correlations are much smaller. Two groups of correlated data are now evident; the data from 0.022 to 0.302 MeV are correlated as are the data from 1.35 to 19.6 MeV, with very little correlation between the two groups.

6.2.6 *Uncertainty Analysis for the Averaged Data*

In Sect. 4.3, we described the selective averaging of our data, reducing the number of points from 60,000 to 13,696 (appropriate for a resonance parameter analysis) and covering the energy range from 2 keV to 20 MeV. A covariance matrix is not provided for this averaged data set, but in Fig. 26 we plot the systematic, statistical, and total uncertainties expressed as a percentage of the total cross section. The uncertainties are derived from Eqs. (6.3) and (6.4). Averaged over the complete energy range, the statistical uncertainty is ~ 2.5 times larger than the systematic uncertainty.

6.2.7 *Conclusions from Uncertainty Analysis Results*

Inspection of the results from the previous examples leads to some conclusions regarding future uncertainty analyses for similar measurements. First, since uncertainties on n , m , M , and σ^2 probably cannot be reduced by 100 (or even 10) experimentally, these will remain the largest sources of uncertainty. This implies that the off-diagonal elements of the input parameter covariance can be neglected, and only the diagonal terms need be dealt with. We also note that, for unaveraged (or moderately averaged) data, the statistical uncertainties are the most important, so running the measurement longer may be cost effective if high accuracy results are required.

We also note from the final output covariance matrix for the various examples that the total uncertainty is small, perhaps smaller than one would have expected prior to the detailed uncertainty analysis presented here. The systematic uncertainties are dominant for the full 15-group case in Sect. 6.2.1, where from Eq. (6.2) we find for group 7, for example, $\Delta\sigma_T = 0.029$, $\Delta\sigma_{stat} = 0.002$, and $\Delta\sigma_{syst} = 0.029$. For the case described in Sect. 6.2.3, where the group contained only one channel, the statistical uncertainties are dominant; for group 7 we find $\Delta\sigma_T = 0.135$, $\Delta\sigma_{stat} = 0.132$ and $\Delta\sigma_{syst} = 0.027$. However, the example in Sect. 6.2.6 where we averaged the data in a realistic manner shows that, in general, both the statistical and systematic uncertainties are important and must be reported.

Table 13. Final covariance matrix for diagonal input covariance matrix

ELOW	EHIGH	% STD.DEV.	CORRELATION														
			1	2	3	4	5	6	7	8	9	10	11	12	13	14	15
1	0.02200	0.02800	100														
2	0.03000	0.03600	64	100													
3	0.03620	0.04090	44	43	100												
4	0.04090	0.06300	38	41	51	100											
5	0.06740	0.11100	34	39	53	74	100										
6	0.11100	0.18300	25	33	54	76	86	100									
7	0.18300	0.30200	21	30	53	75	84	94	100								
8	0.30200	0.49800	18	28	52	74	80	93	96	100							
9	0.49800	0.82100	18	27	52	74	80	93	97	99	100						
10	0.82100	1.35000	18	27	52	74	80	93	97	98	99	100					
11	1.35000	2.23000	18	27	52	73	80	92	96	97	98	99	100				
12	2.23000	3.68000	17	26	49	69	75	86	90	91	92	94	94	100			
13	3.68000	6.06000	16	24	45	64	70	80	83	84	85	87	88	88	100		
14	6.06000	10.00000	16	23	43	61	67	77	80	81	82	83	84	84	80	100	
15	10.00000	19.60000	11	16	28	40	44	49	51	52	52	55	57	62	63	59	100

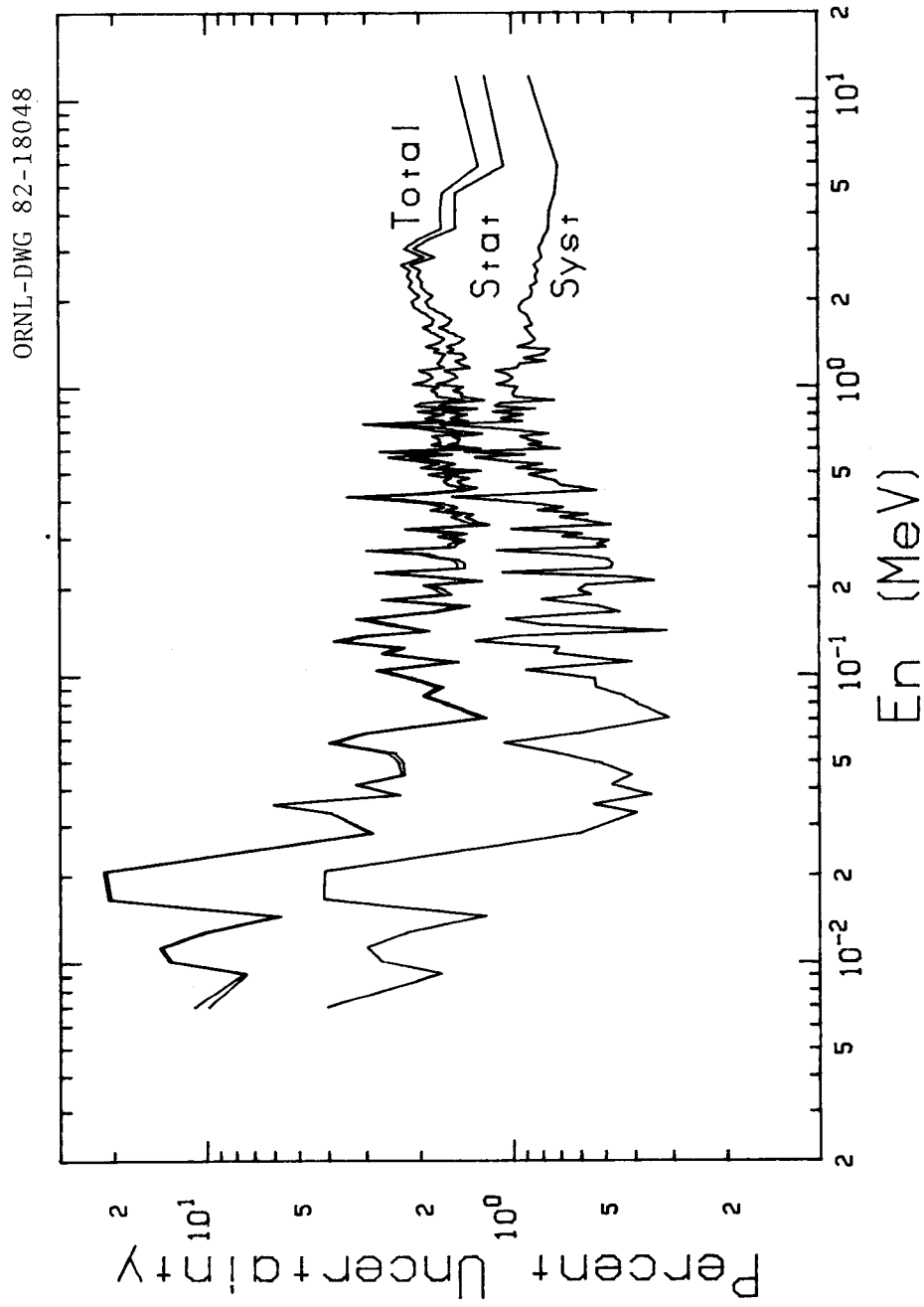


Fig. 26. The systematic (lowest curve), statistical (middle), and total (upper) uncertainties for the averaged nickel data are shown. The results are expressed as percentages ($\Delta\sigma/\sigma \times 100$), and have been averaged by 100 to reduce the scatter below ~ 50 keV.

7. SUMMARY AND CONCLUSIONS

In this report we have described our nickel transmission measurements. As a result of this attempt to measure neutron transmission down to a few keV with a NE110 plastic scintillator, new data acquisition schemes have been developed and tested. These tests demonstrated that a background source not observed in past measurements now must be dealt with; this source is phototube afterpulsing. In order to reduce the lower limit where useful data were obtained in the past from ~ 20 keV down to ~ 2 keV, we had to modify our data-taking scheme from a traditional multistop-per-start mode, which produced 2.5 to 3 counts per burst, to a gated multistop which gives 1.5 to 2 counts per burst. This was done by determining time and pulse-height properties of the detected event and deciding then whether to choose a multistop or single stop-per-start data acquisition scheme. The cost of pushing the lower energy limit for useful data down from 20 to ~ 2 keV has been a decreased counting rate, larger deadtimes (and increased sensitivity to neutron intensity variations), and more complicated electronics in the data acquisition system.

This new data acquisition scheme required modifications to our deadtime correction program, since some data were taken as single stop-per-start, while other data were taken in the multistop-per-start mode. In addition, the variance of the intensity variation was included explicitly and is the only uncertainty associated with the deadtime correction. This correction to the data was the largest correction made and, thus, the most important.

A detailed discussion of the known backgrounds, their sources as well as their removal, was given. The data-taking scheme utilizing four bias levels provided crude pulse-height information which was used to isolate sources of backgrounds. The time-dependent backgrounds were then extracted from the bias where they were the largest, renormalized to other biases based on ratios obtained in separate experiments, and subtracted. Figure 9 shows the backgrounds are small, typically less than 1% (except at the resonances).

An uncertainty analysis was then performed for this measurement, accounting for all known significant sources of possible error in the measurement. Explicit expressions for the uncertainty in the deadtime and background corrections were derived, and correlations were estimated among the terms. A covariance matrix and associated correlation matrix were derived, along with standard deviations for each energy point. Since there were initially 60,000 data points, the cross sections were averaged into 15 groups, and the 15 energies and cross sections were given along with the 15×15 correlation matrix and standard deviations for each group.

One point which remains to be settled is the disagreement of our hydrogen measurement with the evaluated cross section. Our measurement goes systematically from $\sim 1\%$ low at 50 keV to 1.5% high at 1 MeV, and then remains $\sim 1.5\%$ high to 20 MeV. The problem appears to be associated with our efforts to detect low-energy neutrons and corresponding low-light levels, since similar data taken with much higher discriminator levels are in $\sim 0.5\%$ agreement with the hydrogen cross section. This also leads to an apparent inconsistency in that we quote uncertainties of $\sim 1\%$ for the 15-group nickel results, but disagree by larger amounts with the standard hydrogen cross section. Work is continuing in an attempt to understand this difficulty, but it is not apparent to us that the problem is necessarily present for the nickel data.

Results of this work which will impact future measurements include (a) rerunning the polyethylene-carbon matched sets together with an open-beam measurement so the carbon cross section can be

extracted and checked, (b) readjusting the bias levels 3 and 4 to achieve better separation of the background components [i.e., $^{10}\text{B}(n,\alpha\gamma)$ in bias 3, $\text{H}(n,\gamma)$ in bias 4], (c) improved monitoring of the variation in beam power intensity which is needed to evaluate the deadtime uncertainty, and (d) development of a better beam monitor system.

The nickel cross-section data, selectively averaged to 13,696 channels, and the corresponding total uncertainties shown in Fig. 26, have been sent to the National Nuclear Data Center at Brookhaven National Laboratory. If a covariance matrix for the nickel data is desired in some energy grouping other than reported in this paper, it can be obtained by contacting the authors.

ACKNOWLEDGEMENTS

The authors wish to thank the ORELA operating crew for careful operation of the accelerator and monitoring of the beam power variations. We also wish to thank J. G. Craven for providing modifications to the deadtime correction program used in this work, and J. H. Marable for useful discussions involving the deadtime corrections. Finally, we wish to thank Bob Peelle and Francis Perey for useful discussions regarding the uncertainty analysis section of this report, and Sue Damewood for a careful and expert job of typing this report.

REFERENCES

- AR79 R. A. Arndt, Virginia Polytechnic Institute, December 1979, Solution Set CD79.
- CR81 J. G. Craven, Program DTCDCL, unpublished 1981.
- DI79 M. Divadeenam, *Ni Elemental Neutron Induced Reaction Cross-Section Evaluation*, Report BNL-NCS-51346, ENDF-294, March 1979.
- FA66 J. A. Farrell, E. G. Bilpuch and H. W. Newson, *Ann. Phys.*, **37**, 367 (1966).
- GA71 J. B. Garg, J. Rainwater and W. W. Havens, Jr. *Phys. Rev. C***3**, 2447 (1971).
- HA77 J. A. Harvey, private communication, 1977.
- HA79 J. A. Harvey and N. W. Hill, *Nucl. Inst. Meth.* **162**, 507 (1979).
- KI72 W. E. Kinney, private communication, 1972.
- LA76 D. C. Larson, C. H. Johnson, J. A. Harvey, and N. W. Hill, *Measurement of the Neutron Total Cross Section of Fluorine from 5 eV to 20 MeV*, ORNL/TM-5612, Oak Ridge National Laboratory, Oak Ridge, Tenn., October 1976.

- LA80 D. C. Larson, "ORELA Measurements to Meet Fusion Energy Neutron Cross Section Needs," in *Symposium on Neutron Cross-Sections from 10 to 50 MeV*, Report BNL-NCS-51245, Vol. 1, July 1980.
- LA80a N. M. Larson and F. G. Perey, *User's Guide for SAMMY: A Computer Model for Multilevel R-Matrix Fits to Neutron Data Using Bayes' Equations*, ORNL/TM-7485, ENDF-297, Oak Ridge National Laboratory, Oak Ridge, Tenn., November 1980.
- LA83 D. C. Larson, N. M. Larson, and J. A. Harvey, *Determination of the Energy Dependence of the Length, Experimental Energies, and Energy Resolution Function, and their Uncertainties for Flight Path 1 at ORELA*, ORNL/TM-8880, Oak Ridge National Laboratory, Oak Ridge, Tenn., September 1983.
- LA83a N. M. Larson, *User's Guide for ALEX: Uncertainty Propagation from Raw Data to Final Results for ORELA Transmission Measurements*, ORNL/TM-8676, Oak Ridge National Laboratory, Oak Ridge, Tenn., in preparation.
- MA76 R. E. Maerker, C. E. Clifford, and F. J. Muckenthaler, *Neutron Total Cross Section Checks for Iron, Chromium, Nickel, Stainless Steel, Sodium, and Carbon*, ORNL-5013, Oak Ridge National Laboratory, Oak Ridge, Tenn., April 1976.
- MA80 J. H. Marable, C. R. Weisbin, and G. de Saussure, "Uncertainty in the Breeding Ratio of a Large Liquid-Metal Fast Breeder Reactor: Theory and Results," *Nucl. Sci. Eng.* **75**, 30 (1980).
- MO80 M. S. Moore, "Rate Dependence of Counting Losses in Neutron Time-of-Flight Measurements," *Nucl. Inst. Meth.* **169**, 245 (1980).
- OL76 D. K. Olsen, G. de Saussure, R. B. Perez, E. G. Silver, R. W. Ingle, and H. Weaver, *Measurement of Neutron Transmissions from 0.52 eV to 4.0 keV Through Seven Samples of ^{238}U at 40 m.*, ORNL/TM-5256, Oak Ridge National Laboratory, Oak Ridge, Tenn., March 1976.
- PE73 F. G. Perey, T. A. Love, and W. E. Kinney, *A Test of Neutron Total Cross-Section Evaluations from 0.2 to 20 MeV for C, O, Al, Si, Ca, Fe, and SiO_2* , ORNL-4823, ENDF-178, Oak Ridge National Laboratory, Oak Ridge, Tenn., December 1972. Also private communication from F. G. Perey to the National Nuclear Data Center, 1974.
- PE82 C. M. Perey, J. A. Harvey, R. L. Macklin, and F. G. Perey, *Neutron Transmission and Capture Measurements and Analysis of ^{60}Ni from 1 to 450 keV*, ORNL-5893, ENDF-330, Oak Ridge National Laboratory, Oak Ridge, Tenn., November 1982.
- PE83 F. G. Perey, private communication based on preliminary data for the 1.15 keV resonance in the $n + ^{56}\text{Fe}$ reaction.
- RE78 C. Renner, N. W. Hill, G. L. Morgan, K. Rush, and J. A. Harvey, *Nucl. Inst. Meth.* **154**, 525 (1978).

- SC74 R. B. Schwartz, R. A. Schrack and H. T. Heaton II, *MeV Total Neutron Cross Sections*, National Bureau Standards Monograph 138, January 1974.
- ST70 E. Storm and H. I. Israel, "Photon Cross Sections from 1 keV to 100 MeV for Elements $Z=1$ to $Z=100$," *Nucl. Data Tables* 7, 565 (1970).
- ST71 R. G. Stieglitz, R. W. Hockenbury, and R. C. Block, *Nucl. Phys.*, **A163**, 592 (1971).
- ST73 R. G. Stieglitz, J. T. Reynolds, C. J. Slavik, and C. R. Lubitz, *Evaluated Neutron Cross Sections for Chromium (version 8), Iron (versions 13 and 19), and Nickel (version 8)*, Knolls Atomic Power Laboratory Report KAPL-M-7156 (BOB-1), March 1973.
- ST79 L. Stewart, R. J. LaBauve and P. G. Young, *ENDF/B Data File for H(MAT 1301, MOD 1) Evaluation*, Los Alamos Reports LA-4574 (1971) and LA-6518-MS (1976).
- SY82 D. B. Syme, *Nucl. Inst. Meth.*, **198**, 357 (1982).
- TE68 R. E. Textor and V. V. Verbinski, *O5S: A Monte Carlo for Calculating Pulse Height Distributions Due to Monoenergetic Neutrons Incident on Organic Scintillators*, ORNL-4160, Oak Ridge National Laboratory, Oak Ridge, Tenn., 1968.
- WE82 C. R. Weisbin, R. D. McKnight, J. D. Hardy, Jr., R. W. Roussin, R. E. Schenter, and B. Magurno, *Benchmark Testing of ENDF/B-V*, ENDF-311 (August 1982).

APPENDIX A. EFFECTS OF NEUTRON INTENSITY VARIATION ON THE DEADTIME CORRECTION

In this appendix are derived the general formulas for the deadtime correction for the multiple stopper-start mode, in the case where the intensity but not the shape of the incident neutron flux varies from pulse to pulse. We begin by considering the number of counts registered by the detector at time t due to a single pulse. Although experiments necessarily involve only discrete time intervals, it is nevertheless expedient to first consider continuous times in order to correctly describe deadtime effects. Eventually we shall integrate over channel width and sum over the number of pulses in order to obtain the quantity which is needed for the deadtime correction.

Consider first the n^{th} pulse out of a total of N (where $N \sim 10^8$ for a typical ORELA experiment). Let $X_n(t)dt$ represent the number of counts registered by the detector during infinitesimal time interval dt at time t . Since the time digitizer is "dead" (i.e., unreceptive to additional signals) for time D following reception of a signal, it follows that the the integral of $X_n(t)$ over a time interval of length D at any time will be either 0 or 1. It also follows that

$$X_n(t) \propto 1 - \int_{t-D}^t X_n(\tau) d\tau \quad , \quad (\text{A.1})$$

i.e., a count cannot be registered at time t if the detector is dead at time t .

Let $Z_n(t)$ represent the number of neutrons which would have been registered by the detector at time t for the n^{th} pulse, if the deadtime D were zero. [For example, if deadtime D were zero, $Z_n(t)$ would exactly equal $X_n(t)$.] This quantity $Z_n(t)$ is the product of two terms:

(1) The flux $\Phi_n(t')$, where t' is the time at which the neutron leaves the source. If T_p represents the pulse width ($T_p \sim 7$ nsec for the present measurement), then t' ranges from 0 to T_p (see Fig. A-1).

(2) The "system response" $R(t-t')$ where $t-t'$ is the time required for a neutron to travel from source to detector, leaving the source at time t' and arriving at the detector at time t (see Fig. A-1). This system response is in fact the physics which the experimenter is hoping to measure; e.g., in a transmission experiment $R(t-t')$ is the transmission through the sample for a neutron of energy $E \propto (t-t')^{-2}$.

Multiplying flux by response and integrating over pulse width give

$$Z_n(t) = \int_0^{T_p} \Phi_n(t') R(t-t') dt' \quad (\text{A.2})$$

for the number of neutrons available to be counted.

The usual assumption made at this point in the derivation of the deadtime correction is that the flux $\Phi_n(t')$ does not vary from pulse to pulse, i.e., that Φ_n is independent of n . We choose instead to make a less restrictive assumption, that only the *shape* of the spectrum of neutrons is invariant but the magnitude may change from one pulse to the next. That is, we set

ORNL-DWG 82-17091

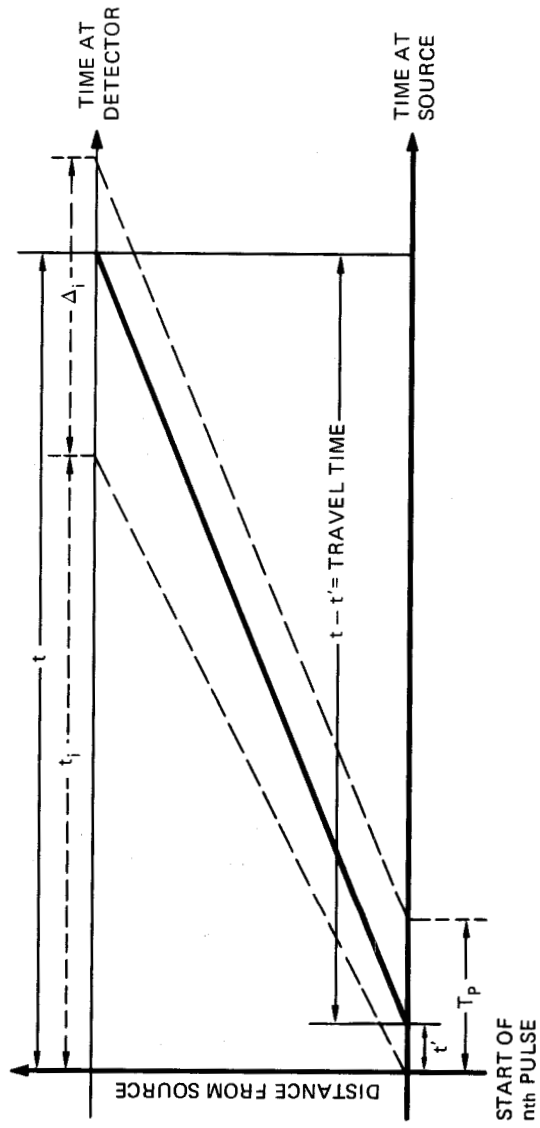


Fig. A-1. Schematic showing the times defined in the text for a neutron which leaves the source at time t' ($0 \leq t' \leq T_p$) and arrives at the detector at time t within channel i ($t_i \leq t \leq t_i + \Delta_i = t_{i+1}$).

$$\Phi_n(t') = F_n \bar{\Phi}(t') \quad (\text{A.3})$$

where F_n is a random number which, when averaged over all n (i.e., over all pulses), is unity. Later we shall make specific assumptions regarding the distribution of F_n .

Substituting Eq. (A.3) into Eq. (A.2) allows us to write $Z_n(t)$ in the form

$$Z_n(t) = F_n Y(t) \quad (\text{A.4})$$

where

$$Y(t) = \int_0^{T_p} \bar{\Phi}(t') R(t-t') dt' \quad (\text{A.5})$$

where $Y(t)$ is independent of n . Since $Z_n(t)$ represents the number of counts available to be detected, and $X_n(t)$ is the number of counts actually detected, the two may be related via the deadtime factor given in Eq. (A.1):

$$X_n(t) = \left[1 - \int_{t-D}^t X_n(\tau) d\tau \right] F_n Y(t) \quad (\text{A.6})$$

where we have used Eq. (A.4) for Z_n .

To obtain an expression which corresponds to the raw data measured in an experiment, $X_n(t)$ must be integrated over channel width and summed over pulses. That is, the total number of counts C_i which the detector registers for channel i is given by

$$C_i = \sum_{n=1}^N \int_{t_i}^{t_i+\Delta_i} X_n(t) dt \quad (\text{A.7})$$

Similarly, the total number of counts C'_i which the detector would have registered for channel i if deadtime were zero is given by

$$C'_i = \sum_{n=1}^N F_n \int_{t_i}^{t_i+\Delta_i} Y(t) dt \quad (\text{A.8})$$

Since C'_i is the quantity which the experimenter would measure if he could, our goal is now to obtain a relationship for C'_i in terms of C_i .

We start with Eq. (A.6), sum over pulses n , and rearrange:

$$Y(t) = \frac{\sum_{n=1}^N X_n(t)}{\sum_{n=1}^N F_n - \sum_{n=1}^N F_n \int_{t-D}^t X_n(\tau) d\tau} \quad (\text{A.9})$$

Substituting this expression for $Y(t)$ into Eq. (A.8) gives, after some manipulation,

$$C'_i = \int_{t_i}^{t_i+\Delta_i} dt \frac{\sum_{n=1}^N X_n(t)}{1 - \frac{\sum_{n=1}^N F_n \int_{t-D}^t X_n(\tau) d\tau}{\sum_{n=1}^N F_n}} \quad (\text{A.10})$$

This is an exact equation for C'_i , subject to only one challengeable assumption (that being that the shape of the flux is the same for all pulses). It is, however, not a particularly useful equation since it is in terms of $X_n(t)$ rather than in terms of measurable quantities C_i . To remedy this shortcoming, it is necessary to make additional assumptions and approximations.

Assumption. The flux intensities F_n average to 1 with variance σ^2 . Moreover, this variance is known only to within $\Delta\sigma^2$. Translating these words to equations, we have

$$\sum_{n=1}^N F_n = N \quad (\text{A.11})$$

and

$$\frac{1}{N} \sum_{n=1}^N (F_n - 1)^2 = \sigma^2 \quad (\text{within } \Delta\sigma^2) \quad (\text{A.12})$$

Further, assuming the distribution is symmetric around 1 gives

$$\sum_{n=1}^N (F_n - 1)^3 = 0 \quad . \quad (\text{A.13})$$

Approximation: The second term in the denominator of Eq. (A.10) can be evaluated by considering the iterated form of Eq. (A.6):

$$X_n(t) = F_n Y(t) - F_n^2 Y(t) \int_{t-D}^t Y(\tau) d\tau + F_n^3 Y(t) \int_{t-D}^t Y(\tau) d\tau \int_{\tau-D}^{\tau} Y(\tau') d\tau' + \dots \quad (\text{A.14})$$

Summing over n and dropping all but the first two terms give

$$\sum_n X_n(t) \approx Y(t) \left\{ \sum_{n=1}^N F_n - \sum_{n=1}^N F_n^2 \int_{t-D}^t Y(\tau) d\tau \right\} \quad (\text{A.15})$$

and

$$\sum_n F_n X_n(t) \approx Y(t) \left\{ \sum_{n=1}^N F_n^2 - \sum_{n=1}^N F_n^3 \int_{t-D}^t Y(\tau) d\tau \right\} \quad (\text{A.16})$$

These approximations are justified by noting that, at a typical ORELA count rate of three counts per burst, the value of $\int_{t-D}^t Y(\tau) d\tau$ is $\sim 3D/T$ where T is the time between bursts. For $D \sim 1100$ nsec, $T \sim 1200$ μ sec, the value of that integral is 3×10^{-3} . Terms of this order will be neglected.

Substituting Eqs. (A.11) to (A.13) into Eqs. (A.15) and (A.16), and letting I represent the integral in these equations, give

$$\sum_n X_n(t) \approx Y(t) \{N - N(1 + \sigma^2)I\} \quad (\text{A.17})$$

and

$$\sum_n F_n X_n(t) \approx Y(t) \{N(1+\sigma^2) - N(1+3\sigma^2)I\} \quad (\text{A.18})$$

The largest value of σ^2 obtained to date at ORELA is <0.05 ; it is therefore legitimate to drop terms $\sim \sigma^2 I$. Solving Eq. (A.17) for Y , substituting into Eq. (A.18), and dropping terms on the order of $\sigma^2 I$ or smaller, give

$$\sum_n F_n X_n(t) \approx [(1 + \sigma^2) - (1 + 3\sigma^2)I + (1 + \sigma^2)^2 I] \sum_n X_n(t) \quad (\text{A.19})$$

or

$$\sum_n F_n X_n(t) \approx (1 + \sigma^2) \sum_n X_n(t) \quad (\text{A.20})$$

Equations (A.20) and (A.11) are used to rewrite Eq. (A.10) into the form

$$C'_i = \int_{t_i}^{t_i+\Delta_i} dt \frac{c(t)}{1 - \frac{(1+\sigma^2)}{N} \int_{t-D}^t c(\tau) d\tau} \quad (\text{A.21})$$

where we have introduced the notation

$$c(t) = \sum_n X_n(t) \quad (\text{A.22})$$

so that the experimentally measured raw data corresponds to

$$C_i = \int_{t_i}^{t_i+\Delta_i} c(t) dt \quad (\text{A.23})$$

Further simplification of Eq. (A.21) requires additional approximations for the integration limits in the denominator. Let i_1 represent that channel for which

$$t_i \leq t_i - D < t_{i+1} \quad (\text{A.24})$$

and i_2 represent that channel for which

$$t_{i-1} < t_i + \Delta_i - D \leq t_{i_2} \quad (\text{A.25})$$

Figure A-2 illustrates these relationships. Note that it is possible, but not necessary, that $i_1 = i_2 - 1$.

The integral in the denominator of Eq. (A.21) may then be broken into pieces as

$$\int_{t-D}^t c(\tau) d\tau = \int_{t_i}^t c(\tau) d\tau + \sum_{j=i_2}^{i-1} C_j + \int_{t-D}^{t_{i_2}} c(\tau) d\tau \quad (\text{A.26})$$

Normally the third term is approximated by setting the lower limit $t-D$ equal to a channel boundary t_{i_3} , where i_3 is in the range $i_1 \leq i_3 \leq i_2$. This term can then be combined with the second term, yielding

$$\int_{t-D}^t c(\tau) d\tau = \int_{t_i}^t c(\tau) d\tau + \sum_{j=i_3}^{i-1} C_j \quad (\text{A.27})$$

The work reported in this paper uses this approximation. An alternative is discussed at the end of this appendix.

Two methods have been used to treat the first term in Eq. (A.27). The first is to treat it exactly. In that case the integrand in Eq. (A.21) is a logarithmic derivative; the integral is

$$C'_i = - \frac{N}{1 + \sigma^2} \ln \left[1 - \frac{C_i}{\frac{N}{1 + \sigma^2} - \sum_{j=i_3}^{i-1} C_j} \right] \quad (\text{A.28})$$

This is the form reported by M. S. Moore (MO80) in his Eq. (2), with $\sigma^2 = 0$. In the appropriate limit (σ^2 small), Eq. (A.28) also agrees with Moore's Eq. (10) for deadtime correction including variation in flux intensity; however, our preference is for the form in our Eq. (A.28), it being the more rigorously derived version.

ORNL-DWG 82-17090

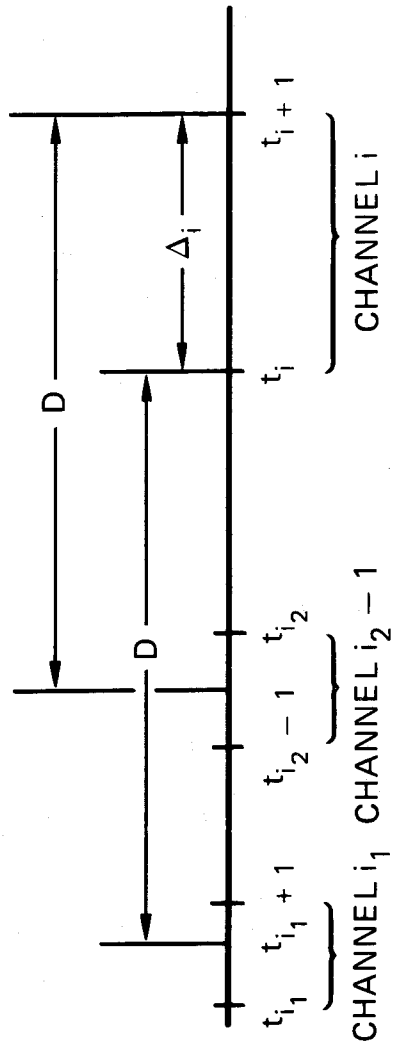


Fig. A-2. Schematic of the channel times entering into the integration limits for the denominator in Eq. (A-21).

The second method is to treat the first term in Eq. (A.27) as a constant, equal to $\frac{1}{2}C_i$. In this case, Eq. (A.21) becomes

$$C'_i \simeq \frac{C_i}{1 - \frac{1 + \sigma^2}{N} \left[\sum_{j=i_1}^{i_2-1} C_j + \frac{1}{2} C_i \right]} \quad (\text{A.29})$$

This is the form of the deadtime correction used in this work. It is clear from Eq. (A.29) that variation in flux intensity produces an increase in the deadtime correction.

Finally, let us consider an alternative approximation for the third term in Eq. (A.26) (MA82). Note that this term may be written as

$$\int_{t-D}^{t_2} c(\tau) d\tau = \int_{t_1}^{t_2} c(\tau) d\tau - \int_{t_1}^{t-D} c(\tau) d\tau \quad (\text{A.30})$$

which is equal to

$$\sum_{j=i_1}^{i_2-1} C_j - \int_{t_1+D}^t c(\tau-D) d\tau \quad (\text{A.31})$$

The lower limit $t_1 + D$ is $\approx t_1$ and will be set equal to t_1 . We now assume that $c(\tau-D)$ has the same shape but perhaps different magnitude as $c(\tau)$ in the range from t_1 to t . This is usually reasonable, since over a channel width there should be little structure in the counting rates. Explicitly, our assumption is that

$$c(\tau - D) \approx \alpha c(\tau) \quad (\text{A.32})$$

and the magnitude of α may be estimated as

$$\alpha \approx \sum_{j=i_1}^{i_2-1} C_j / C_i \quad (\text{A.33})$$

With this assumption, Eq. (A.26) becomes

$$\int_{t-D}^t c(\tau)d\tau \approx (1 - \alpha) \int_{t_i}^t c(\tau)d\tau + \sum_{j=i_1}^{i-1} C_j \quad (\text{A.34})$$

When Eq. (A.34) is substituted into the denominator of Eq. (A.21), the integral may be evaluated directly to yield

$$C'_i \approx - \frac{N}{1 + \sigma^2} \frac{C_i}{C_i - \sum_{j=i_1}^{i_2-1} C_j} \ln \left[1 - \frac{C_i - \sum_{j=i_1}^{i_2-1} C_j}{\frac{N}{1+\sigma^2} - \sum_{j=i_1}^{i-1} C_j} \right] \quad (\text{A.35})$$

Equation (A.35) is the least-restrictive form of the deadtime correction; i.e., it involves the fewest approximations and limiting assumptions.

Finally, if the $\int_{t_i}^t c(\tau)d\tau$ is again treated as a constant, equal to $\frac{1}{2}C_i$, we obtain the form analogous to Eq. (A.29):

$$C'_i \approx \frac{C_i}{1 - \frac{1+\sigma^2}{N} \left[\sum_{j=i_2}^{i_1} C_j + \frac{1}{2} \sum_{j=i_1}^{i_2-1} C_j + \frac{1}{2} C_i \right]} \quad (\text{A.36})$$

This form is possibly easier to manipulate than Eq. (A.35), yet may for some experiments offer significant improvement over the version currently in use at ORELA [Eq. (A.29)].

APPENDIX B. METHOD OF ESTIMATING $(1 + \sigma^2)$

Our description of the deadtime correction (see Appendix A) requires knowledge of the value of σ^2 , which we defined as the variance of the distribution describing the combined intensity variations due both to pulse-to-pulse variations and long-term drifts. Because σ^2 was not measured directly in this experiment, it is necessary to estimate σ^2 based on the information which is available. Two types of information are available: short-term (pulse-to-pulse) variation in intensity (as measured over a time period of a few seconds), and the monitor and trigger counts for each of the ~ 10 -minute cycles for a given run. In this Appendix, we describe a method whereby these two pieces of information may be used to estimate σ^2 , and is valid for the case where the power variation between cycles is less than 20-30%.

We begin by modifying the notation somewhat from that used in Appendix A. Let F_{jk} represent the magnitude of the neutron flux for the j^{th} pulse within the k^{th} 10-minute cycle. That is, F_{jk} is exactly equal to F_n defined in Eq. (A.3), if n is set equal to

$$n = \sum_{k'=1}^{k-1} T_{k'} + j \quad (\text{B.1})$$

where $T_{k'}$ is the number of triggers in the k'^{th} cycle. By direct comparison with Eq. (A.11), we see that

$$\sum_{k=1}^K \sum_{j=1}^{T_k} F_{jk} = T \quad (\text{B.2})$$

where K is the total number of cycles for the run and where

$$T = \sum_{k=1}^K T_k \quad (\text{B.3})$$

is the total number of triggers for the run. Similarly, Eq. (A.12) becomes

$$\frac{1}{T} \sum_{k=1}^K \sum_{j=1}^{T_k} (F_{jk} - 1)^2 = \sigma^2 \quad (\text{B.4})$$

or, using Eqs. (B.2) and (B.3), we can write this as

$$\frac{1}{T} \sum_{k=1}^K \sum_{j=1}^{T_k} F_{jk}^2 = 1 + \sigma^2 \quad (\text{B.5})$$

Our goal is to evaluate $1 + \sigma^2$ by estimating values for the summations on the left-hand side of Eq. (B.5).

Recall from Eq. (A.3) that the flux for the j^{th} pulse in the k^{th} cycle is given by $F_{jk}\Phi(t')$. Let m_{jk} represent the (deadtime corrected) monitor counts; m_{jk} is directly proportional to the integrated flux. Thus, we may write

$$m_{jk} = F_{jk}I \quad (\text{B.6})$$

where I is a constant. To determine the value of I , define m_k as the monitor counts for cycle k , that is,

$$m_k = \sum_{j=1}^{T_k} m_{jk} \quad (\text{B.7})$$

and the value of m_k is a known quantity. We also define m to be the total monitor counts for all cycles (i.e., for a run)

$$m = \sum_{k=1}^K m_k = \sum_{k=1}^K \sum_{j=1}^{T_k} m_{jk} \quad (\text{B.8})$$

Since the m_k are known, m is also known. If we sum Eq. (B.6) over both j and k , and compare with Eqs. (B.2) and (B.8), we find

$$m = TI$$

or

$$I = \frac{m}{T}$$

so that m_{jk} is related to F_{jk} via

$$m_{jk} = \frac{m}{T} F_{jk} \quad . \quad (\text{B.9})$$

The short-term (pulse-to-pulse) information available for this experiment consists of the frequency distribution of m_{jk} for a small number of triggers, say n , where $n \ll T_k$. The mean and variance of this distribution may be calculated as

$$\frac{1}{n} \sum_{j=1}^n m_{jk} = \mu_k \quad (\text{B.10})$$

and

$$\frac{1}{n} \sum_{j=1}^n (m_{jk} - \mu_k)^2 = \sigma_0^2 \mu_k^2 \quad . \quad (\text{B.11})$$

Equations (B.10) and (B.11) may be taken as the definitions of μ_k and σ_0^2 . The relative variance σ_0^2 was found by measurement to be essentially independent of k , and to have a value of ~ 0.02 . The value of μ_k was not directly determined.

We now make the approximation that drifts in the ORELA flux intensity do not occur within a 10-minute cycle but only between cycles. That is, we assume

$$\mu_k = \frac{1}{n} \sum_{j=1}^n m_{jk} \approx \frac{1}{T_k} \sum_{j=1}^{T_k} m_{jk}$$

or from Eq. (B.7)

$$\mu_k \approx \frac{m_k}{T_k} \quad . \quad (\text{B.12})$$

Likewise, Eq. (B.11) becomes

$$1 + \sigma_0^2 = \frac{1}{\mu_k^2} \frac{1}{n} \sum_{j=1}^n m_{jk}^2 \approx \left(\frac{T_k}{m_k} \right)^2 \frac{1}{T_k} \sum_{j=1}^{T_k} m_{jk}^2 \quad (\text{B.13})$$

Substituting the value of m_{jk}^2 from Eq. (B.9) into Eq. (B.13) and rearranging give

$$\frac{m^2}{T^2} \sum_{j=1}^{T_k} F_{jk}^2 \approx T_k \left(\frac{m_k}{T_k} \right)^2 (1 + \sigma_0^2) \quad (\text{B.14})$$

Summing over cycles k and rearranging give

$$\frac{1}{T} \sum_{k=1}^K \sum_{j=1}^{T_k} F_{jk}^2 \approx (1 + \sigma_0^2) \frac{T}{m^2} \sum_{k=1}^K \frac{m_k^2}{T_k} \quad (\text{B.15})$$

Comparison of Eq. (B.15) with Eq. (B.5) gives the final result for our approximation for $1 + \sigma^2$:

$$1 + \sigma^2 = (1 + \sigma_0^2) \frac{T}{m^2} \sum_{k=1}^K \frac{m_k^2}{T_k} \quad (\text{B.16})$$

m_k and T_k are the monitor counts and triggers for the k^{th} ~ 10 -minute cycle, m and T are the summed monitor counts and triggers for the run, and σ_0^2 is the variance of the flux intensity distribution described in Sect. 4.1 of this report.

APPENDIX C. MONITOR UNCERTAINTIES DUE TO DEADTIME CORRECTIONS

In this Appendix we describe the deadtime corrections necessary to determine the uncertainties associated with the monitor counter. For each cycle we store the triggers, valid stops, and house monitor counts, but not the individual spectra from the NE110 detector. The house monitor and the BF₃ monitor spectra are not taken as part of the measurement. Since the BF₃ detector averages one count per two triggers, deadtime effects are not a problem for the detector. The house monitor averages 11 counts per trigger, and during preparation of this report we obtained a time-of-flight spectrum from this detector to determine if deadtime corrections must be made. The spectral shape showed that the number of counts dropped by a factor of 60 over the 551 μsec looking time, with half of the integrated counts coming in the first 73 μsec after the gate opened. Estimating a maximum deadtime of 1 μsec for this detector system, the maximum deadtime correction is calculated to be $\approx 4\%$. Since this would be the same for both sample-in and -out, it would cancel out, assuming no spectral shape changes. Thus, we do not correct the house monitor counter for deadtime.

Since we do not store the individual spectra from the NE110 detector for each cycle, we must make some approximations to estimate a deadtime correction factor for each cycle. First, we assume that the spectral shape does not change appreciably for each cycle, thus we get an average spectrum by dividing the counts in each channel of the spectrum by the number of cycles in the run. We then deadtime correct this average spectrum for a few cycles, using the correct number of triggers for each cycle. An average deadtime correction for the n^{th} cycle is then extracted via

$$\langle D \rangle^n = \frac{\sum_{i=1}^N D_i^n C_i}{\sum_{i=1}^N C_i} \quad (\text{C.1})$$

This average deadtime correction factor can then be used to correct the valid stops for the particular cycle under consideration.

However, since the deadtime correction program takes about 5 minutes to run for each cycle, and we have 60-70 cycles to correct for a given run, it is prudent to make another approximation. The expression for the deadtime correction factor for channel j and the n^{th} cycle is (see Sect. 4.1 and Eq. (4.1) of text)

$$D_j^n = \frac{1}{1 - \frac{\sum_{k=1}^4 \left(\sum_i C_i + C_j/2 \right)}{T^n}} \quad (\text{C.2})$$

Our objective is to be able to directly estimate $\langle D \rangle^n$ from T^n , thus eliminating the computation of $\langle D \rangle^n$ from the deadtime correction program. Recall that the quantity

$$\sum_{k=1}^4 \left(\sum_i C_i + C_j/2 \right) \quad (\text{C.3})$$

represents a sum over selected channels in the k^{th} bias level spectrum; the range of the sum over i is a function of the bias level k . Our next approximation is to replace Eq. (C.3) by a parameter corresponding to an average number of counts, and is dependent only on an average deadtime period $\Delta\tau$.

$$\sum_{k=1}^4 \left(\sum_i C_i + C_j/2 \right) \rightarrow \langle C \rangle_{\Delta\tau} \quad (\text{C.4})$$

This approximation is independent of the sum over i and is consistent with the concept of an average deadtime correction factor. Substituting Eqs. (C.4) and (C.2) into Eq. (C.1)

$$\langle D \rangle^n = \frac{\sum_{i=1}^N C_i \left(\frac{1}{1 - \langle C \rangle_{\Delta\tau}} \right)}{\sum_{i=1}^N C_i} \quad (\text{C.5})$$

Thus,

$$\langle D \rangle^n = \frac{1}{1 - \frac{\langle C \rangle_{\Delta\tau}}{T^n}} \left(\frac{\sum_{i=1}^N C_i}{\sum_{i=1}^N C_i} \right) \quad (\text{C.6})$$

or we have our desired result

$$\langle D \rangle^n = \frac{1}{1 - \frac{\langle C \rangle_{\Delta\tau}}{T^n}} \quad (\text{C.7})$$

To evaluate $\langle C \rangle_{\Delta\tau}$, we solve for $\langle C \rangle_{\Delta\tau}$

$$\langle C \rangle_{\Delta\tau} = T^n \left(1 - \frac{1}{\langle D \rangle^n} \right) \quad (\text{C.8})$$

Using values for T^n and $\langle D \rangle^n$ from the few cycles for which we did the full deadtime correction calculation to obtain $\langle D \rangle^n$, we find an average value of $\langle C \rangle_{\Delta\tau} = 90641 \pm 59$ for sample-in, and 128627 ± 210 for sample-out. Substituting these values in and recalculating $\langle D \rangle^n$ with these approximations, we find agreement with the correct $\langle D \rangle^n$ to better than 0.05%. Thus, we have used these approximations as represented by Eq. (C.9) to calculate the deadtime corrected valid stops for each cycle.

APPENDIX D. AVERAGED CROSS SECTION RESULTS

In this appendix we present numerical values of the averaged energies and cross sections, and the statistical, systematic, and total uncertainties as described in Sect. 6.2.6 of this report. The energies are given in MeV, cross sections in barns, and uncertainties (standard deviations) in percent.

For compactness, these results are on microfiche attached to this report.

ORNL/TM-8203
ENDF-333
Dist. Category UC-79d

INTERNAL DISTRIBUTION

- | | | | |
|--------|-------------------|-----|---------------------------------|
| 1. | L. S. Abbott | 36. | R. W. Peelle |
| 2. | J. W. T. Dabbs | 37. | F. G. Perey |
| 3. | G. de Saussure | 38. | R. R. Spencer |
| 4. | J. K. Dickens | 39. | L. W. Weston |
| 5. | G. F. Flanagan | 40. | A. Zucker |
| 6. | R. Gwin | 41. | P. W. Dickson, Jr. (consultant) |
| 7-11. | J. A. Harvey | 42. | H. J. C. Kouts (consultant) |
| 12. | D. M. Hetrick | 43. | W. B. Loewenstein (consultant) |
| 13-17. | N. W. Hill | 44. | Richard Wilson (consultant) |
| 18-22. | C. H. Johnson | 45. | Central Research Library |
| 23-27. | D. C. Larson | 46. | ORNL Y-12 Technical Library |
| 28-32. | N. M. Larson | 47. | Document Reference Section |
| 33. | R. L. Macklin | 48. | Laboratory Records |
| 34. | F. C. Maienschein | 49. | Laboratory Records - RC |
| 35. | D. K. Olsen | 50. | ORNL Patent Section |

EXTERNAL DISTRIBUTION

51. Office of Assistant Manager for Energy Research and Development, Department of Energy, Oak Ridge Operations Office, Oak Ridge, TN 37830
- 52-53. Director, Reactor Research and Development, USDOE, Washington, DC 20545
54. Dr. W. P. Poenitz, Argonne National Laboratory, 9700 South Cass Ave., Argonne, IL 60439
55. Mr. Philip B. Hemmig, Chief, Physics Branch, Reactor Research and Technology, Office of Energy Technology, U.S. Department of Energy, Washington, DC 20545
56. Dr. R. C. Block, Department of Nuclear Engineering, Rensselaer Polytechnic Institute, Troy, NY 12181
57. Dr. Donald L. Smith, Building 314, Applied Physics Division, Argonne National Laboratory, 9700 South Cass Ave., Argonne, IL 60439
58. Dr. S. L. Whetstone, Division of Nuclear Sciences, Office of Basic Energy Sciences, U.S. Department of Energy, Room G-355, Washington, DC 20545
59. Dr. M. R. Bhat, Building 197D, National Nuclear Data Center, Brookhaven National Laboratory, Upton, NY 11973
60. Dr. G. F. Auchampaugh, Los Alamos Scientific Laboratory, MS 442, P-3, Los Alamos, NM 87545

EXTERNAL DISTRIBUTION (contd)

61. Dr. R. F. Carlton, Middle Tennessee State University, Physics Department, Box 407, Murfreesboro, TN 37132
62. Dr. E. C. Lynn, Nuclear Physics Division, Atomic Energy Research Establishment, Harwell, Didcot, Oxon, OX11 0RA, United Kingdom
63. Dr. M. G. Sowerby, Nuclear Physics Division, Bldg. 418, Atomic Energy Research Establishment, Harwell, Didcot, Oxon, OX11, 0RA, United Kingdom
64. Dr. Roger White, Lawrence Livermore National Laboratory, P. O. Box 808, Livermore, CA 94550
65. Dr. R. R. Winters, Physics Department, Denison University, Granville, Ohio 43023
66. Dr. Herman Weigmann, Central Bureau for Nuclear Measurements, Steenweg naar Retie, B-2440 Geel, Belgium
67. Dr. G. L. Morgan, Los Alamos National Laboratory, P. O. Box 1663, Group P-15, MS D406, Los Alamos, NM 87545
- 68-242. For distribution as shown in TID-4500 Distribution Category UC-79d, Liquid Metal Fast Breeder Reactor Physics - Base (60 copies - ENDF Distribution)

ORNL/TM-8203
ENDF-333

APPLICATION OF NEW TECHNIQUES TO ORELA NEUTRON TRANSMISSION MEASUREMENTS AND
THEIR UNCERTAINTY ANALYSIS: THE CASE OF NATURAL NICKEL FROM 2 keV TO 20 MeV

D.C. Larson N.M. Larson J.A. Harvey N.W. Hill C.H. Johnson

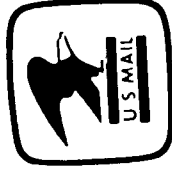
Microfiche  Enclosed

UNITED STATES DEPARTMENT OF ENERGY

P.O. BOX 62
OAK RIDGE, TENNESSEE 37830

OFFICIAL BUSINESS
PENALTY FOR PRIVATE USE, \$300

POSTAGE AND FEES PAID
UNITED STATES
DEPARTMENT OF ENERGY



BROOKHAVEN NATIONAL LAB
ATTN DR NORMAN E HOLDEN
NATIONAL NUCLEAR DATA CENTER
BLDG 197
UPTON NY 11973

ENDF